Journal of Computational Physics **163,** 376–433 (2000)
doi:10.1006/jcph.2000.6569, available online at http://www.idealibrary.com on IDEAL®

A High-Resolution Numerical Method for a Two-Phase Model of Deflagration-to-Detonation Transition

Keith A. Gonthier* and Joseph M. Powers†

*Department of Mechanical Engineering, Lamar University, Beaumont, Texas 77710; †Department of Aerospace and Mechanical Engineering, University of Notre Dame, Notre Dame, Indiana 46556
E-mail: gonthierka@hal.lamar.edu, powers@nd.edu

Received July 22, 1999; revised June 9, 2000

A conservative, upwind numerical method is formulated for the solution of a two-phase (reactive solid and inert gas) model of deflagration-to-detonation transition (DDT) in granular energetic solids. The model, which is representative of most two-phase DDT models, accounts for complete nonequilibrium between phases and constitutes a nonstrictly hyperbolic system of equations having parabolic degeneracies. The numerical method is based on Godunov's methodology and utilizes a new approximate solution for the two-phase Riemann problem for arbitrary equations of state. The approximate solution is similar to the Roe-type Riemann solution for single-phase systems. The method is able to accurately capture strong shocks associated with each phase without excessive smearing or spurious oscillations and can accurately resolve fine-scale detonation structure resulting from interaction between phases. The utility of the method is demonstrated by comparing numerical predictions with known solutions for three test cases: (1) a two-phase shock tube problem; (2) the evolution of a steady compaction wave in a granular material resulting from weak piston impact (∼100 m/s); and (3) the evolution of a steady two-phase detonation wave in an energetic granular material resulting from weak piston impact. The nominally second-order accurate numerical method is shown to have global convergence rates of 1.001 and 1.670 for inert test cases with (case 1) and without (case 2) discontinuities, respectively. For the reactive test case having a discontinuity (case 3), a convergence rate of 1.834 was predicted for coarse grids that seemed to be approaching the expected value of unity with increasing resolution. © 2000 Academic Press

1. INTRODUCTION

In this paper we give a detailed description of the numerical method first used by Gonthier and Powers [21] to simulate deflagration-to-detonation transition (DDT) in granular energetic solids. This and other research studies on DDT have largely been motivated by concerns

0021-9991/00 $35.00
Copyright © 2000 by Academic Press
All rights of reproduction in any form reserved.

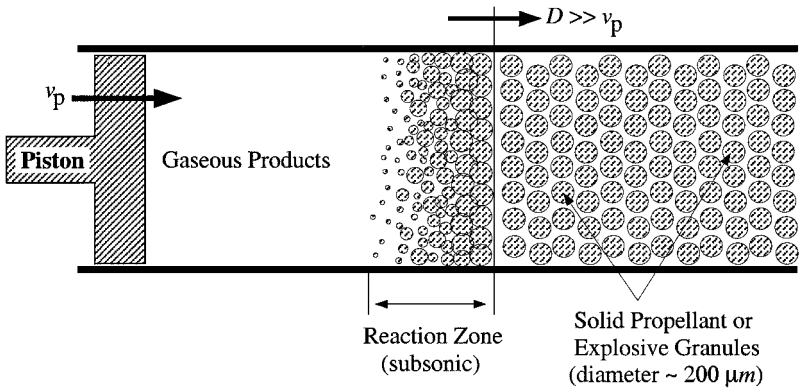

FIG. 1. Schematic of a piston-induced two-phase detonation.

over the increased sensitivity of damaged high explosives and propellants to mechanical impact. Experiments have shown that weak mechanical shock ($\sim$0.2 GPa) is often sufficient to initiate detonation in granulated energetic material through various mechanisms of hot-spot formation [34, 36, 53], whereas only strong shocks ($>$10 GPa) provide sufficient energy to initiate detonation in cast material. Here, we first briefly introduce the physical problem, focusing on issues relevant to the numerical solution of two-phase DDT models, and then describe a new high-resolution numerical method for accurately solving these models.

Figure 1 shows a simple schematic of a paradigm problem for the initiation of detonation in damaged high explosives by weak, planar mechanical shock. This problem, which is well characterized by experiments [36, 53], involves the low-velocity impact of a moving piston, having velocity $v_p \sim 100$ m/s, with a stationary bed of granular explosive. In this figure, transition to detonation, which results from a complex, not well-understood sequence of physical events, has already occurred. The resulting detonation wave, composed of a thin lead shock followed by a thick reaction zone, is propagating to the right at speed D, where $D \gg v_p$, and is supersonic with respect to both the ambient gas and the solid. As shown by Gonthier [22], the lead shock may be in the gas and/or solid depending on the relative rates of the various physical processes occurring within the reaction zone structure; such processes will be discussed in detail. Typically, the shocks are modeled as discontinuities since the length scales associated with diffusive processes, which define a shock structure, are thin compared to length scales associated with reaction and other relaxation processes. Adiabatic compression of the ambient material by the lead shock and compaction-induced dissipation provide sufficient energy to initiate chemical reaction. Due to reaction, solid particle mass, momentum, and energy are converted into gas mass, momentum, and energy. This conversion process sustains propagation of the wave through the material by means of acoustic energy transmission from the point of local reaction, through the subsonic region of the reaction zone, and to the lead shock. At the end of the reaction zone, all of the solid is completely consumed by reaction. The reaction rate determines both the time required for complete reaction and the length of the reaction zone; typical reaction times are O (1 μs) and typical reaction zone lengths are O (1 mm).

To gain better understanding of combustion in porous solids and DDT, a number of two-phase continuum models have been developed [3, 6, 8, 13, 35, 41, 44]. The models are posed as coupled time-dependent partial differential equations (PDEs) which track the evolution of mass, momentum, and energy of an inert gas and reactive solid particles. For mathematical

closure, some models include an additional PDE to account for the dynamic compaction of the solid particles [3, 6, 35, 44], while others use an algebraic stress relation to account for compaction [8]. Physical processes accounted for by most models include (1) convective transport in both the gas and solid, (2) mass, momentum, and energy transfer from the solid to the gas due to chemical reaction, (3) momentum and energy exchange between the gas and the solid due to drag interaction, (4) thermal energy exchange between the gas and the solid due to convective heat transfer, and (5) material compaction due to a stress imbalance between the gas pressure, the solid pressure, and an intragranular stress. Though various two-phase DDT models have common features, they often differ in the functional forms of the evolution equations. Some of the relevant differences are discussed in detail by Powers *et al.* [44], and more recently by Bdzil *et al.* [6] and Saurel and Abgrall [58].

One relevant difference concerns the inclusion of nonconservative "nozzling" terms in the gas and solid momentum and energy equations which are proportional to the spatial derivative of solid volume fraction. Some models include these terms [3, 35], whereas others exclude them [8, 44]. Inclusion of such terms introduces additional asymmetry into a model, which in principle should be indifferent to the description of individual phases. The primary rationale for including nozzling terms, which are constructed in a nonunique manner, is to ensure that another asymmetry, known as a dynamic compaction model, identically satisfies the strong form of the second law of thermodynamics [6]; plausibility arguments that relate the behavior of the nozzling terms to one-dimensional flow in a variable cross-sectional area duct are also given.

While we find no fault in the rationale given in Ref. [6], we exclude nozzling terms in our model, and we offer the following arguments for doing so. First, no rigorous micro-scale justification for either the inclusion or the exclusion of nozzling terms currently exists. Consequently, all current multiphase flow models remain open to such scrutiny. Second, as noted by Powers *et al.* [44], satisfaction of the strong form of the second law, while appealing, may be overly restrictive. Even if dynamic compaction induces a decrease in entropy, there may be sufficient compensation from competing dissipative processes to guarantee satisfaction of the more general weak form of the second law, which only requires a global increase in entropy. Third, as noted in Ref. [6], nozzling does not significantly affect low-pressure compaction waves, a key ingredient for DDT, becoming less important as pressure increases. This result suggests that nozzling may play a small role in the DDT process, though there is some belief that nozzling could play an important role in low-speed gas permeation scenarios [1]. We also recognize that its role under detonation conditions is not currently well characterized. Our results without nozzling have shown good agreement with existing experimental DDT [22] and compaction wave [43] data. Fourth, we avoid mathematical and numerical difficulties in the analysis of shocks associated with models having a nonconservative form. Such difficulties are often addressed by simply grouping the nonconservative terms together with algebraic source terms and proceeding in a manner similar to what will be done here (cf. [58]), albeit with slightly modified source terms. We also note that, in contrast to what is stated in Refs. [50, 58], the exclusion of nozzling terms is not necessary to retain hyperbolicity of our model, as similar models containing nozzling terms are known to also be hyperbolic [6, 15]. So, while a definitive argument for nozzling remains to be found, the numerical technique given here can be applied in either case, and the predicted results will be similar.

There are a number of difficulties in numerically solving two-phase DDT models that stringently test the capabilities of the method. First, the numerical method must be capable of capturing strong shocks in each phase with minimal numerical diffusion and

dispersion. This requirement is especially important for two-phase DDT simulations since such numerical artifacts can substantially affect local phase interaction processes, resulting in severe numerical inaccuracies. Second, the numerical method must be capable of handling mathematical stiffness, which arises due to the disparate time scales associated with both gas and solid convection, and phase interaction processes. For instance, gas and solid acoustic speeds and particle speeds can differ by an order of magnitude, and the rates of phase interaction processes can differ by several orders of magnitude. This problem has partly motivated the development of reduced two-phase DDT models based on asymptotic analyses [30]. Third, the numerical method must be capable of handling a local loss of hyperbolicity, as most current two-phase DDT models possess singularities for which the equations become parabolic [15, 21]. As discussed later, the physical implications of these singularities are unclear, but the loss of hyperbolicity results in numerical instabilities that must be suppressed. Last, the numerical method must accommodate nonideal equations of state for both the gas and the solid to characterize their thermodynamic behavior under the extreme conditions of detonation. The numerical method formulated in this paper satisfies each of these requirements.

Most commonly used numerical methods for simulating DDT are based on either conventional method of lines (MOL) or MacCormack predictor/corrector techniques, relying on explicitly added artificial viscosity to capture shocks and maintain numerical stability [3, 4, 8, 46, 54]. It is likely that this added viscosity reduces the ability of such methods to accurately resolve fine-scale detonation structure due to excessive numerical smearing. Furthermore, the optimal amount of artificial viscosity needed to reasonably capture shocks is largely problem-specific. Though several modern high-resolution upwind numerical methods have been developed and applied to dilute two-phase compressible flows [55–57] (i.e., the dilute phase is assumed to occupy negligible volume), these methods are not applicable to the particle-laden flows of interest here. Saurel and Abgrall [58] recently applied a Godunov-based method using the existing numerical flux functions of Rusanov [51] and Harten *et al.* [26] to nondilute compressible flows. Their method is robust, as it can be applied to both multifluid and multiphase compressible flows, though it generates noticeable dispersion for the test cases shown in Ref. [58], likely due to the low accuracy of the Riemann solvers employed.

The work contained in this paper provides two original contributions to the numerical modeling and theory of two-phase detonation. First, we give a new approximate solution for the two-phase Riemann problem and use it with Godunov's methodology to obtain an accurate numerical method for computing DDT. In addition to increased computational efficiency, the use of an approximate solution is necessitated by the lack of an exact solution. The approximate Riemann solution is formulated following the approach used by Roe and Pike [48] to obtain an approximate Riemann solution for the Euler equations for ideal equations of state and that used by Glaister [18] to obtain an approximate solution for nonideal equations of state. Consequently, the method formulated in this paper has the shock resolution property common to Roe-type solvers and is applicable to general gas and solid equations of state. Second, based on detailed comparisons between numerical predictions and results of a steady, two-phase detonation wave analysis [22], we predict for the first time the evolution of a two-phase *weak* detonation structure, indicating that the Chapman–Jouguet (CJ) wave speed is not the unique wave speed for a self-propagating two-phase detonation. Together with Ref. [21], which gives predictions of the evolution of the steady CJ detonation structure identified by Powers *et al.* [45], this work gives the only known detailed comparison between unsteady numerical predictions and steady-state results

for two-phase detonation wave structure. Further, these comparisons conclusively show that all relevant detonation length scales are fully resolved, in contrast to most published work in this area, which is underresolved.

The plan of the paper is as follows. We first give the model equations and perform a characteristic analysis to determine the mathematical framework needed for the construction of the approximate Riemann solution. Next, we briefly discuss the two-phase Riemann problem and obtain an exact solution for the linearized Riemann problem. Based on this exact solution, we then formulate an approximate solution valid for arbitrary initial data. We give a technique for suppressing numerical instabilities associated with a loss of hyperbolicity and summarize the techniques used for increasing both the spatial and the temporal accuracy of the method and for the coupling of the Godunov-based method with a standard ordinary differential equation (ODE) solver to account for the influence of inhomogeneous phase interaction terms. Last, we illustrate the performance of the method based on detailed comparisons between numerical predictions and known theoretical solutions for granular energetic solids, and we quantify its convergence rate for both continuous and discontinuous solutions.

2. MATHEMATICAL MODEL

The model adopted for this work is a variant of the unsteady, two-phase continuum model formulated by Powers *et al.* [44, 45]. As discussed later, we have modified their model to include an additional evolution equation for an ignition variable and have incorporated an intragranular stress relation that better describes dynamic compaction of granular explosives [43]. The model assumes the existence of reactive, spherical solid particles and an inert gas, both having fixed composition, and further assumes that both phases are compressible, all intraphase diffusive transport is negligible, body forces are negligible, each phase is in complete nonequilibrium with the other, and the two-phase flow is one-dimensional in a macroscopic sense. The model is representative of other two-phase continuum models commonly used to predict detonation in granulated material [3, 8] and is able to predict most experimentally observed features of DDT [22].

The two-phase model equations are given by the following:

$$\frac{\partial}{\partial t}[\rho_1\phi_1] + \frac{\partial}{\partial x}[\rho_1\phi_1 u_1] = \left(\frac{3}{r}\right)\rho_2\phi_2 a P_1^m H(I - I_{\text{ig}}), \tag{2.1}$$

$$\frac{\partial}{\partial t}[\rho_1\phi_1 u_1] + \frac{\partial}{\partial x}\left[\rho_1\phi_1 u_1^2 + P_1\phi_1\right] = u_2\left(\frac{3}{r}\right)\rho_2\phi_2 a P_1^m H(I - I_{\text{ig}}) + \beta\frac{\phi_1\phi_2}{r}(u_2 - u_1), \tag{2.2}$$

$$\begin{aligned}\frac{\partial}{\partial t}\left[\rho_1\phi_1\left(e_1 + \frac{u_1^2}{2}\right)\right] + \frac{\partial}{\partial x}\left[\rho_1\phi_1 u_1\left(e_1 + \frac{u_1^2}{2} + \frac{P_1}{\rho_1}\right)\right] \\ = \left(e_2 + \frac{u_2^2}{2}\right)\left(\frac{3}{r}\right)\rho_2\phi_2 a P_1^m H(I - I_{\text{ig}}) + \beta\frac{\phi_1\phi_2}{r}u_2(u_2 - u_1) + h\frac{\phi_1\phi_2}{r^{1/3}}(T_2 - T_1),\end{aligned} \tag{2.3}$$

$$\frac{\partial}{\partial t}[\rho_2\phi_2] + \frac{\partial}{\partial x}[\rho_2\phi_2 u_2] = -\left(\frac{3}{r}\right)\rho_2\phi_2 a P_1^m H(I - I_{\text{ig}}), \tag{2.4}$$

$$\frac{\partial}{\partial t}[\rho_2\phi_2 u_2] + \frac{\partial}{\partial x}\left[\rho_2\phi_2 u_2^2 + P_2\phi_2\right] = -u_2\left(\frac{3}{r}\right)\rho_2\phi_2 a P_1^m H(I - I_{\text{ig}}) - \beta\frac{\phi_1\phi_2}{r}(u_2 - u_1), \tag{2.5}$$

$$\frac{\partial}{\partial t}\left[\rho_2\phi_2\left(e_2+\frac{u_2^2}{2}\right)\right]+\frac{\partial}{\partial x}\left[\rho_2\phi_2 u_2\left(e_2+\frac{u_2^2}{2}+\frac{P_2}{\rho_2}\right)\right]$$
$$=-\left(e_2+\frac{u_2^2}{2}\right)\left(\frac{3}{r}\right)\rho_2\phi_2 a P_1^m H(I-I_{\mathrm{ig}})-\beta\frac{\phi_1\phi_2}{r}u_2(u_2-u_1)-h\frac{\phi_1\phi_2}{r^{1/3}}(T_2-T_1), \tag{2.6}$$

$$\frac{\partial\phi_2}{\partial t}+u_2\frac{\partial\phi_2}{\partial x}=\frac{\phi_1\phi_2}{\mu_c}(P_2-P_1-f)-\left(\frac{3}{r}\right)\phi_2 a P_1^m H(I-I_{\mathrm{ig}}), \tag{2.7}$$

$$\frac{\partial n}{\partial t}+\frac{\partial}{\partial x}[u_2 n]=0, \tag{2.8}$$

$$\frac{\partial I}{\partial t}+u_2\frac{\partial I}{\partial x}=k_I(1-I)\left[\frac{P_1\phi_1+P_2\phi_2-P_{1o}\phi_{1o}-P_{2o}\phi_{2o}}{P_{1o}\phi_{1o}+P_{2o}\phi_{2o}}\right]^2\exp\left[-\frac{T_I}{T_1\phi_1+T_2\phi_2}\right], \tag{2.9}$$

$$f=(P_{2o}-P_{1o})\,\frac{\phi_2^2}{\phi_{2o}^2}\,\frac{(2-\phi_{2o})^2}{(2-\phi_2)^2}\,\frac{\ln\frac{1}{1-\phi_2}}{\ln\frac{1}{1-\phi_{2o}}}, \tag{2.10}$$

$$n=\frac{3\phi_2}{4\pi r^3}, \tag{2.11}$$

$$\phi_1+\phi_2=1, \tag{2.12}$$

$$P_1=P_1(\rho_1,T_1), \tag{2.13}$$

$$e_1=e_1(\rho_1,T_1), \tag{2.14}$$

$$P_2=P_2(\rho_2,T_2), \tag{2.15}$$

$$e_2=e_2(\rho_2,T_2). \tag{2.16}$$

In these equations, the subscripts "1" and "2" denote quantities associated with the gas and solid, respectively. Quantities labeled with subscript o are associated with the ambient state. The independent variables are time t and position x. Dependent variables are as follows: the phase density ρ_i $(i=1,2)$, defined as the mass of phase i per unit volume occupied by that phase; the phase pressure P_i; the phase temperature T_i; the particle velocity u_i; the specific internal energy e_i; the volume fraction ϕ_i; the radius of the spherical solid particles r; the number of particles per unit volume n; the intragranular stress f; and the ignition variable I. In Eqs. (2.1)–(2.9), $H(I-I_{\mathrm{ig}})$ is the Heaviside unit step function, and I_{ig}, a, m, β, h, μ_c, k_I, and T_I are constant parameters, which are described below. Equations (2.1)–(2.16) constitute a system of 16 equations in 16 unknowns; thus, the system of equations is mathematically closed and, in principle, can be solved provided that appropriate initial and boundary conditions are supplied.

Equations (2.1), (2.2), and (2.3) are evolution equations for the mass, momentum, and total energy of the gas. Equations (2.4), (2.5), and (2.6) are evolution equations for the mass, momentum, and total energy of the solid. Equations (2.7)–(2.9) are evolution equations for the solid volume fraction, the particle number density, and the ignition variable, respectively.

The forcing terms in Eqs. (2.1) and (2.4) account for the exchange of mass from the solid to the gas due to combustion. Here, mass exchange is modeled as a single, irreversible process (solid $\rightarrow$ inert gas), and all chemical reaction is assumed to occur on the particle surface. Combustion initiation occurs for $I \geq I_{\mathrm{ig}}$, where I_{ig} is a constant ignition parameter.

The combustion rate is modeled by a burn law which depends upon the gas pressure. Values for the combustion rate parameters a and m are typically correlated to match strand burn rate data [4].

The forcing terms in Eqs. (2.2) and (2.5) account for two forms of momentum exchange between the gas and the solid. First, the gas is gaining that momentum associated with the solid which is being converted into gas due to combustion. Second, there is an exchange of momentum due to solid particle–gas drag interaction. The drag interaction is modeled by a drag law which states that the drag is proportional to the difference in velocity between the phases, and inversely proportional to the particle radius. In the drag law, β is defined as a drag coefficient which gives the time scale for velocity equilibration between the phases.

The forcing terms in Eqs. (2.3) and (2.6) account for the exchange of energy between the gas and the solid. Energy exchange associated with combustion, and with particle-gas drag work, is accounted for, as is thermal energy exchange between the gas and the solid. The thermal energy exchange rate is assumed to be proportional to the temperature difference between the gas and the solid, and inversely proportional to the cube root of the particle radius; here, h is defined as a heat transfer coefficient which gives the time scale for thermal equilibration between the phases.

Equation (2.7) is a dynamic compaction equation governing changes in solid volume fraction due to both compaction and combustion of the granular material. This equation predicts that, in the absence of combustion, the solid volume fraction, ϕ_2, will equilibrate to a value such that the solid pressure, P_2, equals the sum of the gas pressure, P_1, and the intragranular stress, f; the equilibration rate is governed by the parameter μ_c, which is referred to as the compaction viscosity. The use of this equation was first proposed by Baer and Nunziato [3]. Though this equation is not standard in all multiphase modeling, it does allow the modeling of rate-dependent material compaction, which is known to be important in the evolution of detonation in granulated material. Additionally, the use of this equation ensures that the characteristic wave speeds associated with the model equations are real [42–44], and that solutions of the governing PDEs are hyperbolic waves. The characteristic wave speeds of some two-phase models, particularly models which assume pressure equilibrium between the phases, have been shown to be imaginary; the models are thus unable to properly model discontinuous solutions as the initial-value problem is ill-posed [14, 47].

Equation (2.8) expresses that the total number of particles in the system is conserved. Though not considered here, it is possible to model the break-up of particles by including an appropriate inhomogeneous term in this equation.

Equation (2.9) is an *ad hoc* evolution equation for the ignition variable I. For this study, $0 \leq I \leq 1$, where $I_o = 0$ for the ambient state, and $I_{\text{ig}} = 0.5$. This equation is used to model the observed induction period occurring prior to the onset of vigorous combustion in piston-initiated DDT experiments [4, 36, 53]. The forcing term in this equation models the ignition variable as an increasing function of pressure and temperature of the gas and solid. Consequently, in agreement with experiments, higher temperatures and pressures result in a decrease in the induction time. In this equation, k_I and T_I are ignition rate constants. Similar equations have been used in other two-phase combustion models as "switches" for controlling the amount of chemical energy released by combustion during the induction period [5, 46, 60].

Equation (2.10) is an expression for the intragranular stress, which was used by Powers *et al.* [43] to analyze steady compaction waves in granular HMX. Equation (2.11) is the

definition of the local particle number density expressed in terms of the solid volume fraction and the particle radius, and Eq. (2.12) is a mixture saturation condition (i.e., no voids are present within the mixture). Equations (2.13) and (2.14), and Eqs. (2.15) and (2.16) are functional dependencies for the thermal and caloric equations of state for the gas and the solid, respectively. At this juncture, we choose not to specify exact forms for the state relations as the formulation of the numerical method in the following section does not require us to do so. Furthermore, different state relations are used for various problems in this paper, the exact forms of which are given where appropriate.

As discussed by Powers *et al.* [44, 45], the phase interaction terms have been constructed such that (1) the total mass, momentum, and energy of the gas–solid mixture are conserved; (2) the ambient state of the material is an equilibrium state; and (3) some analytical simplicity is retained. Additionally, the drag and thermal interaction terms have been constructed to guarantee a nonnegative change in mixture entropy in accordance with the strong form of the second law of thermodynamics. The combustion and compaction terms may under certain circumstances induce negative entropy changes, thus violating the strong form of the second law, though the less restrictive form may remain satisfied as previously discussed. Despite their relative simplicity, it is shown in Ref. [45] that these forms do predict the same trends as more complicated empirical relations.

Equations (2.13)–(2.16) can be used to define expressions for the gas sound speed, c_1, and the solid sound speed, c_2. To this end, we solve Eqs. (2.14) and (2.16) for T_1 and T_2, respectively, and substitute the results into Eqs. (2.13) and (2.15) to obtain the following functional dependencies:

$$P_1 = P_1(\rho_1, e_1), \tag{2.17}$$

$$P_2 = P_2(\rho_2, e_2). \tag{2.18}$$

The gas and solid sound speed can be expressed in terms of thermodynamic derivatives obtained from these relations,

$$c_1^2 \equiv \left.\frac{\partial P_1}{\partial \rho_1}\right|_{s_1} = \frac{P_1}{\rho_1}\Gamma_1 + \left.\frac{\partial P_1}{\partial \rho_1}\right|_{e_1}, \tag{2.19}$$

$$c_2^2 \equiv \left.\frac{\partial P_2}{\partial \rho_2}\right|_{s_2} = \frac{P_2}{\rho_2}\Gamma_2 + \left.\frac{\partial P_2}{\partial \rho_2}\right|_{e_2}, \tag{2.20}$$

where s_1 and s_2 are the specific entropy of the gas and solid, and Γ_1 and Γ_2 are the Grüneisen coefficients for the gas and solid, defined by

$$\Gamma_1 \equiv \frac{1}{\rho_1}\left.\frac{\partial P_1}{\partial e_1}\right|_{\rho_1}, \quad \Gamma_2 \equiv \frac{1}{\rho_2}\left.\frac{\partial P_2}{\partial e_2}\right|_{\rho_1}. \tag{2.21}$$

Finally, the construction of the numerical method requires that Eqs. (2.7) and (2.9) be expressed in divergence form. To this end, Eq. (2.4) is multiplied by ϕ_2, Eq. (2.7) is multiplied by $\rho_2\phi_2$, and the two resulting expressions are added to obtain

$$\frac{\partial}{\partial t}\left[\rho_2\phi_2^2\right] + \frac{\partial}{\partial x}\left[\rho_2 u_2\phi_2^2\right] = \frac{\rho_2\phi_1\phi_2^2}{\mu_c}(P_2 - P_1 - f) - 2\left(\frac{3}{r}\right)\rho_2\phi_2^2 a P_1^m H(I - I_{\text{ig}}). \tag{2.22}$$

Similarly, Eq. (2.4) is multiplied by I, Eq. (2.9) is multiplied by $\rho_2\phi_2$, and the two resulting

expressions are added to obtain

$$\frac{\partial}{\partial t}[\rho_2\phi_2 I] + \frac{\partial}{\partial x}[\rho_2\phi_2 u_2 I]$$
$$= k_I\rho_2\phi_2(1-I)\left[\frac{P_1\phi_1 + P_2\phi_2 - P_{1o}\phi_{1o} - P_{2o}\phi_{2o}}{P_{1o}\phi_{1o} + P_{2o}\phi_{2o}}\right]^2 \exp\left[-\frac{T_I}{T_1\phi_1 + T_2\phi_2}\right]$$
$$-\left(\frac{3}{r}\right)\rho_2\phi_2 I a P_1^m H(I - I_{ig}). \tag{2.23}$$

It is noted that spurious wave speeds for discontinuities may be introduced when PDEs are manipulated in this manner. However, Eqs. (2.7) and (2.9) are already in standard characteristic form; the characteristics are solid particle paths. Furthermore, as discussed in the following section, the corresponding characteristic fields are linearly degenerate; consequently, discontinuities in these fields propagate at speed u_2. This result is also obtained by a formal discontinuity analysis based on integral conservation expressions for Eqs. (2.22) and (2.23) [22]. Consequently, these manipulations will not affect the solution.

2.1. *Characteristic Analysis*

Equations (2.1)–(2.6), (2.8), (2.22), and (2.23) form a quasilinear system of nine first-order PDEs expressed in divergence form. Using vector notation, these equations can be compactly expressed by

$$\frac{\partial \mathbf{q}}{\partial t} + \frac{\partial \mathbf{f}(\mathbf{q})}{\partial x} = \mathbf{g}(\mathbf{q}), \tag{2.24}$$

where

$$\mathbf{q} = \left[\rho_1\phi_1,\ \rho_1\phi_1 u_1,\ \rho_1\phi_1\left(e_1 + \frac{u_1^2}{2}\right),\ \rho_2\phi_2,\ \rho_2\phi_2 u_2,\ \rho_2\phi_2\left(e_2 + \frac{u_2^2}{2}\right),\ \rho_2\phi_2^2,\ n,\ \rho_2\phi_2 I\right]^T, \tag{2.25}$$

$$\mathbf{f}(\mathbf{q}) = \left[\rho_1\phi_1 u_1,\ \rho_1\phi_1 u_1^2 + P_1\phi_1,\ \rho_1\phi_1 u_1\left(e_1 + \frac{u_1^2}{2} + \frac{P_1}{\rho_1}\right),\ \rho_2\phi_2 u_2,\ \rho_2\phi_2 u_2^2 + P_2\phi_2,\right.$$
$$\left.\rho_2\phi_2 u_2\left(e_2 + \frac{u_2^2}{2} + \frac{P_2}{\rho_2}\right),\ \rho_2 u_2\phi_2^2,\ u_2 n,\ \rho_2\phi_2 u_2 I\right]^T, \tag{2.26}$$

$$\mathbf{g}(\mathbf{q}) = \left[C_m,\ C_m u_2 + C_d,\ C_m\left(e_2 + \frac{u_2^2}{2}\right) + C_d u_2 + C_e,\right.$$
$$-C_m,\ -C_m u_2 - C_d,\ -C_m\left(e_2 + \frac{v_2^2}{2}\right) - C_d u_2 - C_e,$$
$$\left.\frac{\rho_2\phi_1\phi_2^2}{\mu_c}(P_2 - P_1 - f) - 2\phi_2 C_m,\ 0,\ \rho_2\phi_2 C_I - I C_m\right]^T, \tag{2.27}$$

and

$$C_m = \left(\frac{3}{r}\right)\frac{\rho_2\phi_2 a P_1^m}{r} H(I - I_{ig}),\quad C_d = \beta\frac{\phi_1\phi_2}{r}(u_2 - u_1),\quad C_e = h\frac{\phi_1\phi_2}{r^{1/3}}(T_2 - T_1), \tag{2.28}$$

$$C_I = k_I(1-I)\left[\frac{P_1\phi_1 + P_2\phi_2 - P_{1o}\phi_{1o} - P_{2o}\phi_{2o}}{P_{1o}\phi_{1o} + P_{2o}\phi_{2o}}\right]^2 \exp\left[-\frac{T_I}{T_1\phi_1 + T_2\phi_2}\right].$$

Here, $\mathbf{q} \in \Re^9$ is the vector of conserved quantities, $\mathbf{f} \in \Re^9$ is the flux vector, and $\mathbf{g} \in \Re^9$ is the source vector ($\Re$ is the set of real numbers). Both $\mathbf{f}$ and $\mathbf{g}$ are functions of $\mathbf{q}$.

We now give a standard analysis applicable to systems of first-order quasilinear PDEs in two independent variables to determine the classification of the model equations and to provide the mathematical framework needed for the development of the numerical method. The analysis requires that Eq. (2.24) be expressed in the following nondivergence form obtained by carrying out the differentiation of $\mathbf{f}$ with respect to x,

$$\frac{\partial \mathbf{q}}{\partial t} + \mathbf{A}(\mathbf{q})\frac{\partial \mathbf{q}}{\partial x} = \mathbf{g}(\mathbf{q}), \tag{2.29}$$

where $\mathbf{A}$ is the 9×9 flux Jacobian matrix defined by

$$\mathbf{A} \equiv \frac{\partial \mathbf{f}}{\partial \mathbf{q}}. \tag{2.30}$$

If we denote the components of $\mathbf{q}$ and $\mathbf{f}$ by q_j and f_j $(j = 1, \ldots, 9)$, respectively, then $\mathbf{A}$ is given by

$$\mathbf{A} = \begin{bmatrix} \partial f_1/\partial q_1 & \partial f_1/\partial q_2 & \cdots & \partial f_1/\partial q_9 \\ \partial f_2/\partial q_1 & \partial f_2/\partial q_2 & \cdots & \partial f_2/\partial q_9 \\ \vdots & \vdots & & \vdots \\ \partial f_9/\partial q_1 & \partial f_9/\partial q_2 & \cdots & \partial f_9/\partial q_9 \end{bmatrix}. \tag{2.31}$$

For the construction of $\mathbf{A}$, it is necessary to first express ϕ_1, ρ_1, u_1, e_1, ϕ_2, ρ_2, u_2, e_2, n, and I as functions of $\mathbf{q}$. In particular, we have

$$\begin{aligned} \phi_1 &= 1 - \frac{q_7}{q_4}, \quad \rho_1 = \frac{q_1}{1 - q_7/q_4}, \quad u_1 = \frac{q_2}{q_1}, \quad e_1 = \frac{q_3}{q_1} - \frac{1}{2}\left(\frac{q_2}{q_1}\right)^2, \\ \phi_2 &= \frac{q_7}{q_4}, \quad \rho_2 = \frac{q_4^2}{q_7}, \quad u_2 = \frac{q_5}{q_4}, \quad e_2 = \frac{q_6}{q_4} - \frac{1}{2}\left(\frac{q_5}{q_4}\right)^2, \\ n &= q_8, \quad I = \frac{q_9}{q_4}. \end{aligned} \tag{2.32}$$

Given these expressions for ρ_1, e_1, ρ_2, and e_2, and using the functional dependencies of Eq. (2.18), the derivatives

$$\left.\frac{\partial P_1}{\partial q_j}\right|_{q_{j'(j'\neq j)}} \quad \text{and} \quad \left.\frac{\partial P_2}{\partial q_j}\right|_{q_{j'(j'\neq j)}} \quad (j, j' = 1, \ldots, 9),$$

which are needed for the construction of $\mathbf{A}$, can be computed by direct application of the chain rule:

$$\left.\frac{\partial P_1}{\partial q_j}\right|_{q_{j'(j'\neq j)}} = \left.\frac{\partial P_1}{\partial \rho_1}\right|_{e_1} \left.\frac{\partial \rho_1}{\partial q_j}\right|_{q_{j'(j'\neq j)}} + \left.\frac{\partial P_1}{\partial e_1}\right|_{\rho_1} \left.\frac{\partial e_1}{\partial q_j}\right|_{q_{j'(j'\neq j)}}, \tag{2.33}$$

$$\left.\frac{\partial P_2}{\partial q_j}\right|_{q_{j'(j'\neq j)}} = \left.\frac{\partial P_2}{\partial \rho_2}\right|_{e_1} \left.\frac{\partial \rho_2}{\partial q_j}\right|_{q_{j'(j'\neq j)}} + \left.\frac{\partial P_2}{\partial e_2}\right|_{\rho_2} \left.\frac{\partial e_2}{\partial q_j}\right|_{q_{j'(j'\neq j)}}. \tag{2.34}$$

Explicit expressions for the derivatives $\frac{\partial P_1}{\partial \rho_1}|_{e_1}$ and $\frac{\partial P_1}{\partial e_1}|_{\rho_1}$, and $\frac{\partial P_2}{\partial \rho_2}|_{e_1}$ and $\frac{\partial P_2}{\partial e_2}|_{\rho_2}$ can be obtained when the gas and solid state relations are specified.

After the required calculations are performed, the following expression is obtained for $\mathbf{A}$:

$$\mathbf{A} = \begin{bmatrix}
0 & 1 & 0 & 0 & 0 & 0 & 0 & 0 & 0 \\
c_1^2 - u_1^2 - \left(H_1 - u_1^2\right)\Gamma_1 & 2u_1 - u_1\Gamma_1 & \Gamma_1 & -\rho_1\eta_1/\rho_2 & 0 & 0 & \rho_1\eta_1/(\rho_2\phi_2) & 0 & 0 \\
u_1\left(c_1^2 - H_1\right) - u_1\left(H_1 - u_1^2\right)\Gamma_1 & H_1 - u_1^2\Gamma_1 & u_1 + u_1\Gamma_1 & -u_1\rho_1\eta_1/\rho_2 & 0 & 0 & u_1\rho_1\eta_1/(\rho_2\phi_2) & 0 & 0 \\
0 & 0 & 0 & 0 & 1 & 0 & 0 & 0 & 0 \\
0 & 0 & 0 & c_2^2 - u_2^2 - \left(H_2 - u_2^2\right)\Gamma_2 + \eta_2 & 2u_2 - u_2\Gamma_2 & \Gamma_2 & -\eta_2/\phi_2 & 0 & 0 \\
0 & 0 & 0 & u_2\left(c_2^2 - u_2^2\right) - u_2\left(H_2 - u_2^2\right)\Gamma_2 + u_2\eta_2 & H_2 - u_2^2\Gamma_2 & u_2 + u_2\Gamma_2 & -u_2\eta_2/\phi_2 & 0 & 0 \\
0 & 0 & 0 & -\phi_2 u_2 & \phi_2 & 0 & u_2 & 0 & 0 \\
0 & 0 & 0 & -u_2 n/(\rho_2\phi_2) & n/(\rho_2\phi_2) & & 0 & u_2 & 0 \\
0 & 0 & 0 & -u_2 I & I & 0 & 0 & 0 & u_2
\end{bmatrix}. \tag{2.35}$$

In Eq. (2.35), the total enthalpies H_1 and H_2 are defined by

$$H_1 \equiv e_1 + \frac{u_1^2}{2} + \frac{P_1}{\rho_1}, \quad H_2 \equiv e_2 + \frac{u_2^2}{2} + \frac{P_2}{\rho_2}. \tag{2.36}$$

Additionally, the following variables are introduced for compactness:

$$\eta_1 \equiv c_1^2 - (\Gamma_1 + 1)\frac{P_1}{\rho_1}, \quad \eta_2 \equiv c_2^2 - (\Gamma_2 + 1)\frac{P_2}{\rho_2}. \tag{2.37}$$

Here, it is noted that for a calorically perfect ideal gas and solid, $c_i^2 = \gamma_i \frac{P_i}{\rho_i}$ and $\Gamma_i = \gamma_i - 1$ $(i = 1, 2)$, where γ_i is the specific heat ratio; consequently, $\eta_{1,2} \equiv 0$. Terms in Eq. (2.35) corresponding to the derivatives of the mass, momentum, and energy flux components with respect to the conserved mass, momentum, and energy variables for each phase are similar in form to the derivatives given by Glaister [18] for a single-phase system.

The eigenvalues and right eigenvectors of $\mathbf{A}$, $\lambda^{(j)}$ $(j = 1, \ldots, 9)$ and $\mathbf{r}^{(j)}$, respectively, are solutions of the eigenvalue problem

$$\mathbf{A} \cdot \mathbf{r}^{(j)} = \lambda^{(j)} \mathbf{r}^{(j)}. \tag{2.38}$$

Using matrix notation, the right eigenvalue problem can be concisely expressed as

$$\mathbf{AR} = \mathbf{R\Lambda}, \tag{2.39}$$

where $\mathbf{R}$ is the 9×9 matrix whose columns consist of the right eigenvectors, and $\mathbf{\Lambda}$ is the 9×9 diagonal matrix of eigenvalues; i.e.,

$$\mathbf{R} \equiv \left[\mathbf{r}^{(1)} \middle| \mathbf{r}^{(2)} \middle| \cdots \middle| \mathbf{r}^{(9)}\right], \quad \mathbf{\Lambda} \equiv \begin{bmatrix} \lambda^{(1)} & 0 & \cdots & 0 \\ 0 & \lambda^{(2)} & \cdots & 0 \\ \vdots & \vdots & \ddots & \vdots \\ 0 & 0 & \cdots & \lambda^{(9)} \end{bmatrix}. \tag{2.40}$$

The eigenvalues are determined to be

$$\begin{aligned} &\lambda^{(1)} = u_1, \quad \lambda^{(2)} = u_1 + c_1, \quad \lambda^{(3)} = u_1 - c_1, \\ &\lambda^{(4)} = u_2, \quad \lambda^{(5)} = u_2 + c_2, \quad \lambda^{(6)} = u_2 - c_2, \\ &\lambda^{(7)} = u_2, \quad \lambda^{(8)} = u_2, \qquad \lambda^{(9)} = u_2, \end{aligned} \tag{2.41}$$

and the corresponding right eigenvectors are determined to be

$$\mathbf{r}^{(1)} = \left[1, u_1, H_1 - c_1^2/\Gamma_1, 0, 0, 0, 0, 0, 0\right]^T, \tag{2.42}$$

$$\mathbf{r}^{(2)} = [1, u_1 + c_1, H_1 + u_1 c_1, 0, 0, 0, 0, 0, 0]^T, \tag{2.43}$$

$$\mathbf{r}^{(3)} = [1, u_1 - c_1, H_1 - u_1 c_1, 0, 0, 0, 0, 0, 0]^T, \tag{2.44}$$

$$\mathbf{r}^{(4)} = \left[0, 0, 0, 1, u_2, H_2 - c_2^2/\Gamma_2, \phi_2, 0, 0\right]^T, \tag{2.45}$$

$$\mathbf{r}^{(5)} = [0, 0, 0, 1, u_2 + c_2, H_2 + u_2 c_2, \phi_2, n/(\rho_2 \phi_2), I]^T, \tag{2.46}$$

$$\mathbf{r}^{(6)} = [0, 0, 0, 1, u_2 - c_2, H_2 - u_2 c_2, \phi_2, n/(\rho_2 \phi_2), I]^T, \tag{2.47}$$

$$\mathbf{r}^{(7)} = \left[\frac{\rho_1\eta_1}{\rho_2\phi_2\big((u_2-u_1)^2-c_1^2\big)}, \frac{\rho_1\eta_1 u_2}{\rho_2\phi_2\big((u_2-u_1)^2-c_1^2\big)}, \right.$$
$$\left. \frac{\rho_1\eta_1\big(H_1+u_1u_2-u_1^2\big)}{\rho_2\phi_2\big((u_2-u_1)^2-c_1^2\big)}, 0, 0, \frac{\eta_2}{\phi_2\Gamma_2}, 1, 0, 0\right]^T, \tag{2.48}$$

$$\mathbf{r}^{(8)} = [0, 0, 0, 0, 0, 0, 0, 1, 0]^T, \tag{2.49}$$

$$\mathbf{r}^{(9)} = [0, 0, 0, 0, 0, 0, 0, 0, 1]^T. \tag{2.50}$$

The left eigenvectors of $\mathbf{A}$, $\mathbf{l}^{(j)}$ ($j = 1, \ldots, 9$), are solutions of the eigenvalue problem

$$\mathbf{l}^{(j)} \cdot \mathbf{A} = \lambda^{(j)}\mathbf{l}^{(j)}. \tag{2.51}$$

Using matrix notation, the left eigenvalue problem can be concisely expressed as

$$\mathbf{LA} = \mathbf{\Lambda L}, \tag{2.52}$$

where $\mathbf{L}$ is the 9×9 matrix whose rows consists of the left eigenvectors; i.e.,

$$\mathbf{L} \equiv \begin{bmatrix} \mathbf{l}^{(1)} \\ \mathbf{l}^{(2)} \\ \vdots \\ \mathbf{l}^{(9)} \end{bmatrix}. \tag{2.53}$$

The left eigenvectors are given by

$$\mathbf{l}^{(1)} = \frac{1}{c_1^2}\big[\big(H_1-u_1^2\big)\Gamma_1, u_1\Gamma_1, -\Gamma_1, 0, 0, 0, 0, 0, 0\big], \tag{2.54}$$

$$\mathbf{l}^{(2)} = \frac{1}{2c_1^2}\left[-\big(H_1-u_1^2\big)\Gamma_1 + c_1(c_1-u_1), c_1-u_1\Gamma_1, \Gamma_1, \frac{\rho_1\eta_1c_1}{\rho_2(u_2-(u_1+c_1))}, 0, 0, \right.$$
$$\left. -\frac{\rho_1\eta_1c_1}{\rho_2\phi_2(u_2-(u_1+c_1))}, 0, 0\right], \tag{2.55}$$

$$\mathbf{l}^{(3)} = \frac{1}{2c_1^2}\left[-\big(H_1-u_1^2\big)\Gamma_1 + c_1(c_1+u_1), -c_1-u_1\Gamma_1, \Gamma_1, -\frac{\rho_1\eta_1c_1}{\rho_2(u_2-(u_1-c_1))}, 0, 0, \right.$$
$$\left. \frac{\rho_1\eta_1c_1}{\rho_2\phi_2(u_2-(u_1-c_1))}, 0, 0\right], \tag{2.56}$$

$$\mathbf{l}^{(4)} = \frac{1}{c_2^2}\big[0, 0, 0, \big(H_2-u_2^2\big)\Gamma_2 - \eta_2, u_2\Gamma_2, -\Gamma_2, \eta_2/\phi_2, 0, 0\big], \tag{2.57}$$

$$\mathbf{l}^{(5)} = \frac{1}{2c_2^2}\big[0, 0, 0, -\big(H_2-u_2^2\big)\Gamma_2 + c_2(c_2-u_2) + \eta_2, c_2-u_2\Gamma_2, \Gamma_2, -\eta_2/\phi_2, 0, 0\big], \tag{2.58}$$

$$\mathbf{l}^{(6)} = \frac{1}{2c_2^2}\big[0, 0, 0, -\big(H_2-u_2^2\big)\Gamma_2 + c_2(c_2+u_2) + \eta_2, -c_2-u_2\Gamma_2, \Gamma_2, -\eta_2/\phi_2, 0, 0\big], \tag{2.59}$$

$$\mathbf{l}^{(7)} = [0, 0, 0, -\phi_2, 0, 0, 1, 0, 0], \tag{2.60}$$

$$\mathbf{l}^{(8)} = \frac{n}{\rho_2\phi_2 c_2^2}\left[0, 0, 0, \left(H_2 - u_2^2\right)\Gamma_2 - c_2^2 - \eta_2, u_2\Gamma_2, -\Gamma_2, \eta_2/\phi_2, \rho_2\phi_2 c_2^2/n, 0\right], \tag{2.61}$$

$$\mathbf{l}^{(9)} = [0, 0, 0, -I, 0, 0, 0, 0, 1]. \tag{2.62}$$

Each grouping $(\lambda, \mathbf{r}, \mathbf{l})^{(j)}$ $(j = 1, \ldots, 9)$ is associated with a different mode of wave propagation. In particular, $(\lambda, \mathbf{r}, \mathbf{l})^{(1)}$, $(\lambda, \mathbf{r}, \mathbf{l})^{(2)}$, and $(\lambda, \mathbf{r}, \mathbf{l})^{(3)}$ are associated with the propagation of entropy waves, forward traveling acoustic waves, and backward traveling acoustic waves in the gas, respectively; $(\lambda, \mathbf{r}, \mathbf{l})^{(4)}$, $(\lambda, \mathbf{r}, \mathbf{l})^{(5)}$, and $(\lambda, \mathbf{r}, \mathbf{l})^{(6)}$ are associated with the propagation of entropy waves, forward traveling acoustic waves, and backward traveling acoustic waves in the solid, respectively; and $(\lambda, \mathbf{r}, \mathbf{l})^{(7)}$, $(\lambda, \mathbf{r}, \mathbf{l})^{(8)}$, and $(\lambda, \mathbf{r}, \mathbf{l})^{(9)}$ are associated with the propagation of infinitesimal disturbances in the volume fraction, the particle number density, and the ignition variable, respectively.

As shown in Ref. [22], the gas entropy field, solid entropy field, compaction field, number density field, and ignition field are linearly degenerate since $\nabla_q \lambda^{(j)} \cdot \mathbf{r}^{(j)} \equiv 0$ for all $\mathbf{q}$, where $\nabla_q = [\partial(\,)/\partial q_1, \ldots, \partial(\,)/\partial q_9]$. The gas and solid acoustic fields are genuinely nonlinear provided that

$$\left.\frac{\partial^2 P_1}{\partial \mu_1^2}\right|_{s_1} \neq 0 \quad \text{and} \quad \left.\frac{\partial^2 P_2}{\partial \mu_2^2}\right|_{s_2} \neq 0,$$

where μ_1 and μ_2 are the specific volumes of the gas and solid. Each of these conditions is identical to the convexity requirement for genuinely nonlinear acoustic fields for the Euler equations of gas dynamics [12, 66]. The distinction between degenerate and nonlinear characteristic fields is important since discontinuities cannot evolve in degenerate fields from smooth initial data.

Since the eigenvalues given by Eq. (2.41) are real but not distinct, the model equations constitute a nonstrictly hyperbolic system provided that the right eigenvectors [Eqs. (2.42)–(2.49)] are linearly independent. Linear independence requires that the right eigenvector matrix $\mathbf{R}$ be nonsingular or, equivalently, that its inverse exist. Inspection of $\mathbf{R}^{-1}$ $(=\mathbf{L})$, whose rows consist of the left eigenvectors [Eqs. (2.54)–(2.61)], indicates that the right eigenvectors are linearly independent except at the singular points $\phi_2 = 0$ and $u_2 = u_1 \pm c_1$.

For $\phi_2 = 0$, it is seen that the forward and backward acoustic eigenvectors for the solid, $\mathbf{r}^{(5)}$ and $\mathbf{r}^{(6)}$ respectively, degenerate (upon proper scaling) into the particle number density eigenvector $\mathbf{r}^{(8)}$:

$$\lim_{\phi_2 \to 0}\left[\frac{\rho_2\phi_2}{n}\mathbf{r}^{(5)}\right] = \lim_{\phi_2 \to 0}\left[\frac{\rho_2\phi_2}{n}\mathbf{r}^{(6)}\right] = \mathbf{r}^{(8)}. \tag{2.63}$$

The time-dependent analysis performed in this study does not formally consider the limit $\phi_2 \to 0$; rather, the singularity is avoided by terminating combustion when the solid volume fraction reaches a specified minimum value. As such, the solid particles are assumed to have an inert core of small diameter. It is noted that this complete combustion singularity also exist in steady-state models of two-phase detonation [22, 45] and, within the context of those models, is shown to be inconsequential.

For $u_2 = u_1 + c_1$ and $u_2 = u_1 - c_1$, it is seen that the compaction eigenvector $\mathbf{r}^{(7)}$ degenerates (upon proper scaling) into the forward and backward acoustic eigenvectors of the gas, $\mathbf{r}^{(2)}$ and $\mathbf{r}^{(3)}$, respectively:

$$\lim_{u_2 \to u_1 + c_1} \left[\frac{\rho_2 \phi_2 \left((u_2 - u_1)^2 - c_1^2 \right)}{\rho_1 \eta_1} \mathbf{r}^{(7)} \right] = \mathbf{r}^{(2)}, \tag{2.64}$$

$$\lim_{u_2 \to u_1 - c_1} \left[\frac{\rho_2 \phi_2 \left((u_2 - u_1)^2 - c_1^2 \right)}{\rho_1 \eta_1} \mathbf{r}^{(7)} \right] = \mathbf{r}^{(3)}. \tag{2.65}$$

Inspection of Eqs. (2.55) and (2.56) shows that the sonic singularities, corresponding to $u_2 = u_1 \pm c_1$, are removed for $\eta_1 \equiv 0$; as already mentioned, this condition results when a calorically perfect ideal equation of state is used for the gas. In this case, $\mathbf{r}^{(7)}$ reduces to

$$\mathbf{r}_{\mathrm{IG}}^{(7)} = [0, 0, 0, 0, 0, \eta_2/(\phi_2 \Gamma_2), 1, 0, 0]^T.$$

Thus, for $\eta_1 \neq 0$, the model equations constitute a nonstrictly hyperbolic system of equations that contain a parabolic degeneracy on the manifolds $\phi_2 = 0$ and $u_2 = u_1 \pm c_1$ in phase space.

Similar singularities have been identified in the two-phase model proposed by Baer and Nunziato [3]; a detailed discussion is given by Embid and Baer [15]. The physical interpretation of these singular points is unclear. Embid and Baer suggest that the sonic singularities arise since, at the pore level, two-phase granular flow is analogous to flow in a moving duct of variable cross-sectional area; a choked flow condition is reached when the relative flow is sonic. Furthermore, Embid and Baer suggested that nonlinear resonant interactions between the compaction mode, $(\lambda, \mathbf{r}, \mathbf{l})^{(7)}$, and the related gas acoustic mode, $(\lambda, \mathbf{r}, \mathbf{l})^{(2)}$ or $(\lambda, \mathbf{r}, \mathbf{l})^{(3)}$, may occur near these singular points; such resonant interactions are discussed by Isaacson and Temple [29] for a general inhomogeneous system of conservation laws. Based on this premise, Embid *et al.* [16] and Embid and Majda [17] developed and analyzed an asymptotic model describing transition to detonation in granulated reactive solids. It is demonstrated in Ref. [17] that the asymptotic model does predict the development of resonant gas acoustic hot spots which may influence the DDT process.

3. NUMERICAL METHOD

The numerical method is formulated in this section. First, a brief discussion of the two-phase Riemann problem is given, and an approximate solution is formulated based on the exact solution of the linearized two-phase Riemann problem. Next, the implementation of the approximate solution within the framework of a conservative, upwind numerical algorithm for solving nonlinear convection in the gas and solid is given. Since this transport mechanism is responsible for the evolution of discontinuities, it is important that the method accurately predict convection effects. Last, the numerical method used to solve the system of equations governing local phase interaction processes is formulated, and the numerical splitting technique used to couple this method with the upwind method for nonlinear convection is given.

3.1. *The Two-Phase Riemann Problem*

We consider the initial-value problem (IVP)

$$\frac{\partial \mathbf{q}}{\partial t} + \frac{\partial \mathbf{f}(\mathbf{q})}{\partial x} = 0, \tag{3.1}$$

$$\mathbf{q}_o(x) = \begin{cases} \mathbf{q}_L & \text{for } x < 0 \\ \mathbf{q}_R & \text{for } x > 0, \end{cases} \tag{3.2}$$

where $\mathbf{q} \in \Re^9$, $\mathbf{f}$: $\Re^9 \to \Re^9$, $x \in (-\infty, \infty)$, and $t \in [0, \infty)$. The discontinuity in the initial data is defined by constant states, $\mathbf{q}_L$ and $\mathbf{q}_R$ ($\mathbf{q}_L \neq \mathbf{q}_R$), where subscripts L and R are used to indicate the states to the left and right of the discontinuity, respectively. We refer to the IVP defined by Eqs. (3.1) and (3.2), which governs nonlinear convection in the gas and solid, as the two-phase Riemann problem.

The various waves that compose a typical solution of the two-phase Riemann problem are shown in the x/t diagram of Fig. 2. Here, it is assumed that both the gas and the solid pressure associated with the state $\mathbf{q}_L$ are higher than that associated with the state $\mathbf{q}_R$. The initial discontinuity is located at $x = 0$, and the solution evolves for $t > 0$. The resulting waves separate regions having different constant states. Due to the absence of phase interaction processes, physical diffusion, and physical boundaries, the solution has a self-similar form; e.g., it can be expressed as a function of the similarity variable x/t. Associated with each phase is a shock, a contact discontinuity (entropy wave), and a rarefaction (expansion wave). The shocks, which are driven by the high-pressure state $\mathbf{q}_L$, propagate to the right into the low-pressure region. The shocks are followed by right-propagating contact discontinuities which separate regions having different entropy. Since the gas and solid entropy are constant through their respective rarefactions, the gas and solid entropy to the left of their respective contact discontinuities are associated with the state $\mathbf{q}_L$, while the gas and solid entropy to the right of the contact discontinuities are associated with the shocked gas and solid states. Also, a discontinuity in particle number density advects with the solid contact discontinuity, as does the initial discontinuity in the volume fraction and the ignition variable (if a jump in

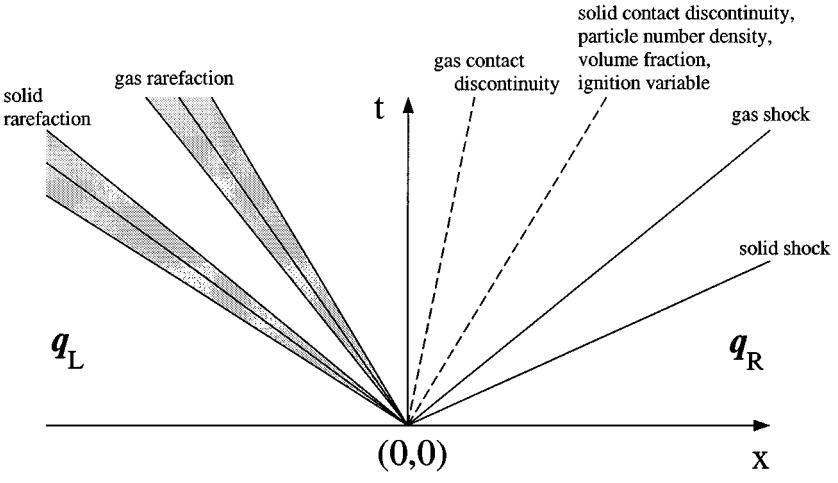

FIG. 2. Sketch of a typical solution of the two-phase Riemann problem.

the volume fraction and the ignition variable is prescribed across the initial discontinuity). Rarefactions, which propagate to the left into the high-pressure region, continuously expand the gas and solid from the state $\mathbf{q}_L$ to the constant states to the left of their respective contact discontinuities.

The order of the gas waves relative to the solid waves for the Riemann problem can change depending upon the states $\mathbf{q}_L$ and $\mathbf{q}_R$. However, the order of the waves associated with each phase is maintained in that the contact discontinuity will always separate the shock and rarefaction. In general, the relative movement of the gas waves with respect to the solid waves poses no special problems, but more work needs to be done to verify this claim; this is beyond the scope of this paper. It is plausible, however, that certain initial conditions might result in the evolution of special *compound* discontinuities consisting of (1) a shock in each phase (e.g., if both the gas and solid shocks propagate with the same velocity), (2) a shock in one phase and a contact discontinuity in the other (e.g., if both the gas shock and the solid contact discontinuity propagate at the same velocity), or (3) a contact discontinuity in each phase (e.g., if both contact discontinuities propagate with the same velocity). As shown by Gonthier [22], each of these compound discontinuities satisfies the second law of thermodynamics for the two-phase mixture and is thus physically admissible; however, boundary and initial conditions necessary for their evolution are generally unknown. Further, if the solid contact discontinuity is located within the gas rarefaction wave, then the sonic condition $u_2 = u_1 - c_1$ is locally satisfied at the point where the two waves intersect, and the model equations become parabolic (for a nonideal gas). As such, the wave structure associated with the solution of the Riemann problem may be considerably more complex than illustrated here. In particular, it is noted that for arbitrary $\mathbf{q}_L$ and $\mathbf{q}_R$, a single wave will generally evolve in each characteristic field; such is the case shown in Fig. 2. However, in contrast to the results for strictly hyperbolic systems, Keyfitz and Kranzer [31] have shown that the Riemann problem for a class of nonstrictly hyperbolic systems containing parabolic degeneracies can admit multiple waves in a single characteristic field. A similar result may hold for Eq. (3.1) for certain values of $\mathbf{q}_L$ and $\mathbf{q}_R$. Such anomalies are not accounted for by the numerical method formulated in this paper.

3.2. *Exact Solution of the Linear Two-Phase Riemann Problem*

The approximate solution of the two-phase Riemann problem is closely coupled to the exact solution of the linearized two-phase Riemann problem. As such, we first consider the case where the initial data $\mathbf{q}_L$ and $\mathbf{q}_R$ in Eq. (3.2) are close to a constant reference state $\mathbf{q}^*$. This assumption will be later relaxed to account for arbitrary $\mathbf{q}_L$ and $\mathbf{q}_R$.

For $\mathbf{q}_L$ and $\mathbf{q}_R$ close to $\mathbf{q}^*$, we can linearize Eq. (2.29) by assuming an expansion of the form

$$\mathbf{q}(x,t) = \mathbf{q}^* + \epsilon \mathbf{q}_{(1)}(x,t) + \epsilon^2 \mathbf{q}_{(2)}(x,t) + \cdots, \tag{3.3}$$

where $0 < \epsilon \ll 1$. The following linear system of equations is obtained at the lowest order in ϵ:

$$\epsilon \frac{\partial \mathbf{q}_{(1)}}{\partial t} + \epsilon \mathbf{A}(\mathbf{q}^*) \frac{\partial \mathbf{q}_{(1)}}{\partial x} = 0. \tag{3.4}$$

Or, since $\epsilon \mathbf{q}_{(1)} = \mathbf{q} - \mathbf{q}^* + O(\epsilon^2)$, we have to $O(\epsilon)$

$$\frac{\partial \mathbf{q}}{\partial t} + \mathbf{A}(\mathbf{q}^*) \frac{\partial \mathbf{q}}{\partial x} = 0, \tag{3.5}$$

where $\mathbf{A}(\mathbf{q}^*)$ is the Jacobian matrix evaluated at the constant reference state. This equation, with the initial data of Eq. (3.2), can be solved using standard techniques applicable to linear hyperbolic systems [33, 65]; the following solution for $\mathbf{q}(x,t)$ is obtained,

$$\begin{aligned}\mathbf{q}(x,t) &= \mathbf{q}_L + \sum_{\lambda^{(j)}<x/t} (\nu_{jR} - \nu_{jL})\mathbf{r}^{(j)} \\ &= \mathbf{q}_R - \sum_{\lambda^{(j)}\geq x/t} (\nu_{jR} - \nu_{jL})\mathbf{r}^{(j)},\end{aligned} \tag{3.6}$$

where the scalars ν_{jL} and ν_{jR} are components of the vectors

$$\boldsymbol{\nu}_L \equiv \mathbf{R}^{-1}\mathbf{q}_L \quad \boldsymbol{\nu}_R \equiv \mathbf{R}^{-1}\mathbf{q}_R, \tag{3.7}$$

respectively. Furthermore, since $\mathbf{A}$ is constant for this linear problem, $\mathbf{f} = \mathbf{A}\mathbf{q}$, and we obtain

$$\begin{aligned}\mathbf{f}(x,t) &= \mathbf{f}_L + \sum_{\lambda^{(j)}<x/t} (\nu_{jR} - \nu_{jL})\lambda^{(j)}\mathbf{r}^{(j)} \\ &= \mathbf{f}_R - \sum_{\lambda^{(j)}\geq x/t} (\nu_{jR} - \nu_{jL})\lambda^{(j)}\mathbf{r}^{(j)}.\end{aligned} \tag{3.8}$$

Following Roe and Pike [48] and Glaister [18, 19], the eigenvector coefficients ν_{jL} and ν_{jR} $(j = 1, \ldots, 9)$ are not directly computed using the definitions given in Eq. (3.7). Rather, the differences $\nu_{jR} - \nu_{jL}$ are approximated by the coefficients $\alpha^{(j)}$ $(j = 1, \ldots, 9)$, which are determined such that each component of the vector equation

$$\delta(\mathbf{q}) = \sum_{j=1}^{9} \alpha^{(j)}\mathbf{r}^{(j)} \tag{3.9}$$

is satisfied to within $O[\delta(q_j)^2] \sim O(\epsilon^2)$, and that each component of the vector equation

$$\delta(\mathbf{f}) = \sum_{j=1}^{9} \alpha^{(j)}\lambda^{(j)}\mathbf{r}^{(j)} \tag{3.10}$$

is setisfied to within $O[\delta(f_j)^2] \sim O(\epsilon^2)$, where the difference operator is defined by $\delta(\bullet) \equiv (\bullet)_R - (\bullet)_L$. Expressions for $\alpha^{(j)}$ $(j = 1, \ldots, 9)$, derived in Appendix A, are given by

$$\alpha^{(1)} = \delta(\rho_1\phi_1) - \frac{1}{c_1^2}\delta(P_1\phi_1) - \frac{\rho_1\eta_1}{c_1^2}\delta(\phi_1), \tag{3.11}$$

$$\alpha^{(2)} = \frac{1}{2c_1^2}\delta(P_1\phi_1) + \frac{\rho_1\phi_1}{2c_1}\delta(u_1) + \left(\frac{u_2 - u_1}{u_2 - (u_1 + c_1)}\right)\frac{\rho_1\eta_1}{2c_1^2}\delta(\phi_1), \tag{3.12}$$

$$\alpha^{(3)} = \frac{1}{2c_1^2}\delta(P_1\phi_1) - \frac{\rho_1\phi_1}{2c_1}\delta(u_1) + \left(\frac{u_2 - u_1}{u_2 - (u_1 - c_1)}\right)\frac{\rho_1\eta_1}{2c_1^2}\delta(\phi_1), \tag{3.13}$$

$$\alpha^{(4)} = \delta(\rho_2\phi_2) - \frac{1}{c_2^2}\delta(P_2\phi_2), \tag{3.14}$$

$$\alpha^{(5)} = \frac{1}{2c_2^2}\delta(P_2\phi_2) + \frac{\rho_2\phi_2}{2c_2}\delta(u_2), \tag{3.15}$$

$$\alpha^{(6)} = \frac{1}{2c_2^2}\delta(P_2\phi_2) - \frac{\rho_2\phi_2}{2c_2}\delta(u_2), \tag{3.16}$$

$$\alpha^{(7)} = \rho_2\phi_2\delta(\phi_2), \tag{3.17}$$

$$\alpha^{(8)} = \delta(n) - \frac{n}{\rho_2\phi_2 c_2^2}\delta(P_2\phi_2), \tag{3.18}$$

$$\alpha^{(9)} = \rho_2\phi_2\delta(I) + I\delta(\rho_2\phi_2) - \frac{I}{c_2^2}\delta(P_2\phi_2). \tag{3.19}$$

Here, it is again noted that these expressions are to be evaluated at the constant reference state $\mathbf{q}^*$. The expressions for $\alpha^{(2)}$ [Eq. (3.12)] and $\alpha^{(3)}$ [Eq. (3.13)] are singular when $u_2 = u_1 + c_1$ and $u_2 = u_1 - c_1$, respectively; also, the expression for $\alpha^{(8)}$ [Eq. (3.18)] is singular when $\phi_2 = 0$. These points correspond to the sonic and complete combustion singularities discussed in the previous section. At these points, the model equations become parabolic, and the eigenvector expansions given by Eqs. (3.9) and (3.10) are no longer valid. The methodology used to suppress numerical instabilities at these points is discussed at the end of this section.

3.3. *Approximate Solution of the Nonlinear Two-Phase Riemann Problem*

An approximate solution of the nonlinear two-phase Riemann problem for arbitrary $\mathbf{q}_L$ and $\mathbf{q}_R$ will now be formulated. Following Roe [49] and Glaister [18], it is desirable to construct the approximate solution such that the following criteria are satisfied.

1. The approximate solution reduces to the exact solution of the linear Riemann problem as $\mathbf{q}_R \to \mathbf{q}_L \to \mathbf{q}$.
2. The approximate solution is derived from a hyperbolic system of equations.
3. The Rankine–Hugoniot relations are satisfied across all discontinuities.

In essence, these criteria stipulate that the approximate solution be consistent with the solution of the original system of hyperbolic equations.

The solution of the linear Riemann problem satisfies the above criteria. As such, it is plausible to use this solution as a basis for constructing the approximate solution. To this end, we require that the approximate solution have the same functional form as the solution of the linear Riemann problem evaluated at an average state $\tilde{\mathbf{q}}$ which is different from the reference state $\mathbf{q}^*$. The problem then reduces to one of properly defining $\tilde{\mathbf{q}}$ as a function of the arbitrary initial data $\mathbf{q}_L$ and $\mathbf{q}_R$.

We first reexpress the solution of the linear Riemann problem in a form which better facilitates the derivation of the approximate solution. In particular, we reexpress the solution of the linear problem in terms of the quantities ϕ_1, u_1, e_1, ϕ_2, u_2, e_2, n, and I and the new quantities $(\rho_1\phi_1)$, $(P_1\phi_1)$, $(\rho_2\phi_2)$, $(P_2\phi_2)$. These latter quantities are the partial density and partial pressure of the gas and solid, respectively. Also, the derivatives

$$F_{i_{\rho_i\phi_i}} \equiv \left.\frac{\partial F_i}{\partial(\rho_i\phi_i)}\right|_{\phi_i,e_i}, \quad F_{i_{\phi_i}} \equiv \left.\frac{\partial F_i}{\partial\phi_i}\right|_{(\rho_i\phi_i),e_i}, \quad \text{and} \quad F_{i_{e_i}} \equiv \left.\frac{\partial F_i}{\partial e_i}\right|_{(\rho_i\phi_i),\phi_i} \quad (i = 1, 2)$$

are introduced, where the F_i denote the functional relationships $P_i\phi_i = F_i(\rho_i\phi_i, \phi_i, e_i)$ obtained by multiplying Eqs. (2.17) and (2.18) by ϕ_1 and ϕ_2, respectively, and expressing the results in terms of the desired quantities. We then seek to define $\tilde{\mathbf{q}}$ in terms of the average

quantities $\widetilde{\rho_1\phi_1}$, $\tilde{v}_1$, $\tilde{e}_1$, $\tilde{H}_1$, $\tilde{F}_{1_{\rho 1\phi 1}}$, $\tilde{F}_{1_{\phi 1}}$, $\tilde{F}_{1_{e1}}$, $\widetilde{\rho_2\phi_2}$, $\tilde{\phi}_2$, $\tilde{v}_2$, $\tilde{e}_2$, $\tilde{H}_2$, $\tilde{F}_{2_{\rho 2\phi 2}}$, $\tilde{F}_{2_{\phi 2}}$, $\tilde{F}_{2_{e2}}$, $\tilde{n}$, and $\tilde{I}$, which are functions of $\mathbf{q}_L$ and $\mathbf{q}_R$, such that the following algebraic equations are identically satisfied [average quantities are denoted by $(\tilde{\bullet})$ throughout this analysis],

$$\Delta(\mathbf{q}) = \sum_{j=1}^{9} \tilde{\alpha}^{(j)} \tilde{\mathbf{r}}^{(j)}, \tag{3.20}$$

$$\Delta(\mathbf{f}) = \sum_{j=1}^{9} \tilde{\alpha}^{(j)} \tilde{\lambda}^{(j)} \tilde{\mathbf{r}}^{(j)}, \tag{3.21}$$

where

$$\tilde{\lambda}^{(1),(2),\ldots,(9)} = \tilde{v}_1, \tilde{v}_1 + \tilde{c}_1, \tilde{v}_1 - \tilde{c}_1, \tilde{v}_2, \tilde{v}_2 + \tilde{c}_2, \tilde{v}_2 - \tilde{c}_2, \tilde{v}_2, \tilde{v}_2, \tilde{v}_2, \tag{3.22}$$

$$\tilde{\mathbf{r}}^{(1)} = \left[1, \tilde{v}_1, \tilde{H}_1 - \tilde{c}_1^2/\tilde{\Gamma}_1, 0, 0, 0, 0, 0, 0\right]^T, \tag{3.23}$$

$$\tilde{\mathbf{r}}^{(2)} = [1, \tilde{v}_1 + \tilde{c}_1, \tilde{H}_1 + \tilde{v}_1\tilde{c}_1, 0, 0, 0, 0, 0, 0]^T, \tag{3.24}$$

$$\tilde{\mathbf{r}}^{(3)} = [1, \tilde{v}_1 - \tilde{c}_1, \tilde{H}_1 - \tilde{v}_1\tilde{c}_1, 0, 0, 0, 0, 0, 0]^T, \tag{3.25}$$

$$\tilde{\mathbf{r}}^{(4)} = \left[0, 0, 0, 1, \tilde{v}_2, \tilde{H}_2 - \tilde{c}_2^2/\tilde{\Gamma}_2, \tilde{\phi}_2, 0, 0\right]^T, \tag{3.26}$$

$$\tilde{\mathbf{r}}^{(5)} = [0, 0, 0, 1, \tilde{v}_2 + \tilde{c}_2, \tilde{H}_2 + \tilde{v}_2\tilde{c}_2, \tilde{\phi}_2, \tilde{n}/\widetilde{\rho_2\phi_2}, \tilde{I}]^T, \tag{3.27}$$

$$\tilde{\mathbf{r}}^{(6)} = [0, 0, 0, 1, \tilde{v}_2 - \tilde{c}_2, \tilde{H}_2 - \tilde{v}_2\tilde{c}_2, \tilde{\phi}_2, \tilde{n}/\widetilde{\rho_2\phi_2}, \tilde{I}]^T, \tag{3.28}$$

$$\tilde{\mathbf{r}}^{(7)} = \left[-\frac{\tilde{F}_{1_{\phi 1}}}{\widetilde{\rho_2\phi_2}\left((\tilde{v}_2 - \tilde{v}_1)^2 - \tilde{c}_1^2\right)}, -\frac{\tilde{F}_{1_{\phi 1}}\tilde{v}_2}{\widetilde{\rho_2\phi_2}\left((\tilde{v}_2 - \tilde{v}_1)^2 - \tilde{c}_1^2\right)}, -\frac{\tilde{F}_{1_{\phi 1}}\left(\tilde{H}_1 + \tilde{v}_1\tilde{v}_2 - \tilde{v}_1^2\right)}{\widetilde{\rho_2\phi_2}\left((\tilde{v}_2 - \tilde{v}_1)^2 - \tilde{c}_1^2\right)}, 0, 0, -\frac{\tilde{F}_{2_{\phi 2}}}{\widetilde{\rho_2\phi_2}\tilde{\Gamma}_2}, 1, 0, 0\right]^T, \tag{3.29}$$

$$\tilde{\mathbf{r}}^{(8)} = [0, 0, 0, 0, 0, 0, 0, 1, 0]^T, \tag{3.30}$$

$$\tilde{\mathbf{r}}^{(9)} = [0, 0, 0, 0, 0, 0, 0, 0, 1]^T, \tag{3.31}$$

$$\tilde{\alpha}^{(1)} = \Delta(\rho_1\phi_1) - \frac{1}{\tilde{c}_1^2}\Delta(P_1\phi_1) + \frac{\tilde{F}_{1_{\phi 1}}}{\tilde{c}_1^2}\Delta(\phi_1), \tag{3.32}$$

$$\tilde{\alpha}^{(2)} = \frac{1}{2\tilde{c}_1^2}\Delta(P_1\phi_1) + \frac{\widetilde{\rho_1\phi_1}}{2\tilde{c}_1}\Delta(u_1) - \left(\frac{\tilde{v}_2 - \tilde{v}_1}{\tilde{v}_2 - (\tilde{v}_1 + \tilde{c}_1)}\right)\frac{\tilde{F}_{1_{\phi 1}}}{2\tilde{c}_1^2}\Delta(\phi_1), \tag{3.33}$$

$$\tilde{\alpha}^{(3)} = \frac{1}{2\tilde{c}_1^2}\Delta(P_1\phi_1) - \frac{\widetilde{\rho_1\phi_1}}{2\tilde{c}_1}\Delta(u_1) - \left(\frac{\tilde{v}_2 - \tilde{v}_1}{\tilde{v}_2 - (\tilde{v}_1 - \tilde{c}_1)}\right)\frac{\tilde{F}_{1_{\phi 1}}}{2\tilde{c}_1^2}\Delta(\phi_1), \tag{3.34}$$

$$\tilde{\alpha}^{(4)} = \Delta(\rho_2\phi_2) - \frac{1}{\tilde{c}_2^2}\Delta(P_2\phi_2), \tag{3.35}$$

$$\tilde{\alpha}^{(5)} = \frac{1}{2\tilde{c}_2^2}\Delta(P_2\phi_2) + \frac{\widetilde{\rho_2\phi_2}}{2\tilde{c}_2}\Delta(u_2), \tag{3.36}$$

$$\tilde{\alpha}^{(6)} = \frac{1}{2\tilde{c}_2^2}\Delta(P_2\phi_2) - \frac{\widetilde{\rho_2\phi_2}}{2\tilde{c}_2}\Delta(u_2), \tag{3.37}$$

$$\tilde{\alpha}^{(7)} = \widetilde{\rho_2\phi_2}\Delta(\phi_2), \tag{3.38}$$

$$\tilde{\alpha}^{(8)} = \Delta(n) - \frac{\tilde{n}}{\widetilde{\rho_2\phi_2}\tilde{c}_2^2}\Delta(P_2\phi_2), \tag{3.39}$$

$$\tilde{\alpha}^{(9)} = \widetilde{\rho_2\phi_2}\Delta(I) + \tilde{I}\Delta(\rho_2\phi_2) - \frac{\tilde{I}}{\tilde{c}_2^2}\Delta(P_2\phi_2), \tag{3.40}$$

and $\tilde{c}_1^2$, $\tilde{c}_2^2$, $\widetilde{P_1\phi_1}$, $\widetilde{P_2\phi_2}$, $\tilde{\Gamma}_1$, and $\tilde{\Gamma}_2$ are given by

$$\tilde{c}_1^2 = \frac{\widetilde{P_1\phi_1}}{\widetilde{\rho_1\phi_1}^2}\tilde{F}_{1_{e1}} + \tilde{F}_{1_{\rho 1\phi 1}}, \quad \tilde{c}_2^2 = \frac{\widetilde{P_2\phi_2}}{\widetilde{\rho_2\phi_2}^2}\tilde{F}_{2_{e2}} + \tilde{F}_{2_{\rho 2\phi 2}}, \tag{3.41}$$

$$\widetilde{P_1\phi_1} = \widetilde{\rho_1\phi_1}\left(\tilde{H}_1 - \tilde{e}_1 - \frac{\tilde{v}_1^2}{2}\right), \quad \widetilde{P_2\phi_2} = \widetilde{\rho_2\phi_2}\left(\tilde{H}_2 - \tilde{e}_2 - \frac{\tilde{v}_2^2}{2}\right), \tag{3.42}$$

$$\tilde{\Gamma}_1 = \frac{1}{\widetilde{\rho_1\phi_1}}\tilde{F}_{1_{e1}}, \quad \tilde{\Gamma}_2 = \frac{1}{\widetilde{\rho_2\phi_2}}\tilde{F}_{2_{e2}}. \tag{3.43}$$

Here, the difference operator is defined by $\Delta(\bullet) \equiv (\bullet)_R - (\bullet)_L$, where the difference $\mathbf{q}_R - \mathbf{q}_L$ is not necessarily small [as opposed to the difference operator $\delta(\bullet)$ defined for the linear Riemann problem]. If suitable averages can be defined, then the approximate solutions $\mathbf{q}(x,t)$ and $\mathbf{f}(x,t)$ are given by

$$\begin{aligned}\mathbf{q}(x,t) &= \mathbf{q}_L + \sum_{\tilde{\lambda}^{(j)}<x/t} \tilde{\alpha}^{(j)}\tilde{\mathbf{r}}^{(j)} \\ &= \mathbf{q}_R - \sum_{\tilde{\lambda}^{(j)}\geq x/t} \tilde{\alpha}^{(j)}\tilde{\mathbf{r}}^{(j)},\end{aligned} \tag{3.44}$$

$$\begin{aligned}\mathbf{f}(x,t) &= \mathbf{f}_L + \sum_{\tilde{\lambda}^{(j)}<x/t} \tilde{\alpha}^{(j)}\tilde{\lambda}^{(j)}\tilde{\mathbf{r}}^{(j)} \\ &= \mathbf{f}_R - \sum_{\tilde{\lambda}^{(j)}\geq x/t} \tilde{\alpha}^{(j)}\tilde{\lambda}^{(j)}\tilde{\mathbf{r}}^{(j)}.\end{aligned} \tag{3.45}$$

Equations (3.20) and (3.21), and Eqs. (3.44) and (3.45) are analogous to Eqs. (3.9) and (3.10), and Eqs. (3.6) and (3.8), respectively.

To define the desired average quantities, it is necessary to solve the nonlinear algebraic problem given by Eqs. (3.20) and (3.21). Though the solution of this problem is nontrivial, closed form expressions can be obtained for the average quantities. The derivation of these quantities is given in Appendix B; the results are summarized below (where $i = 1, 2$):

$$\widetilde{\rho_i\phi_i} \equiv \sqrt{\rho_{iL}\phi_{iL}\rho_{iR}\phi_{iR}}, \tag{3.46}$$

$$\tilde{v}_i \equiv \frac{\sqrt{\rho_{iL}\phi_{iL}}u_{iL} + \sqrt{\rho_{iR}\phi_{iR}}u_{iR}}{\sqrt{\rho_{iL}\phi_{iL}} + \sqrt{\rho_{iR}\phi_{iR}}}, \tag{3.47}$$

$$\tilde{e}_i \equiv \frac{\sqrt{\rho_{iL}\phi_{iL}}e_{iL} + \sqrt{\rho_{iR}\phi_{iR}}e_{iR}}{\sqrt{\rho_{iL}\phi_{iL}} + \sqrt{\rho_{iR}\phi_{iR}}}, \tag{3.48}$$

$$\tilde{H}_i \equiv \frac{\sqrt{\rho_{iL}\phi_{iL}}H_{iL} + \sqrt{\rho_{iR}\phi_{iR}}H_{iR}}{\sqrt{\rho_{iL}\phi_{iL}} + \sqrt{\rho_{iR}\phi_{iR}}}, \tag{3.49}$$

$$\tilde{\phi}_2 \equiv \frac{\sqrt{\rho_{2L}\phi_{2L}}\phi_{2L} + \sqrt{\rho_{2R}\phi_{2R}}\phi_{2R}}{\sqrt{\rho_{2L}\phi_{2L}} + \sqrt{\rho_{2R}\phi_{2R}}}, \tag{3.50}$$

$$\tilde{n} \equiv \frac{\sqrt{\rho_{2L}\phi_{2L}}n_{2R} + \sqrt{\rho_{2R}\phi_{2R}}n_{2L}}{\sqrt{\rho_{2L}\phi_{2L}} + \sqrt{\rho_{2R}\phi_{2R}}}, \tag{3.51}$$

$$\tilde{I} \equiv \frac{\sqrt{\rho_{2L}\phi_{2L}}I_{2L} + \sqrt{\rho_{2R}\phi_{2R}}I_{2R}}{\sqrt{\rho_{2L}\phi_{2L}} + \sqrt{\rho_{2R}\phi_{2R}}}, \tag{3.52}$$

$$\tilde{F}_{i_{\rho_i\phi_i}} \equiv \begin{cases} \big(\frac{1}{4}[F_i(\rho_{iR}\phi_{iR}, \phi_{iR}, e_{1R}) + F_i(\rho_{iR}\phi_{iR}, \phi_{iR}, e_{iL}) + F_i(\rho_{iR}\phi_{iR}, \phi_{iL}, e_{iL}) \\ \quad + F_i(\rho_{iR}\phi_{iR}, \phi_{iL}, e_{iR})] - \frac{1}{4}[F_i(\rho_{iL}\phi_{iL}, \phi_{iR}, e_{iR}) + F_i(\rho_{iL}\phi_{iL}, \phi_{iL}, e_{iR}) \\ \quad + F_i(\rho_{iL}\phi_{iL}, \phi_{iR}, e_{iL}) + F_i(\rho_{iL}\phi_{iL}, \phi_{iL}, e_{iL})]\big)/\Delta(\rho_i\phi_i) \quad \text{if } \Delta(\rho_i\phi_i) \neq 0, \\ \frac{1}{4}\big[\frac{\partial F_i}{\partial(\rho_i\phi_i)}(\rho_i\phi_i, \phi_{iR}, e_{1R}) + \frac{\partial F_i}{\partial(\rho_i\phi_i)}(\rho_i\phi_i, \phi_{iR}, e_{iL}) + \frac{\partial F_i}{\partial(\rho_i\phi_i)}(\rho_i\phi_i, \phi_{iL}, e_{iR}) \\ \quad + \frac{\partial F_i}{\partial(\rho_i\phi_i)}(\rho_i\phi_i, \phi_{iL}, e_{iL})\big], \quad \text{if } \Delta(\rho_i\phi_i) = 0, \end{cases} \tag{3.53}$$

$$\tilde{F}_{i_{\phi_i}} \equiv \begin{cases} \big(\frac{1}{2}[F_i(\rho_{iR}\phi_{iR}, \phi_{iR}, e_{1R}) + F_i(\rho_{iL}\phi_{iL}, \phi_{iR}, e_{iL})] + \frac{1}{2}[F_i(\rho_{iR}\phi_{iR}, \phi_{iL}, e_{iR}) \\ \quad + F_i(\rho_{iL}\phi_{iL}, \phi_{iL}, e_{iL})]\big)/\Delta(\phi_i) \quad \text{if } \Delta(\phi_i) \neq 0, \\ \frac{1}{2}\big[\frac{\partial F_i}{\partial \phi_i}(\rho_{iR}\phi_{iR}, \phi_i, e_{1R}) + \frac{\partial F_i}{\partial \phi_i}(\rho_{iL}\phi_{iL}, \phi_i, e_{iL})\big] \quad \text{if } \Delta(\phi_i) = 0, \end{cases} \tag{3.54}$$

$$\tilde{F}_{i_{e_i}} \equiv \begin{cases} \big(\frac{1}{4}[F_i(\rho_{iR}\phi_{iR}, \phi_{iR}, e_{1R}) + F_i(\rho_{iL}\phi_{iL}, \phi_{iL}, e_{iR}) + F_i(\rho_{iR}\phi_{iR}, \phi_{iL}, e_{iR}) \\ \quad + F_i(\rho_{iL}\phi_{iL}, \phi_{iR}, e_{iR})] - \frac{1}{4}[F_i(\rho_{iR}\phi_{iR}, \phi_{iL}, e_{iL}) + F_i(\rho_{iR}\phi_{iR}, \phi_{iR}, e_{iL}) \\ \quad + F_i(\rho_{iL}\phi_{iL}, \phi_{iR}, e_{iL}) + F_i(\rho_{iL}\phi_{iL}, \phi_{iL}, e_{iL})]\big)/\Delta(e_i) \quad \text{if } \Delta(e_i) \neq 0, \\ \frac{1}{4}\big[\frac{\partial F_i}{\partial e_i}(\rho_{iR}\phi_{iR}, \phi_{iR}, e_i) + \frac{\partial F_i}{\partial e_i}(\rho_{iR}\phi_{iR}, \phi_{iL}, e_i) + \frac{\partial F_i}{\partial e_i}(\rho_{iL}\phi_{iL}, \phi_{iR}, e_i) \\ \quad + \frac{\partial F_i}{\partial e_i}(\rho_{iL}\phi_{iL}, \phi_{iL}, e_i)\big], \quad \text{if } \Delta(e_i) = 0. \end{cases} \tag{3.55}$$

The averages defined by Eqs. (3.46)–(3.52) are similar in form to the "square root" averages defined in Refs. [18, 49]. Though the averages for the thermodynamic derivatives defined by Eqs. (3.53)–(3.55) appear complicated, it is shown in the section on numerical simulations that they lead to relatively simple expressions that can be easily evaluated when the functional form of the equations of state are specified and that the expressions are physically reasonable. However, these expressions may be difficult and/or computationally expensive to evaluate for thermodynamic data given in tabular form. Furthermore, these averages require function evaluations for artificial states constructed from the initial data $\mathbf{q}_L$ and $\mathbf{q}_R$, and it is possible that these states lie outside the range of validity of the thermodynamic data. Glaister [20] has addressed similar deficiencies for his approximate Riemann solution and has modified his solution to overcome these shortcomings. It is possible that similar modifications can be made for the approximate solution outlined here.

It is easy to verify that the three criteria stated above are satisfied by the approximate solution. First, the averages defined by Eqs. (3.46)–(3.55) satisfy the property that $\tilde{\mathbf{q}} \to \mathbf{q}$ as $\mathbf{q}_L \to \mathbf{q}_R \to \mathbf{q}$; consequently, the approximate solution properly reduces to the exact solution of the linear Riemann problem in this limit. Second, since the approximate solution was constructed to have the same mathematical structure as the exact solution of the linear Riemann problem, the approximate solution can be considered to be associated with an

equivalent linear, constant coefficient system of hyperbolic equations (provided that $\tilde{v}_2 \neq \tilde{v}_1 \pm \tilde{c}_1$ and $\tilde{\phi}_2 \neq 0$). As such, the approximate solution has the same physical interpretation as the solution of the linear Riemann problem and consists of (at most) nine discontinuous waves separating seven regions of constant state. Third, the jumps in $\mathbf{q}$ and $\mathbf{f}$ across the jth wave are given by

$$[\mathbf{q}]_j = \tilde{\alpha}^{(j)}\tilde{\mathbf{r}}^{(j)}, \tag{3.56}$$

$$[\mathbf{f}]_j = \tilde{\alpha}^{(j)}\tilde{\lambda}^{(j)}\tilde{\mathbf{r}}^{(j)}. \tag{3.57}$$

Thus, the Rankine–Hugoniot relations are satisfied across the discontinuities since

$$[\mathbf{f}]_j = \tilde{\lambda}^{(j)}[\mathbf{q}]_j.$$

A consequence of this property is that, in the event that $\mathbf{q}_L$ and $\mathbf{q}_R$ can be connected by a single shock or contact discontinuity, the approximate solution agrees with the exact solution of the nonlinear Riemann problem [18, 48]. Last, we note that for $\Delta(\phi_1) = 0$ [or $\Delta(\phi_2) = 0$], the governing equations for the gas and solid, given by Eq. (2.24), decouple. Similarly, the approximate Riemann solution given here decouples for the gas and solid, and the resulting approximate solution for each phase reduces to the approximate solution given by Glaister [18] for a single-phase nonideal system.

3.4. *Implementation of the Numerical Method*

It is required that Eq. (3.1) be expressed in conservative form so that the correct propagation speeds of discontinuities are predicted [33]:

$$\mathbf{Q}_k^{n+1} = \mathbf{Q}_k^n - \frac{\Delta t}{\Delta x}\left[\mathbf{F}_{k+1/2}(\mathbf{Q}^n) - \mathbf{F}_{k-1/2}(\mathbf{Q}^n)\right]. \tag{3.58}$$

Here, it is assumed that the spatial domain is discretized into uniformly spaced nodes located at the points x_k ($k = 1, 2, \ldots$). Each node is located at the center of a computational cell of width Δx. The locations of the left and right boundaries of the kth cell are denoted as $x_{k-1/2}$ and $x_{k+1/2}$, respectively. The vector quantities $\mathbf{Q}_k^n$ and $\mathbf{Q}_k^{n+1}$ are numerical approximations for $\mathbf{q}$ at times t^n and $t^{n+1} = t^n + \Delta t$, respectively, where Δt is a small time increment. The vector quantities $\mathbf{F}_{k\pm1/2}$, which are dependent upon $\mathbf{Q}^n$, are numerical approximations for $\mathbf{f}$ at the cell boundaries $x_{k\pm1/2}$.

The implementation of the approximate Riemann solution within the framework of Godunov's methodology is now described. First, the states $\mathbf{q}_L = \mathbf{Q}_k^n$ and $\mathbf{q}_R = \mathbf{Q}_{k+1}^n$ are defined to the left and right of the computational cell boundary located at $x_{k+1/2}$; this step is the *projection step* of Godunov's methodology. The solution is then allowed to evolve over a small time increment Δt, and the numerical flux $\mathbf{F}_{k+1/2}$ is computed from the approximate Riemann solution; this step is the *evolution step* of Godunov's methodology. The numerical flux is given by either expression in Eq. (3.45) evaluated at $x/t = 0$. Alternatively, averaging the two resulting expressions for the numerical flux gives the following expression for $\mathbf{F}_{k+1/2}$ used in this work:

$$\mathbf{F}_{k+1/2} = \frac{\mathbf{f}\left(\mathbf{Q}_k^n\right) + \mathbf{f}\left(\mathbf{Q}_{k+1}^n\right)}{2} - \frac{1}{2}\left[\sum_{j=1}^{9}\tilde{\alpha}^{(j)}\left|\tilde{\lambda}^{(j)}\right|\tilde{\mathbf{r}}^{(j)}\right]_{k+1/2}. \tag{3.59}$$

The time increment Δt is chosen such that waves associated with neighboring Riemann problems do not interact, giving rise to the Courant–Friedrichs–Lewy (CFL) condition

$$\max_j \left| \frac{\tilde{\lambda}^{(j)} \Delta t}{\Delta x} \right|_{k+1/2} \leq \kappa; \quad j = 1, \ldots, 9; \quad k = 1, 2, \ldots. \tag{3.60}$$

Here, the constant κ, commonly termed the CFL number, lies in the range $0 \leq \kappa \leq 0.5$. The value $\kappa = 0.4$ was used for all computations presented in this paper. Once the numerical flux is computed at each cell boundary, the solution at time $t^{n+1} = t^n + \Delta t$ is obtained from Eq. (3.58); this step is the *reconstruction step* of Godunov's methodology. The process is then repeated to further advance the solution in time.

The approximate solution has three deficiencies which must be addressed. First, since all waves are approximated by discontinuities, rarefaction waves, which have a continuous structure, are not accurately represented. This common deficiency poses no difficulty except for the case when a gas or solid sonic point exists within a gas or solid rarefaction wave, respectively. Various techniques can be used to modify the numerical flux at computational cell boundaries where a sonic rarefaction is predicted. To this end, an entropy criterion is used to detect sonic rarefactions in both the gas and the solid, i.e., if $\lambda^{(j)-} < 0 < \lambda^{(j)+}$, where quantities associated with the constant states immediately to the left and right of the rarefaction shock are labeled with superscript "$-$" and "$+$", respectively. If a sonic rarefaction is detected, we locally employ a numerical flux which has been modified based on the technique proposed by Harten and Hyman [25]. As a comprehensive discussion of this technique is given by LeVeque [33], we refer the reader to this reference for details.

Second, the approximate solution is not uniformly valid since the eigenvector expansions given by Eqs. (3.20) and (3.21) break down near the singularities $\tilde{v}_2 = \tilde{v}_1 \pm \tilde{c}_1$ and $\phi_2 = 0$. Numerical experiments have shown this deficiency to result in severe numerical instabilities near these points. Within the context of the approximate Riemann solution, the sonic singularities $\tilde{v}_2 = \tilde{v}_1 \pm \tilde{c}_1$ occur when the discontinuity in volume fraction, propagating at speed $\tilde{v}_2$, impinges upon either a gas shock or rarefaction, propagating at speed $\tilde{v}_1 + \tilde{c}_1$ or $\tilde{v}_1 - \tilde{c}_1$. For such cases, there may exist complicated wave interactions that are not predicted by the approximate solution. As shown by Keyfitz and Kranzer [31] for a simple mathematical system having similar parabolic degeneracies, such interactions may result in a series of additional waves being produced, with the solution of the Riemann problem consisting of multiple waves in a single characteristic field. For the approximate solution formulated in this paper, it was implicitly assumed that a physically relevant unique solution exists which consists of at most nine waves, one associated with each characteristic field; as such, this assumption may be invalid near the sonic singularities. In order to properly address this issue, a more detailed analysis of the Riemann problem would be required. Here, we accept some uncertainty and choose to only suppress numerical instabilities which are known to occur near these singularities. Also, we note that if no jump in volume fraction exists [i.e., $\Delta(\phi_2) = \Delta(\phi_2) = 0$], then the sonic singularities are inconsequential because the quantities $\tilde{\alpha}^{(2)}\tilde{\mathbf{r}}^{(2)}$, $\tilde{\alpha}^{(3)}\tilde{\mathbf{r}}^{(3)}$, and $\tilde{\alpha}^{(7)}\tilde{\mathbf{r}}^{(7)}$ in the eigenvector expansions remain well defined. This result is easily seen from the definitions given in Eqs. (3.23)–(3.40).

General modifications to the Godunov methodology which are needed to suppress numerical instabilities resulting from a loss of hyperbolicity are discussed by Bell *et al.* [7]. To avoid numerical difficulties near the singularities $u_2 = u_1 \pm c_1$, we adopt a technique that is similar to that proposed in Ref. [7]. In particular, we assume that a sonic singularity

exists if the criterion

$$|\tilde{v}_2 - (\tilde{v}_1 \pm \tilde{c}_1)| < c_\epsilon \tag{3.61}$$

is satisfied, where c_ϵ is a small positive constant. The value $c_\epsilon = 50$ m/s was used for all computations performed in this work. In such instances, we collapse the waves propagating at speed $\tilde{v}_2$ and $\tilde{v}_1 + \tilde{c}_1$ or $\tilde{v}_1 - \tilde{c}_1$ (whichever wave is involved) into a single wave propagating at speed $\tilde{\lambda}^{(\ddagger)} = (\tilde{v}_2 + \tilde{v}_1 \pm \tilde{c}_1)/2$. The jump across this wave, $\tilde{\alpha}^{(\ddagger)}\tilde{\mathbf{r}}^{(\ddagger)}$, is then defined in terms of both the difference $\mathbf{Q}^n_{k+1} - \mathbf{Q}^n_k$ and the jumps across the waves not associated with the sonic singularity. For example, if the singularity is associated with the gas wave propagating at speed $\tilde{\lambda}^{(3)} = \tilde{v}_1 - \tilde{c}_1$, then the following quantities are defined,

$$\begin{aligned}
\tilde{\lambda}^{(\ddagger)} &\equiv \frac{\tilde{v}_2 + \tilde{v}_1 - \tilde{c}_1}{2}, \\
\tilde{\alpha}^{(\ddagger)} &\equiv \left\| \Delta(\mathbf{q}) - \tilde{\alpha}^{(1)}\tilde{\mathbf{r}}^{(1)} - \tilde{\alpha}^{(2)}\mathbf{r}^{(2)} - \tilde{\alpha}^{(5)}\tilde{\mathbf{r}}^{(5)} - \tilde{\alpha}^{(6)}\tilde{\mathbf{r}}^{(6)} \right\|, \\
\tilde{\mathbf{r}}^{(\ddagger)} &\equiv \frac{\Delta(\mathbf{q}) - \tilde{\alpha}^{(1)}\tilde{\mathbf{r}}^{(1)} - \tilde{\alpha}^{(2)}\mathbf{r}^{(2)} - \tilde{\alpha}^{(5)}\tilde{\mathbf{r}}^{(5)} - \tilde{\alpha}^{(6)}\tilde{\mathbf{r}}^{(6)}}{\left\| \Delta\mathbf{q} - \tilde{\alpha}^{(1)}\tilde{\mathbf{r}}^{(1)} - \tilde{\alpha}^{(2)}\mathbf{r}^{(2)} - \tilde{\alpha}^{(5)}\tilde{\mathbf{r}}^{(5)} - \tilde{\alpha}^{(6)}\tilde{\mathbf{r}}^{(6)} \right\|},
\end{aligned} \tag{3.62}$$

where $\| \bullet \|$ is the Euclidean norm. Consequently,

$$\mathbf{Q}^n_{k+1} - \mathbf{Q}^n_k = \sum_{j=1,2,5,6,\ddagger} \tilde{\alpha}^{(j)}\tilde{\mathbf{r}}^{(j)} \tag{3.63}$$

by construction. The following modified numerical flux, denoted by superscript "‡", is proposed:

$$\mathbf{F}^{\ddagger}_{k+1/2} = \frac{\mathbf{f}\left(\mathbf{Q}^n_k\right) + \mathbf{f}\left(\mathbf{Q}^n_{k+1}\right)}{2} - \frac{1}{2}\left[\sum_{j=1,2,5,6,\ddagger} \tilde{\alpha}^{(j)}\left|\tilde{\lambda}^{(j)}\right|\tilde{\mathbf{r}}^{(j)} \right]_{k+1/2}. \tag{3.64}$$

A similar result holds if the singularity is associated with the gas wave propagating at speed $\tilde{\lambda}^{(2)} = \tilde{v}_1 + \tilde{c}_1$. Though the Rankine–Hugoniot relations are not identically satisfied by this newly defined wave (i.e., $[\mathbf{f}]_\ddagger \neq \tilde{\lambda}^{(\ddagger)}[\mathbf{q}]_\ddagger$), they are nearly satisfied; this has been numerically verified. Comparisons of numerical predictions with exact steady solutions for two-phase detonation structures possessing these sonic singularities indicate that this error is inconsequential.

Last, to suppress numerical instabilities near $\phi_2 = 0$, it is necessary to constrain ϕ_2 to be greater than a constant minimum value $\phi_{2\epsilon}$. This is achieved by terminating combustion for $\phi_2 \leq \phi_{2\epsilon}$. A large number of numerical experiments that showed the onset of instability for $\phi_2 \approx 1 \times 10^{-6}$ were performed, though the instability was not severe; thus, the value $\phi_{2\epsilon} = 1 \times 10^{-5}$ was used for all computations performed in this work. This burn termination was determined to have an insignificant affect on both DDT and detonation wave structure. Further, our steady-sate analysis did not require burn termination as the particle radius approached zero without difficulty. As such, the model is well behaved in this limit.

3.5. *Higher-Order Spatial and Temporal Accuracy*

The upwind numerical method outlined in the previous subsection has only nominal first-order spatial accuracy and has first-order temporal accuracy. First-order spatial accuracy is

characteristic of all Godunov-based methods for which the initial state within each computational cell is assumed constant in the *projection step*. In this subsection, approaches used to increase both the spatial and the temporal accuracy of the method are given.

Using the flux-extrapolation methodology of Chakravarthy and Osher [10] for obtaining second-order total-variation-diminishing (TVD) methods, we get the following higher-order numerical flux function,

$$\mathbf{F}^{(H)}_{k+1/2} = \mathbf{F}^{(L)}_{k+1/2} + \frac{1}{2}\sum_{j=1}^{9}\left(d\check{\mathbf{f}}^{(j+)}_{k-1/2} - d\check{\breve{\mathbf{f}}}^{(j-)}_{k+3/2}\right), \tag{3.65}$$

where

$$d\check{\mathbf{f}}^{(j+)}_{k-1/2} = L\left\{\left[\tilde{\lambda}^{(j+)}\tilde{\alpha}^{(j)}\right]_{k-1/2}, \left[\tilde{\lambda}^{(j+)}\tilde{\alpha}^{(j)}\right]_{k+1/2}\right\}\tilde{\mathbf{r}}^{(j)}_{k+1/2},$$

$$d\check{\breve{\mathbf{f}}}^{(j-)}_{k+3/2} = L\left\{\left[\tilde{\lambda}^{(j-)}\tilde{\alpha}^{(j)}\right]_{k+3/2}, \left[\tilde{\lambda}^{(j-)}\tilde{\alpha}^{(j)}\right]_{k+1/2}\right\}\tilde{\mathbf{r}}^{(j)}_{k+1/2}.$$

Here, $\mathbf{F}^{(L)}_{k+1/2}$ denotes the lower-order numerical flux defined in Eq. (3.59). The operator $L\{y, z\}$ is a nonlinear flux limiter which limits the amount of numerical diffusion in $\mathbf{F}^{(H)}_{k+1/2}$ based on the approximate Riemann solution at cell boundaries located immediately to the left ($x_{k-1/2}$) and right ($x_{k+3/2}$) of the boundary at $x_{k+1/2}$. The flux limiter used in this study is Van Leer's limiter [63], which is given by

$$L\{y, z\} = \frac{yz + |yz|}{y + z}.$$

Other limiters exist that could be used in place of Van Leer's limiter, or different limiters could be used for the gas and solid; this limiter was chosen based on numerical experiments that indicated that it can accurately capture discontinuities in both the gas and the solid.

The use of the flux given by Eq. (3.65) in Eq. (3.58) results in an explicit TVD numerical method that has nominally second-order spatial accuracy in smooth regions of the flow, first-order spatial accuracy near discontinuities, and first-order temporal accuracy. The TVD flux given by Eq. (3.65) results in a conditionally stable method provided that an additional constraint on the time step Δt is satisfied (i.e., in addition to the CFL condition) [10]. Thus, it is desirable to increase the temporal accuracy of the method to obtain better stability properties and to eliminate the need to satisfy an additional time step constraint. To this end, the following two-step Runge–Kutta predictor/corrector algorithm is used to advance the solution from t^n to $t^{n+1} = t^n + \Delta t$ [28]:

$$\bar{\mathbf{Q}}_k = \mathbf{Q}^n_k - \frac{\Delta t}{2\Delta x}\left[\mathbf{F}^{(H)}_{k+1/2}(\mathbf{Q}^n) - \mathbf{F}^{(H)}_{k-1/2}(\mathbf{Q}^n)\right],$$

$$\mathbf{Q}^{n+1}_k = \mathbf{Q}^n_k - \frac{\Delta t}{\Delta x}\left[\mathbf{F}^{(H)}_{k+1/2}(\bar{\mathbf{Q}}) - \mathbf{F}^{(H)}_{k-1/2}(\bar{\mathbf{Q}})\right].$$

Here, the first step is the predictor step whereby the solution is allowed to evolve over the time interval $\frac{\Delta t}{2}$, and the second step is the corrector step in which the updated solution is computed using the numerical flux of Eq. (3.65) evaluated in terms of the intermediate solution $\bar{\mathbf{Q}}$. Both the predictor and corrector steps are expressed in the conservative form of Eq. (3.58); as such, conservation is maintained. The resulting method is second-order accurate in time.

3.6. *Numerical Solution of the Full Two-Phase Equations*

The numerical approach used in this study to solve the full model equations is based on the following time-step splitting procedure [62]:

$$\mathbf{Q}_k^{n+2} = \mathcal{L}_c^{\Delta t}\mathcal{L}_s^{2\Delta t}\mathcal{L}_c^{\Delta t}\mathbf{Q}_k^n. \tag{3.66}$$

Here, $\mathbf{Q}^n$ and $\mathbf{Q}^{n+2}$ are the numerical solution at times t^n and t^{n+2}, respectively, $\mathcal{L}_c^{\Delta t}$ is the convective numerical operator, and $\mathcal{L}_s^{2\Delta t}$ is the source numerical operator. The convective operator solves the convection problem using the high-resolution TVD method formulated in the previous section, and the source operator, which is described below, solves the phase interaction terms using a high-order time accurate stiff ODE solver. During the convection steps, the phase interaction processes are suppressed [i.e., $\mathbf{g}(\mathbf{q}) = 0$ in Eq. (2.24)]; likewise, gas and solid convection are suppressed during the source step [i.e., $\frac{\partial \mathbf{f}(\mathbf{q})}{\partial x} = 0$ in Eq. (2.24)]. The splitting procedure requires that the convection step be performed over the time step Δt and that the source step be performed over twice the time step, where Δt is chosen based upon the CFL condition given by Eq. (3.60). Provided that the ODE solver is at least second-order accurate in time, the splitting procedure given by Eq. (3.66) results in an approximation which is nominally second-order accurate in both space and time. We recognize that the splitting technique used here may result in the prediction of erroneous shock speeds due to the coupling of numerical diffusion and stiff source terms as demonstrated by Colella *et al.* [11] and LeVeque and Yee [32], though comparisons of numerically predicted shock wave speeds with exact values have shown good agreement for all cases considered in this work.

To account for phase interaction processes, the following autonomous system of five ordinary differential equations (ODEs), obtained by setting $\frac{\partial \mathbf{f}}{\partial x} = 0$ in Eq. (2.24) and reducing the resulting system, must be solved over the time interval $2\Delta t$ at each computational grid point,

$$\frac{d\mathbf{y}_s}{dt} = \mathbf{h}_s(\mathbf{y}_s), \tag{3.67}$$

where

$$\mathbf{y}_s = [\rho_2, \phi_2, u_2, e_2, I]^T,$$

$$\mathbf{h}_s(\mathbf{y}_s) = \left[\frac{\phi_1\phi_2}{\mu_c}(P_2 - P_1 - f) - \phi_2 C_m, -\frac{\rho_2\phi_1}{\mu_c}(P_2 - P_1 - f), -\frac{C_d}{\rho_2\phi_2}, -\frac{C_e}{\rho_2\phi_2}, C_I\right]^T.$$

The definitions for C_m, C_d, C_e, and C_I are given in Eq. (2.28). Algebraic expressions for ρ_1, ϕ_1, u_1, and e_1 in terms of $\mathbf{y}_s$ are obtained by respectively adding the gas and solid mass, momentum, and energy equations and integrating the resulting homogeneous ODEs,

$$\rho_1\phi_1 + \rho_2\phi_2 = [\rho_1\phi_1 + \rho_2\phi_2]_k^{n+1}, \tag{3.68}$$

$$\rho_1\phi_1 u_1 + \rho_2\phi_2 u_2 = [\rho_1\phi_1 u_1 + \rho_2\phi_2 u_2]_k^{n+1}, \tag{3.69}$$

$$\rho_1\phi_1\left(e_1 + \frac{u_1^2}{2}\right) + \rho_2\phi_2\left(e_2 + \frac{u_2^2}{2}\right) = \left[\rho_1\phi_1\left(e_1 + \frac{u_1^2}{2}\right) + \rho_2\phi_2\left(e_2 + \frac{u_2^2}{2}\right)\right]_k^{n+1}, \tag{3.70}$$

where the right-hand sides of these equations are integration constants obtained using the data $\mathbf{Q}_k^{n+1}$ provided by the preceding convection step in Eq. (3.66). Here, subscript k is

used to indicate that the integration constant depends upon the grid cell location x_k, and the notation superscript $n+1$ is used to indicate that the constant is based on the data at time t^{n+1}. The algebraic relations given by Eqs. (3.68)–(3.70), with the saturation condition $\phi_1 = 1 - \phi_2$, are sufficient to express the gas variables as algebraic functions of the desired solid variables. As these equations are nonlinear, they give multiple roots for the gas-phase variables corresponding to subsonic and supersonic solutions; thus, the proper root must be selectively chosen in a problem specific manner. Last, the homogeneous ODE for particle number density can be directly integrated to give

$$n = n_k^{n+1}; \tag{3.71}$$

thus, the particle number density is constant during the source step.

Equation (3.67) is in a form suitable to be numerically solved using standard ODE solvers. For this study, an implicit stiff solver contained in the software package LSODE (Livermore Solver for Ordinary Differential Equations) [27] was used to numerically integrate these equations. The solver uses a method based on backward differentiation formulas and internally generates a full Jacobian matrix (i.e., $\frac{\partial \mathbf{h}_s}{\partial \mathbf{y}_s}$) using finite differencing. The solver achieves high-order time accurate approximations by adapting the integration time step such that the truncation error of the scheme meets a user specified tolerance. For the computations performed in this study, an absolute tolerance of magnitude 1.0×10^{-9} was used for each component of $\mathbf{y}_s$.

4. NUMERICAL SIMULATIONS

Comparisons are given between numerical predictions and known solutions to three different test cases in order to demonstrate the numerical method. The test cases include: (1) an inert two-phase shock tube problem; (2) the evolution of an inert compaction wave in a granular material induced by a moving piston; and (3) the evolution of a two-phase detonation wave in an energetic granular material induced by a moving piston. The first case considers gas and solid convection only, whereas the second and third cases couple gas and solid convection with phase interaction processes. All computations were performed on an IBM RS 6000 Model 350 workstation.

4.1. *Inert Two-Phase Shock Tube Problem*

The shock tube problem provides a stringent test for numerical methods used to solve hyperbolic systems of conservation laws since it generally requires the resolution of both contact discontinuities and shocks. As previously discussed, the two-phase shock tube problem, also known as the Riemann problem, involves the break-up of a single initial discontinuity separating constant left (L) and right (R) states into self-similar waves consisting of a shock, a rarefaction, and a contact discontinuity in both the gas and the solid. As this problem considers convection only, $\mathbf{g}(\mathbf{q}) = 0$ in Eq. (2.24).

For this simulation, ideal equations of state were used for both the gas and the solid [$P_1 = \rho_1 R_1 T_1$, $e_1 = c_{v1} T_1$; $P_2 = \rho_2 R_2 T_2$, $e_2 = c_{v2} T_2$] so that the numerical predictions could be compared to existing closed-form analytical solutions. To this end, no jump in volume fraction was prescribed across the initial discontinuity; as such, volume fraction remains constant for all time, and the analytical solution for each phase is simply given by

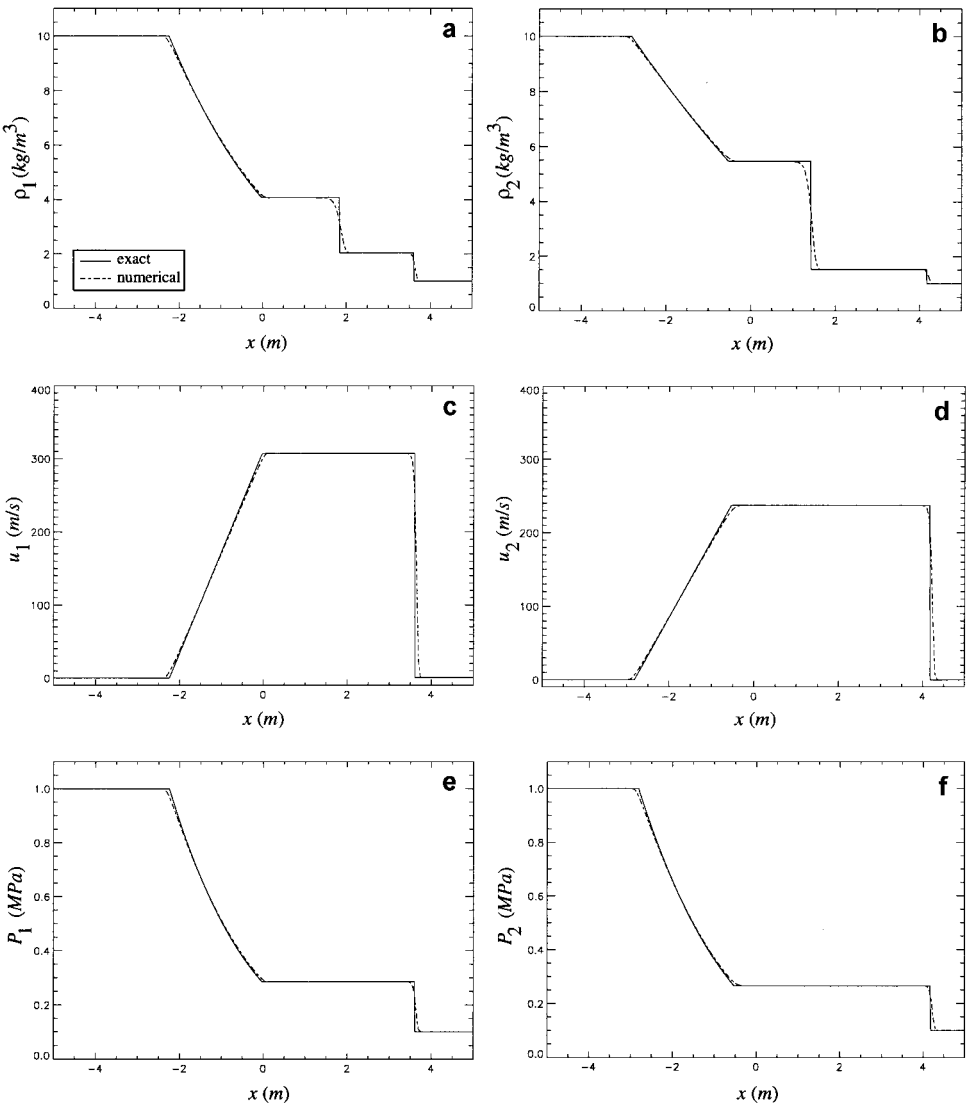

FIG. 3. Comparison of the predicted and exact solutions for the inert shock-tube problem at $t = 6$ ms: (a, b) gas and solid density, (c, d) gas and solid velocity, (e, f) gas and solid pressure, (g, h) gas and solid temperature, and (i) particle number density.

the classical solution to the shock tube problem for a single phase system [12]. For these equations of state, Eqs. (3.53)–(3.55) reduce to

$$\tilde{F}_{i_{\rho_i \phi_i}} = \frac{\gamma_i - 1}{2}(e_{iR} + e_{iL}),$$

$$\tilde{F}_{i_{\phi_i}} = 0,$$

$$\tilde{F}_{i_{e_i}} = \frac{\gamma_i - 1}{2}(\rho_{iR}\phi_{iR} + \rho_{iL}\phi_{iL}),$$

where γ_i $(i = 1, 2)$ is the specific heat ratio. Values chosen for model parameters and initial conditions are given in Table I. Different values for c_{v1} and c_{v2} were used so that differences in the gas and solid solutions exist. The computational domain used for this simulation

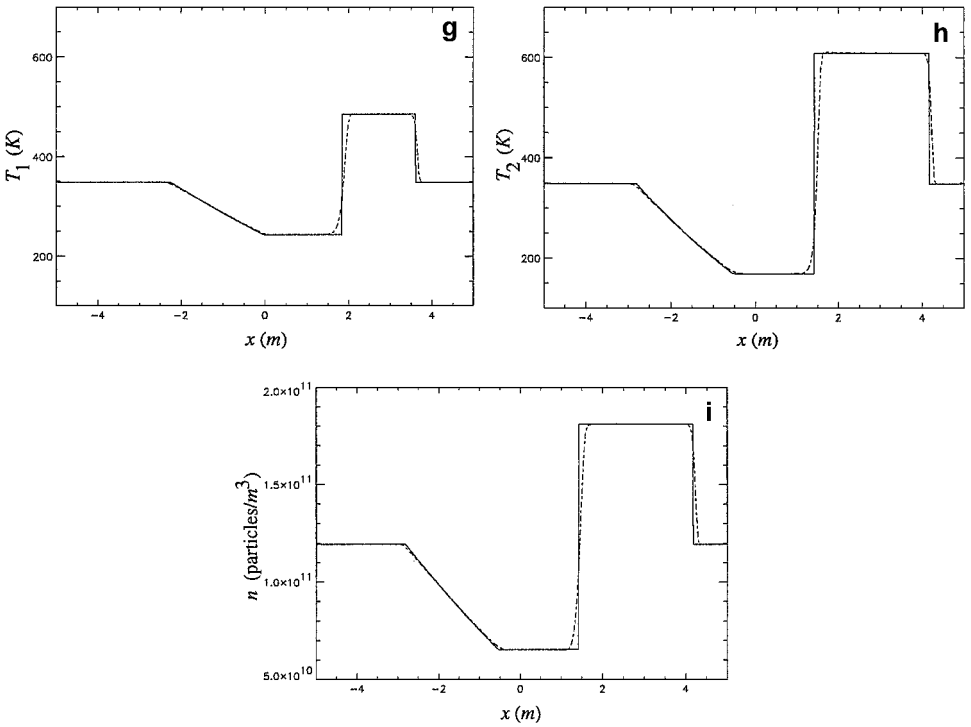

FIG. 3—*Continued*

($-5 \leq x \leq 5$ m) was discretized into $N = 200$ uniformly spaced nodes, with the initial discontinuity located at the center of the domain ($x = 0$ m). The computational run time for this simulation was approximately 2 min.

Shown in Fig. 3 is a comparison between the numerically predicted solution and the exact solution at $t = 6$ ms. For each phase the solution consists of a right-propagating shock

TABLE I
Parameter Values and Initial Conditions Used for the Shock-Tube Simulation

Parameter or initial condition	Value	Units
c_{v1}	7.18×10^2	J/(kg K)
c_{v2}	2.39×10^2	J/(kg K)
R_1	2.87×10^2	J/(kg K)
R_2	2.87×10^2	J/(kg K)
u_{1L}	0	m/s
u_{2L}	0	m/s
u_{1R}	0	m/s
u_{2R}	0	m/s
ρ_{1L}/ρ_{1R}	1.00×10^1	
ρ_{2L}/ρ_{2R}	1.00×10^1	
ϕ_{2L}/ϕ_{2R}	1.00×10^0	
P_{1L}/P_{1R}	1.00×10^1	
P_{2L}/P_{2R}	1.00×10^1	
n_L/n_R	1.00×10^0	

wave, followed by a slower right-propagating contact discontinuity and a left-propagating rarefaction. As a consequence of choosing $c_{v2} < c_{v1}$, the solid shock and rarefaction propagate faster than those of the gas, while the solid contact discontinuity propagates more slowly than that of the gas. The numerical predictions agree well with the exact solution; both the wave speeds and the magnitudes of the jumps are correctly predicted. Furthermore, the numerical method is able to capture the discontinuities without the generation of spurious oscillations. The shocks are spread over approximately three computational cells, while the contact discontinuities are spread over approximately seven cells. Typically, a larger number of cells are required by shock-capturing methods to capture discontinuities associated with linearly degenerate characteristic fields (i.e., contact discontinuities). This is due to the absence of a "steepening" mechanism for linearly degenerate fields, such as provided by the coalescence of acoustic waves in genuinely nonlinear acoustic fields [63]. Consequently, the numerically predicted spatial profiles for contact discontinuities do not steepen as time evolves.

To investigate the convergence rate of the numerical method, which provides a measure of its spatial accuracy, it is necessary to define the error associated with the numerical predictions. For the test cases given in this paper, the error E at t^n is based on either the gas or the solid pressure ($i = 1, 2$) and is defined by the 1 norm

$$E(t^n) = \frac{1}{N} \sum_{k=1}^{N} \frac{|P_{i_k}(t^n) - P_i(x_k, t^n)|}{P_i^c}, \tag{4.1}$$

where $P_{i_k}(t^n)$ is the numerically predicted pressure at the nodal location x_k, $P_i(x_k, t^n)$ is the pressure given by the exact solution at this same location, P_i^c is a characteristic pressure used to nondimensionalize the error, and N is the total number of computational cells. This error is the fractional error used by Woodward and Colella [64] and by Grismer [24] to demonstrate the convergence properties of similar high-resolution numerical methods for the Euler equations. The convergence rate of the method is defined as the change in this error with respect to a change in grid resolution and is estimated by the slope p of the best fit line through the data points $(E, 1/N)$ plotted in the $\log(1/N)$-$\log E$ plane.

Convergence data obtained for the inert shock tube problem are plotted in Fig. 4. For simplicity, it was assumed that $R_1 = R_2 = 287$ J/(kg K) and $c_{v1} = c_{v2} = 717.5$ J/(kg K) for this convergence study. Consequently, identical solutions are obtained for the gas and solid, both of which are given by the gas-phase solution shown in Fig. 3. The data were obtained using computational grids for which N was within the range $1000 \leq N \leq 15000$. The characteristic pressure used to nondimensionalize the error was $P_1^c = P_2^c = 0.1$ MPa, the pressure associated with the state to the left of the initial discontinuity. Results of this study show the convergence rate to be $p = 1.003$. The convergence rates reported in Refs. [24, 64], based on the exact solution of the inert shock tube problem for an ideal gas, were also near unity. Though these high-resolution shock-capturing methods have higher spatial accuracy than nominally first-order methods (i.e., the Lax–Friedrichs scheme, Godunov's method), the accuracy is less than second-order. This result is expected since these methods reduce to nominally first-order accuracy near discontinuities due to the flux-limiting procedure. For the range of nodal points used in this study, machine round-off error was insignificant.

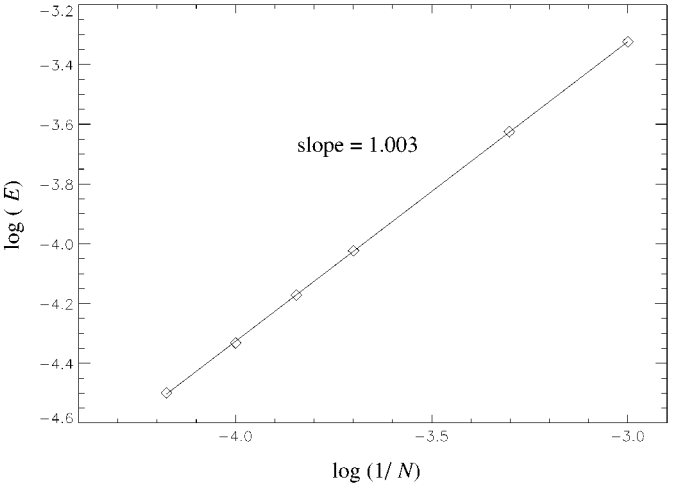

FIG. 4. Numerical convergence data for the inert shock tube problem based on the 1 norm for the pressure.

4.2. *Inert Compaction Wave Problem*

This simulation involves the evolution of an inert compaction wave due to compression of the granular material by a moving piston. A compaction wave refers to the propagation of a finite disturbance in volume fraction due to a local mechanical stress imbalance [i.e., $P_2 - P_1 - f \neq 0$ in Eq. (2.7)]. Here, the processes of gas and solid convection are coupled with the processes of interphase drag, interphase heat transfer, and material compaction. It is not the intent of this section to give a detailed compaction wave analysis; rather, results that illustrate the evolution of a compaction wave are given, and a comparison between the numerically predicted compaction wave structure and the steady structure predicted by the analysis of Powers *et al.* [43] is given. Also, convergence results are given in order to further validate the numerical method. The reader is referred to Refs. [2, 43, 52] for a thorough discussion of compaction waves in energetic granular materials.

As this simulation involves the evolution of a compaction wave resulting from piston impact, the model equations valid in a fixed laboratory reference frame (x, t), as presented in this paper, were transformed to a piston-attached reference frame (ξ, t) for convenience. The transformation, as illustrated in Fig. 5, is given by $\xi = x - x_p(t)$ and $v_i = u_i - u_p(t)$

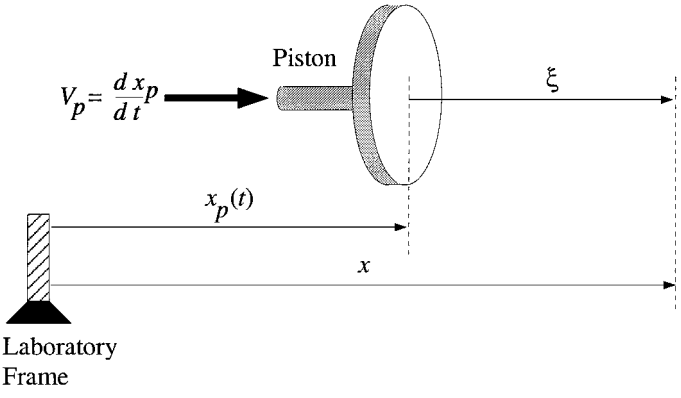

FIG. 5. Schematic of the piston-attached coordinate system.

$(i = 1, 2)$, where v_i is velocity in the piston-attached frame, and $x_p(t)$ and $u_p(t)$ are the piston position and the prescribed piston velocity in the laboratory frame, respectively. The piston is continuously accelerated from rest to a constant velocity of 100 m/s in 2 μs; the piston velocity is given by

$$u_p(t) = \begin{cases} (100\ \text{m/s}) \sin\left[\frac{\pi}{2}\left(\frac{t}{2\ \mu\text{s}}\right)\right] & \text{for } 0 < t \le 2\ \mu\text{s} \\ 100\ \text{m/s} & \text{for } t > 2\ \mu\text{s}. \end{cases} \tag{4.2}$$

This rapid acceleration is chosen so that the piston attains its maximum velocity over a time interval which is short relative to the time required for the piston-induced compaction wave to become fully developed. A maximum piston velocity of 100 m/s is chosen since much of the experimental and numerical compaction and DDT data reported in the literature have been obtained for piston velocities close to this value [5, 9, 59–61]. Since the piston-attached frame is noninertial, piston acceleration terms must be included in the momentum and total energy equations for the gas and solid [Eqs. (2.2), (2.3), (2.5), and (2.6)]. These terms are treated as time-dependent source terms which slightly modify Eq. (3.67), resulting in a nonautonomous system; details of the modification are given in Ref. [22].

For this simulation, equations of state representative of the high-explosive HMX (cyclotetramethylene tetranitramine) are adopted [45]. A virial equation of state was used for the gas [$P_1 = \rho_1 R_1 T_1(1 - b\rho_1)$, $e_1 = c_{v1} T_1$, where b is the constant virial coefficient] and a nonideal Tait equation of state was used for the solid [$P_2 = (\gamma_2 - 1)c_{v2}\rho_2 T_2 - \rho_{2o}\sigma/\gamma_2$, $e_2 = c_{v2} T_2 + \rho_{2o}\sigma/(\gamma_2\rho_2) + q$, where γ_2 is the Tait parameter, σ is the nonideal solid parameter, and q is the mass specific chemical energy]. For these equations of state, Eqs. (3.53)–(3.55) reduce to the following expressions for the gas and solid, respectively:

$$\tilde{F}_{1_{\rho_1\phi_1}} = \frac{R_1}{c_{v1}}\left(1 + 2b\frac{\phi_{1L} + \phi_{1R}}{\phi_{1L}\phi_{1R}}\frac{\rho_{1L}\phi_{1L} + \rho_{1R}\phi_{1R}}{2}\right)\left(\frac{e_{1L} + e_{1R}}{2}\right),$$

$$\tilde{F}_{1_{\phi_1}} = -\frac{1}{2}\frac{R_1 b}{c_{v1}}\left[\frac{(\rho_{1L}\phi_{1L})^2}{\phi_{1L}\phi_{1R}}e_{1L} + \frac{(\rho_{1R}\phi_{1R})^2}{\phi_{1L}\phi_{1R}}e_{1R}\right],$$

$$\tilde{F}_{1_{e_1}} = \frac{R_1}{c_{v1}}\left[\frac{\rho_{1L}\phi_{1L} + \rho_{1R}\phi_{1R}}{2} + b\frac{\phi_{1L} + \phi_{1R}}{\phi_{1L}\phi_{1R}}\left(\frac{(\rho_{1L}\phi_{1L})^2 + (\rho_{1R}\phi_{1R})^2}{4}\right)\right],$$

$$\tilde{F}_{2_{\rho_2\phi_2}} = (\gamma_2 - 1)\left(\frac{e_{2L} + e_{2R}}{2} - q\right),$$

$$\tilde{F}_{2_{\phi_2}} = -\rho_{2o}\sigma,$$

$$\tilde{F}_{2_{e_2}} = (\gamma_2 - 1)\left(\frac{\rho_{2L}\phi_{2L} + \rho_{2R}\phi_{2R}}{2}\right).$$

The time-dependent boundary conditions that must be satisfied at the piston surface are easily obtained by requiring the velocity of both the gas and the solid, measured relative to the piston, to vanish at this boundary [$v_1(0, t) = v_2(0, t) = 0$]. This requirement is equivalent to enforcing a zero mass flux condition at the piston surface. Time is restricted such that there is insufficient time for waves generated by the moving piston to reach the upstream boundary; thus, no condition is enforced at this boundary. The computational domain ($0 \le \xi \le 1.2$ m), which consisted of $N = 600$ nodes, was initialized with the ambient conditions given in

TABLE II
Parameter Values and Ambient Conditions Used for the Compaction Wave and DDT Simulations

Parameter or ambient condition	Compaction value	DDT value	Units	Ref.
b	7.60×10^{-4}	7.60×10^{-4}	m^3/kg	
R_1	8.50×10^{2}	8.50×10^{2}	J/(kg K)	[45]
c_{v1}	2.40×10^{3}	2.40×10^{3}	J/(kg K)	[3, 45]
c_{v2}	1.50×10^{3}	1.50×10^{3}	J/(kg K)	[3, 8, 45]
σ	8.98×10^{6}	8.98×10^{6}	m^2/s^2	[43, 45]
q	0	5.84×10^{6}	J/kg	[8, 45]
k_I	—	1.00×10^{6}	s^{-1}	
T_I	—	2.69×10^{3}	K	
I_{ig}	—	5.00×10^{-1}		
a	—	2.90×10^{-9}	m/(Pa s)	[8, 45]
h	1.00×10^{7}	1.00×10^{7}	J/(K s $m^{8/3}$)	[45]
β	1.00×10^{4}	1.00×10^{4}	kg/(s m^2)	[45]
μ_c	1.00×10^{3}	1.00×10^{2}	kg/(s m)	[45]
m	—	1.00×10^{0}		[8, 45]
γ_2	5.00×10^{0}	5.00×10^{0}		[43, 45]
r_o	1.00×10^{-4}	1.00×10^{-4}	m	[5, 8, 45]
T_o	3.00×10^{2}	3.00×10^{2}	K	
ρ_{1o}	1.00×10^{1}	1.00×10^{1}	kg/m^3	[45]
ρ_{2o}	1.90×10^{3}	1.71×10^{3}	kg/m^3	[61]
ϕ_{2o}	7.30×10^{-1}	7.00×10^{-1}		[61]

Table II. Values for the model parameters are also given in this table. The computational run time for this simulation was approximately 45 min.

Figure 6 shows the numerically predicted history for the gas and solid velocity (measured relative to a fixed laboratory frame), the gas and solid pressure, the solid volume fraction, and the particle number density. Here, ξ is position measured relative to the piston surface. A smooth but rapid increase is predicted in all variables in response to the sudden acceleration of the piston. A dispersed compaction wave quickly develops and propagates away from the piston with a uniform speed of 418.3 m/s, which is well below the ambient solid sound speed ($\sim$3000 m/s). A solid shock does not form in response to the accelerating piston due to the rapid relaxation in solid pressure associated with material compaction (i.e., $P_2 \rightarrow P_1 + f$). The predicted time and length required for transition to a fully developed compaction wave are approximately 0.1 ms and 10 cm (measured relative to the piston). The solid volume fraction and pressure in the compacted region are predicted to be 0.96 and 67.1 MPa, respectively. These values for the compaction wave speed, the final volume fraction, and the final solid pressure agree well with the experimentally determined values reported by Sandusky and Liddiard [52] for the impact of a 100 m/s piston with a bed of porous HMX ($\phi_{2o} = 0.73$). Sandusky and Liddiard observed compaction wave speeds of 432 m/s, final solid volume fractions near 0.94, and final solid pressures near 50 MPa; no values for transition length and time were reported.

Figure 7 shows the numerically predicted variation in solid density, velocity, pressure, and volume fraction within the compaction zone at $t = 3.2$ ms. Also shown in this figure are predictions for the steady wave structure given by the simplified analysis of Powers

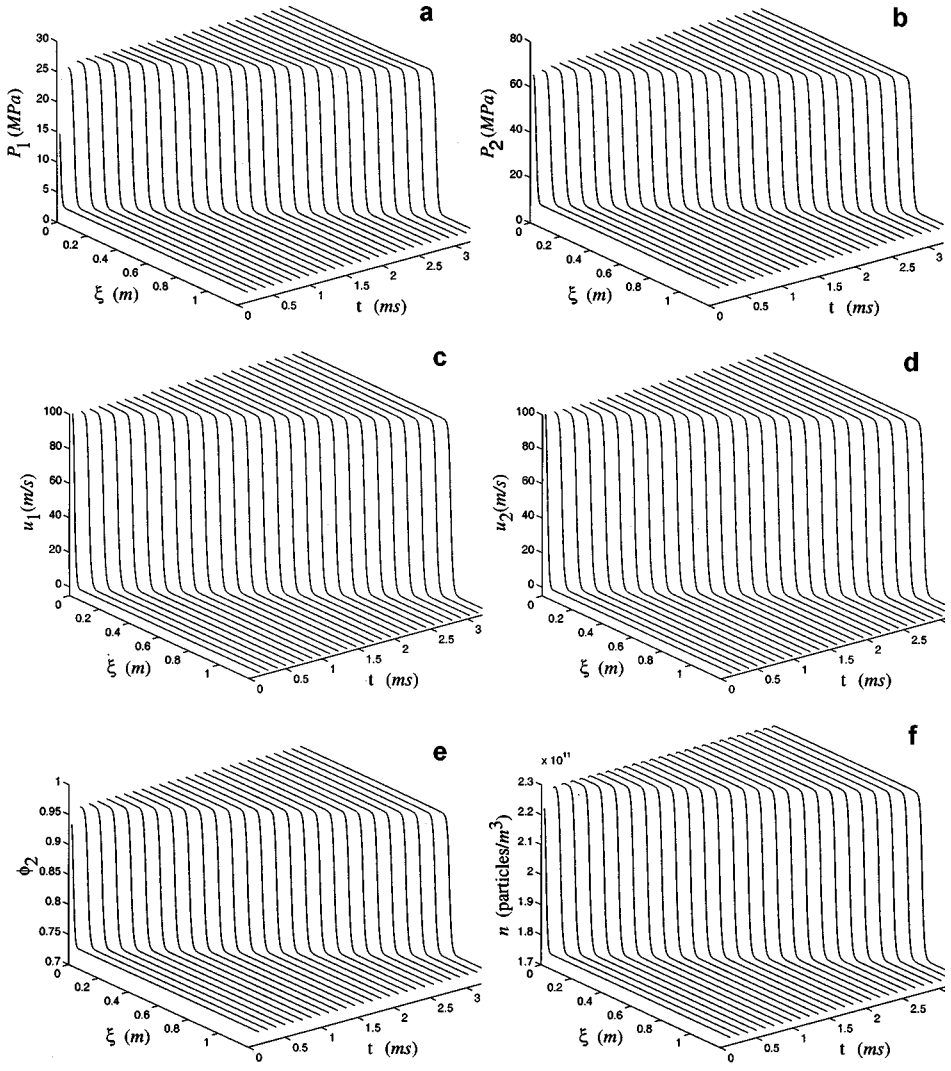

FIG. 6. Predicted time histories for the inert compaction wave problem: (a, b) gas and solid pressure, (c, d) gas and solid velocity, (e) solid volume fraction, and (f) particle number density.

et al. [43]. In their analysis, Powers *et al.* ignore gas effects and describe steady compaction wave structure in terms of the solid variables. The flow located between the piston ($\xi = 0$ m) and the trailing edge of the compaction wave ($\xi = 0.82$ m) is not shown in this figure. The prediction labeled Numerical 1 is the solution shown in Fig. 6. The prediction labeled Numerical 2, also shown at $t = 3.2$ ms, was obtained by ignoring interphase drag and heat transfer and by ignoring gas effects in Eq. (2.7). As such, a direct comparison can be made between the numerical and analytical predictions for compaction wave structure. Good agreement exists between the Numerical 2 prediction and the analytical prediction. It is noted that a continuous compaction wave structure is predicted and that interphase drag, interphase heat transfer, and gas effects increase the final solid pressure and decrease the final solid volume fraction. The results shown here indicate that the gas has little influence on compaction wave structure. The wave speed predicted by the simulation denoted as Numerical 2 is 405.8 m/s; this agrees well with the value of 404.7 m/s predicted by the

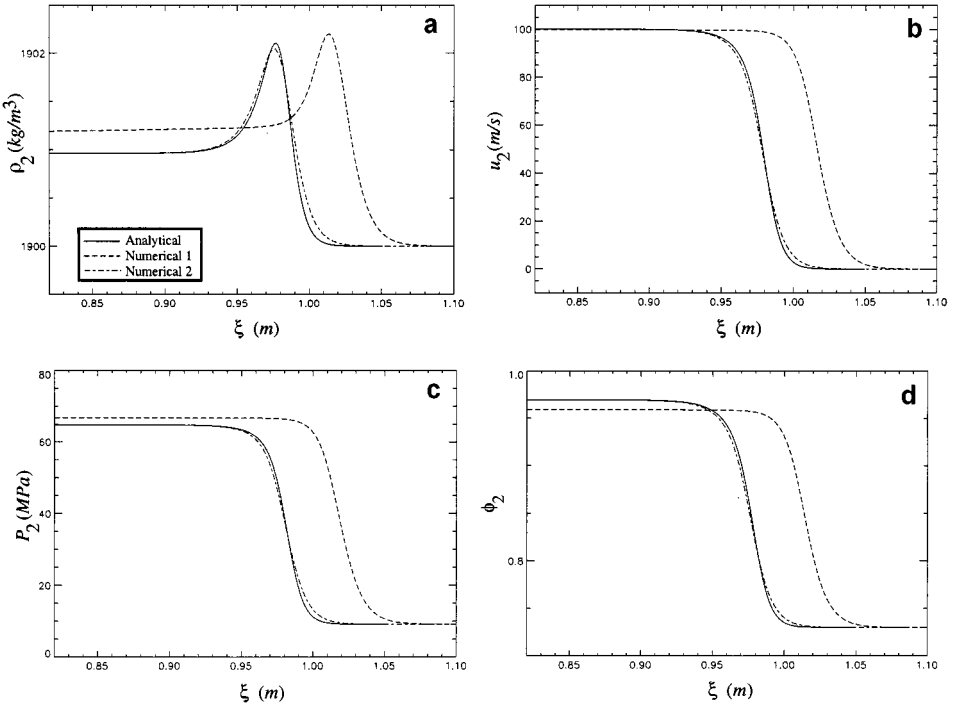

FIG. 7. Comparison of the predicted and analytical solutions for the inert compaction wave structure: (a) solid density, (b) solid velocity, (c) solid pressure, and (d) solid volume fraction.

steady analysis of Powers *et al*. The compaction wave trajectories for the simulations denoted as Numerical 1 and Numerical 2 are shown in Fig. 8.

Convergence data obtained for this test case based on a comparison of the Numerical 2 prediction with the analytical compaction wave structure are plotted in Fig. 9. Here, the error is based on the definition in Eq. (4.1), where $P_2^c = 8.21$ MPa is the ambient pressure of the

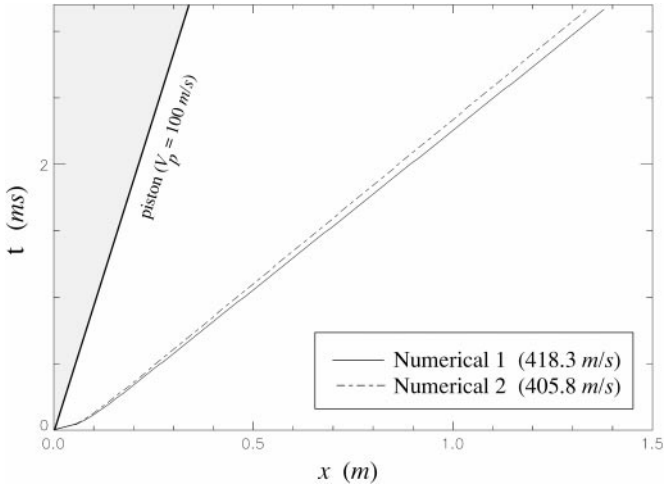

FIG. 8. Predicted compaction wave trajectories for the inert compaction wave problem.

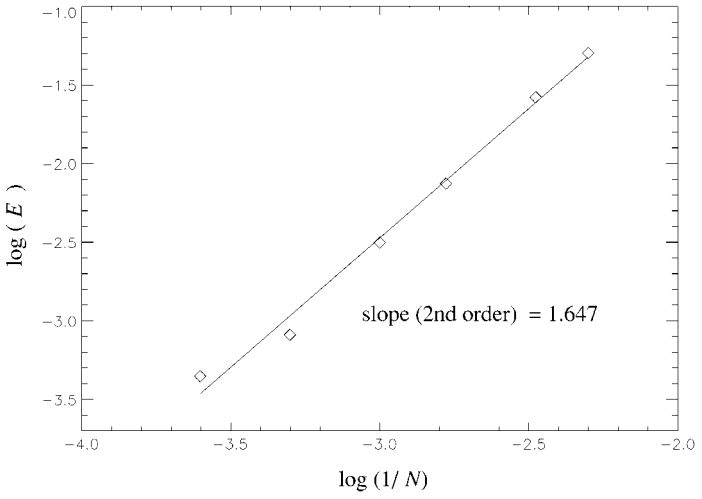

FIG. 9. Numerical convergence data for the inert compaction wave problem based on the 1 norm for the solid pressure.

solid. The scatter in the data from the linear curve fit is greater than that in the convergence data obtained for the inert shock tube problem. This increased scatter is likely due to inaccuracies in the placement of the exact solution relative to the numerically predicted solution in computing the error. As such, the exact solution was placed at the location which minimized the computed error. These inaccuracies do not exist for the shock tube simulation since the exact time-dependent solution is known. Since the compaction wave structure is continuous, this test case provides a good measure for determining the spatial accuracy of the method for a continuous solution. The computed convergence rate is $p = 1.647$. Though this rate is substantially higher than the rate computed for the test case having discontinuous solutions, it is lower than what would be expected from a truly second-order method. This result is likely due to numerical diffusion introduced by the flux-limiting procedure. It is possible that the convergence rate might improve for more resolved computational grids than used here. However, it is not feasible to investigate this claim since the most resolved case performed as part of this study ($N = 4000$) required nearly 100 h of CPU time.

4.3. *Two-Phase Detonation Problem*

This simulation involves the evolution of a self-propagating, two-phase detonation wave due to compression of the granular material by a moving piston. Here, the processes of gas and solid convection are coupled with the local processes of combustion, interphase drag, interphase heat transfer, and material compaction. The results given illustrate the evolution of a detonation wave, and the numerically predicted detonation wave structure and the structure predicted by a steady-state analysis are compared [22]. The reader is referred to Refs. [3, 8, 44, 45] for a discussion of two-phase detonation waves in energetic granular materials.

As was done for the inert compaction wave problem, we numerically solve the model equations in the piston-attached frame where the piston velocity is given by Eq. (4.2). Additionally, the same equations of state and boundary conditions used for the compaction wave problem are used here; as such, this problem simulates DDT in granular HMX. Model

parameters and initial conditions used for this simulation are given in Table II. While most of these values are consistent with experimental data for HMX, the value of the drag parameter β is an order of magnitude smaller than suggested by gas permeation experiments [1]. Also, the initial gas density ρ_{10} is approximately an order of magnitude larger than typically found in DDT experiments. These values were largely chosen to facilitate comparisons with the work of Powers *et al.* [45], as well as to illustrate the evolution of a new two-phase weak detonation structure. Even so, many experimentally observed features are correctly predicted. The computational domain ($0 \leq \xi \leq 50$ cm) consisted of $N = 1500$ uniformly spaced nodes. The CPU time for this simulation was approximately 6 h.

Shown in Fig. 10 are the predicted velocity (measured relative to the laboratory frame), pressure, and temperature history of the gas. Also shown in this figure are the spatial profiles at $t = 210$ μs. The predicted solid velocity, pressure, and temperature history are shown in Fig. 11. Each of the curves for the solid variables is plotted up to the point of complete combustion ($\phi_{2\epsilon} = 1 \times 10^{-5}$). In these figures, ξ is position measured relative to the piston surface.

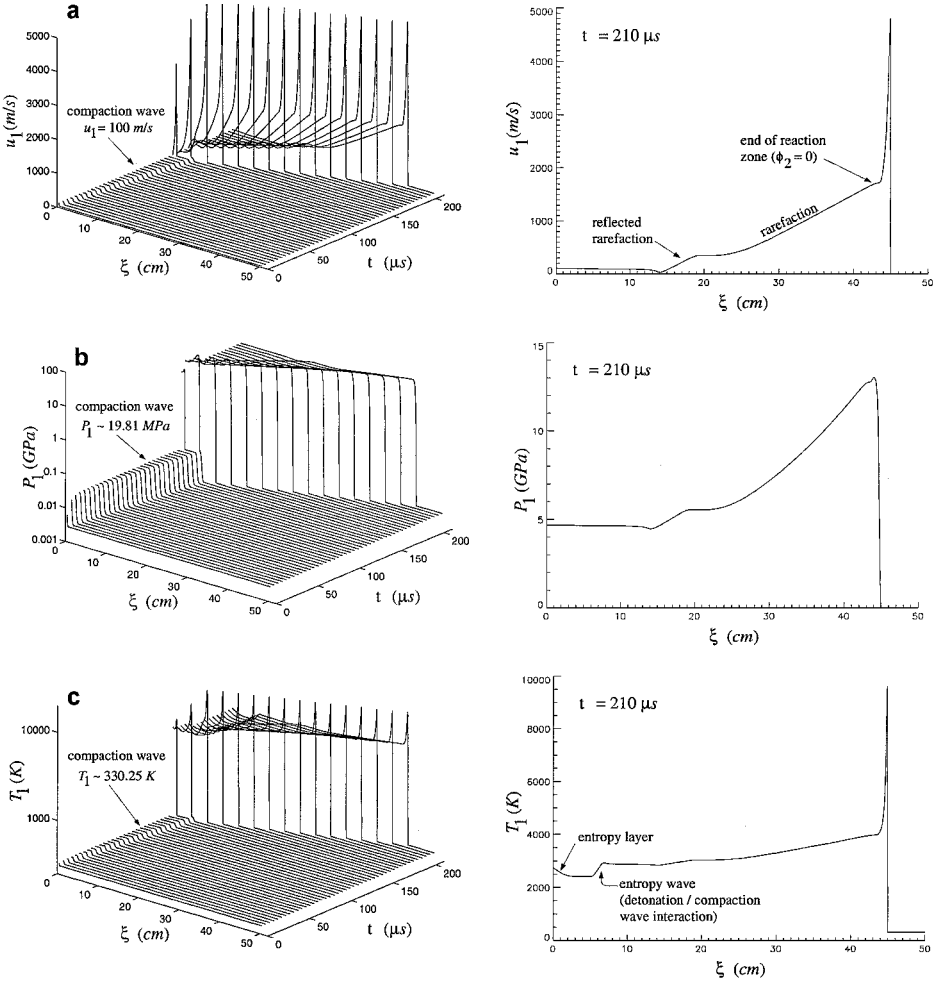

FIG. 10. Predicted time histories for the *shocked gas–unshocked solid* weak detonation simulation: (a) gas velocity, (b) gas pressure, and (c) gas temperature.

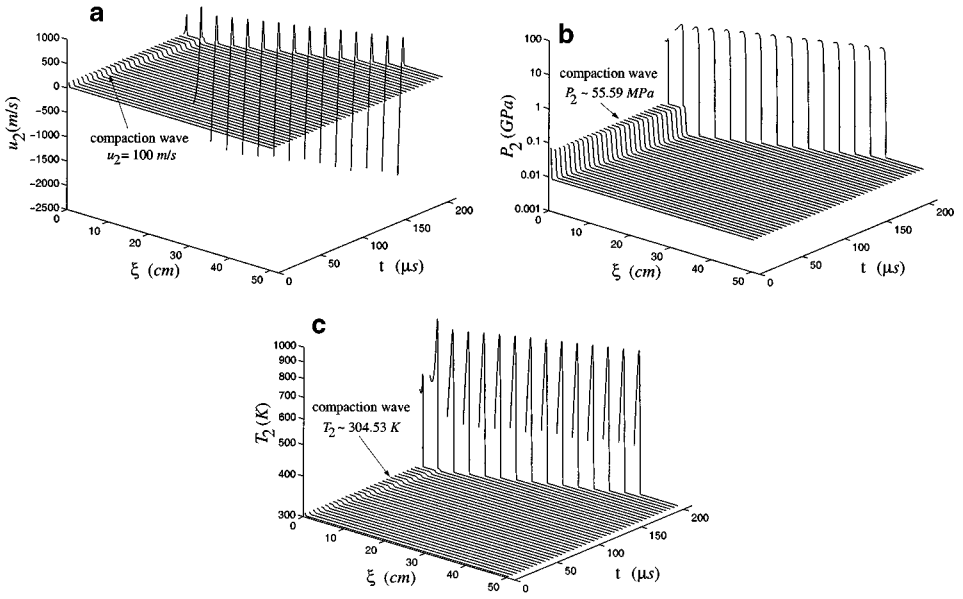

FIG. 11. Predicted time histories for the *shocked gas–unshocked solid* weak detonation simulation: (a) solid velocity, (b) solid pressure, and (c) solid temperature.

A dispersed compaction wave quickly forms and propagates away from the piston at constant speed; the predicted wave speed relative to the fixed laboratory frame is 401.98 m/s. The predicted compaction zone thickness is approximately 5.0 mm. A continuous variation in all variables is predicted within the compaction zone. The gas pressure and temperature increase from their ambient values of 2.57 MPa and 300 K to approximately 19.81 MPa and 330.25 K, and the solid pressure and temperature increase from their ambient values of 8.21 MPa and 300 K to approximately 55.59 MPa and 304.53 K, respectively. The gas and solid velocity increase from 0 to 100 m/s, as required by the zero mass flux boundary condition at the piston surface.

As time advances, the width of the compacted region increases as the compaction wave propagates away from the piston. Combustion initiation is predicted to occur at the piston surface after an induction period of approximately 135 μs. Induction periods prior to the onset of sustained combustion are characteristic of piston-initiated DDT in granular high explosives [5, 36, 37]. It is widely accepted that during the induction period, weakly exothermic chemical reactions take place due to localized heating of the explosive material as it is compacted. Possible heating mechanisms include adiabatic shear localization within particles, friction between particles, and adiabatic compression of the gas contained within the interstices of particles, the analysis of which is beyond the scope of this work. See Gonthier *et al.* [23] for the modeling and analysis of compaction-induced heating in granular HMX. As progressively more energy is liberated due to combustion, the reaction rate increases, resulting in a self-accelerating process. Since chemical reaction is local in nature, the compacted explosive nearest the piston surface incubates the longest and, consequently, is first to undergo sustained combustion. The onset of sustained combustion marks the end of the induction period.

As seen in Figs. 10 and 11, a rapid increase in the velocity, pressure, and temperature of both the gas and solid is predicted following the onset of combustion. Transition to

detonation is predicted to occur almost immediately. The detonation continuously accelerates and strengthens as it propagates through the compacted material. The solid is first completely consumed at the piston surface approximately 140 μs after piston impact; consequently, the solid is not directly affected by the moving piston for $t \geq 140$ μs. The accelerating detonation overtakes the compaction wave approximately 145 μs after piston impact. Since the gas and solid pressure, gas and solid temperature, and solid volume fraction continuously decrease immediately in front of the detonation as it traverses the compaction zone structure, both a left-propagating rarefaction and a right-propagating entropy wave are produced by the interaction. For this case, the entropy wave has a continuous structure (i.e., it is not a contact discontinuity). Subsequently, the left-propagating rarefaction reflects off the piston, the entropy wave continues to propagate slowly to the right, and the accelerating detonation relaxes to a steady detonation propagating at speed 6168 m/s. Following the detonation is a right-propagating rarefaction which reduces the gas velocity at the end of the reaction zone to that of the piston (100 m/s). The rarefactions are indicated in the spatial profiles for the gas velocity and pressure at $t = 210$ μs (Figs. 10a and 10b), and the entropy wave is indicated in the spatial profile for the gas temperature at $t = 210$ μs (Fig. 10c). Because the gas velocity (measured relative to the piston) is zero through the entropy wave at $t = 210$ μs, and because thermal diffusion is absent from the model, the wave does not move relative to the piston, nor does its amplitude decrease as time advances.

Also indicated in the gas temperature profile of Fig. 10c is an entropy layer immediately next to the piston surface which is generated during the transition process. Menikoff [38, 39] and Menikoff and Lackner [40] have shown that shock-capturing methods predict a spurious entropy layer when a shock interacts with a solid boundary and have proposed a production mechanism for this anomalous structure which is a direct consequence of the artificial width of the numerically predicted shock. For hyperbolic equations, the time interval associated with the shock–boundary interaction is zero since the shock is a discontinuity. However,

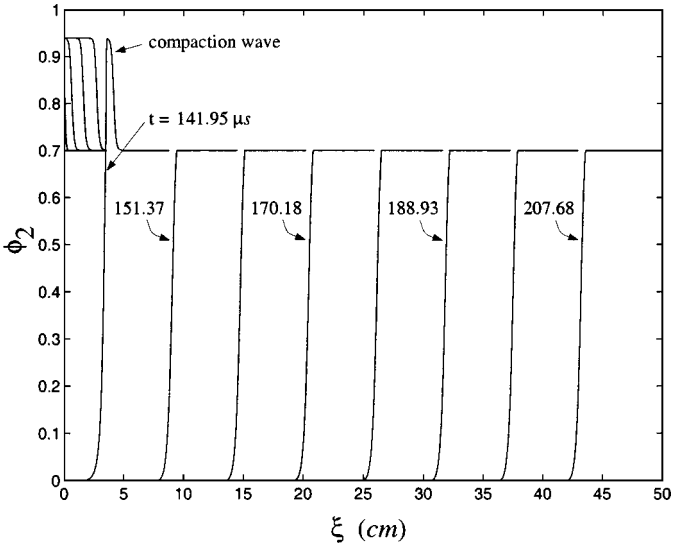

FIG. 12. Numerically predicted solid volume fraction history for the *shocked gas–unshocked solid* weak detonation simulation.

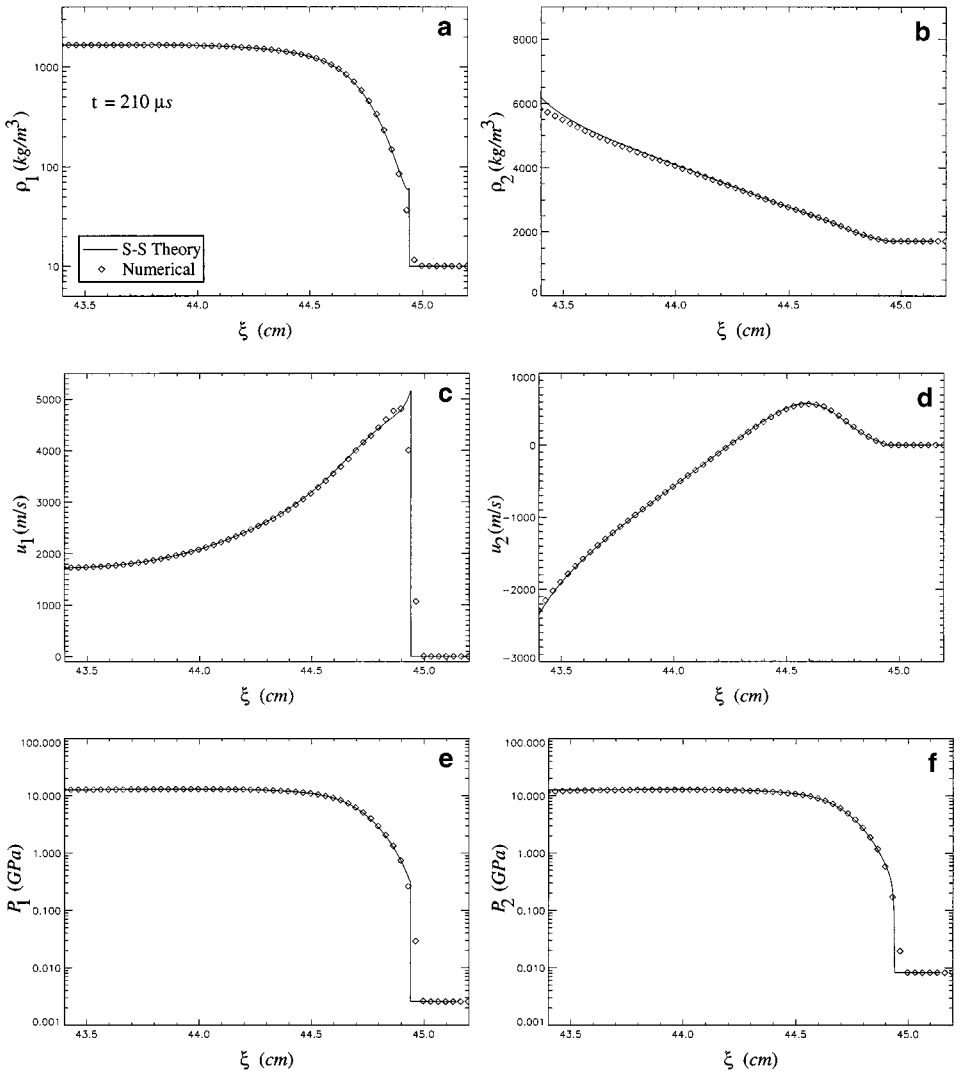

FIG. 13. Comparison of the *shocked gas–unshocked solid* weak detonation structures predicted by the steady and unsteady detonation analyses: (a, b) gas and solid density, (c, d) gas and solid velocity, (e, f) gas and solid pressure, (g, h) gas and solid temperature, (i, j) gas and solid Mach number squared (relative to the wave), (k) solid volume fraction, and (l) particle radius.

numerical shocks, having an artificial width due to numerical diffusion, interact with the boundary over a finite time interval. Since entropy production occurs only during the interaction period, the predicted width of the spurious entropy layer is close to the artificial shock width. Though not shown here, spurious entropy layers were also numerically predicted near the piston surface when the piston was impulsively set into constant velocity motion. Glaister [18] has also predicted spurious entropy layers for similar types of problems. Since the piston was continuously accelerated from rest to a constant velocity, the effects of the spurious entropy production mechanism may be minimal. Furthermore, the width of the entropy layer predicted here is much larger than the length of three computational cells, the typical length needed to numerically capture shocks. Nevertheless, it is difficult to

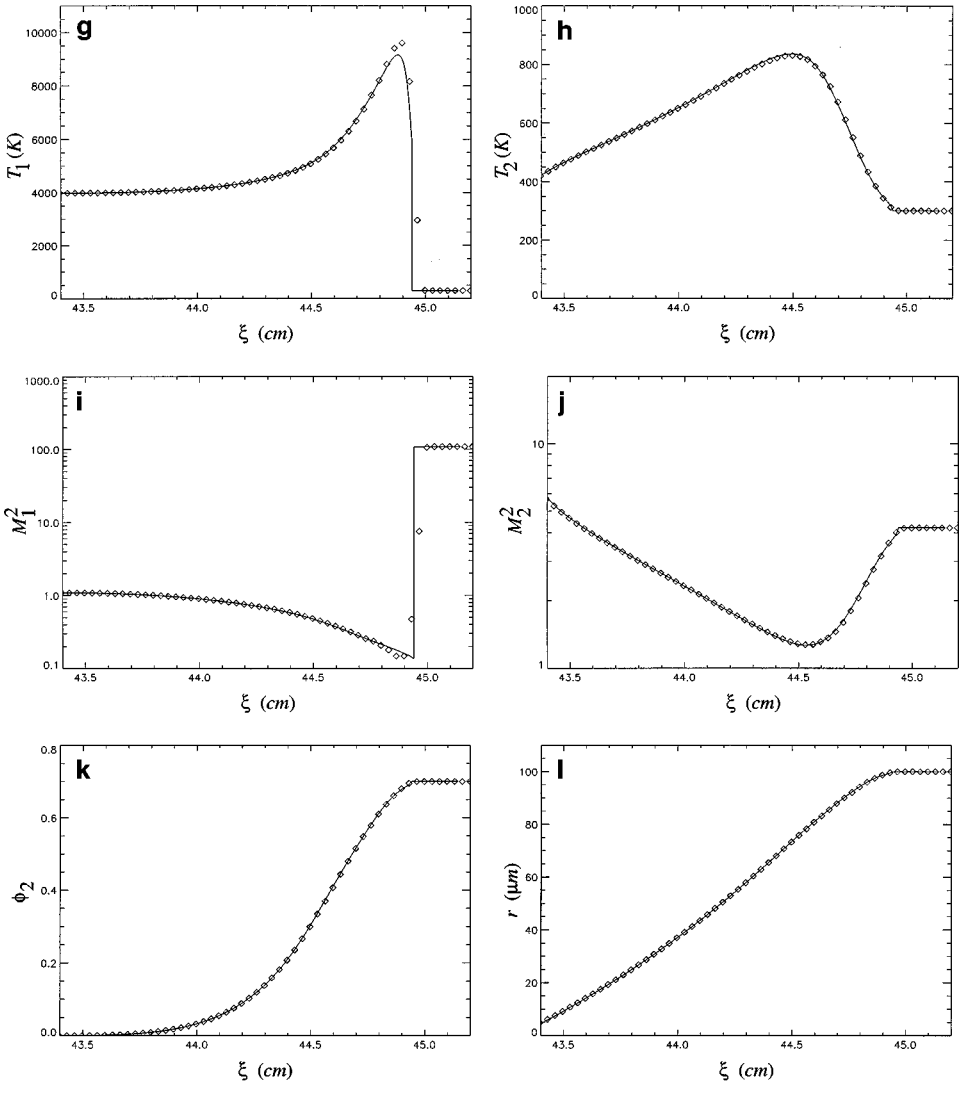

FIG. 13—*Continued*

conclusively determine if this entropy layer is physical or if it is a numerical artifact of the shock-capturing method.

The predicted solid volume fraction history is shown in Fig. 12. Here, the inert compaction wave is seen propagating away from the piston for early time. Across this wave, the ambient mixture is compacted from a solid volume fraction of 0.70 to 0.94. Following combustion initiation at the piston surface at $t = 135\ \mu$s, combustion consumes the solid as the resulting detonation propagates through the compacted material. As seen in this figure, the detonation is about to overtake the compaction wave at $t = 141.95\ \mu$s. Soon afterward, the steady detonation forms. The solid volume fraction continuously decreases from 0.70 to $\phi_{2\epsilon} = 1 \times 10^{-5}$ through the steady detonation structure.

The model reasonably predicts many experimentally observed features. Given in Table III are comparisons of numerically predicted and experimentally measured quantities for the

TABLE III
Comparison of Numerically Predicted Quantities with the Results of the DDT Experiment Given in Ref. [36]

Quantity	Experiment	Model
Compaction wave speed	400 m/s	401.98 m/s
Compaction wave thickness	2 mm	5 mm
Solid volume fraction behind the lead compaction wave	0.90	0.94
Time to detonation	142 μs	138 μs
Distance to detonation measured relative to the piston	25 mm	10 mm
Detonation wave speed	6200 m/s	6169.4 m/s

DDT of granular HMX [36]. However, experiments indicate a more complex transition process than predicted here involving the propagation of a low-speed combustion front away from the piston following initiation ($\sim$400 m/s), the subsequent formation of an inert solid plug slightly ahead of the combustion front, followed by the formation of a shock immediately ahead of the plug which induces a prompt transition to detonation. Son *et al.* [59, 60] have modified the conventional two-phase DDT model of Baer and Nunziato [3] to better account for the transition process including plug formation. Similar modifications, which only involve the forcing terms of the governing differential equations, can be made to the present model, and the high-resolution numerical method outlined in this paper can be applied without difficulty.

A comparison of the numerically predicted detonation structure with the structure predicted by a steady analysis is given in Fig. 13; details of the steady analysis are given in Ref. [12]. This figure shows the variation in density, velocity, pressure, temperature, and Mach number squared (measured relative to the wave) of the gas and solid and in the solid volume fraction and particle radius within the reaction zone. The flow located between the piston surface ($\xi = 0$ cm) and the end of the reaction zone ($\xi = 43.4$ cm) is not shown in this figure. Good agreement exists between the predicted solutions. As such, it is clear that a *shocked gas–unshocked solid* detonation structure has evolved. Moreover, since the Mach number of the gas at the end of the reaction zone is greater than unity ($M_1^2 = 1.094$), this structure is classified as a two-phase *weak detonation*; such structures have not been previously predicted. The numerical method is able to capture the gas shock with approximately three computational cells without the generation of spurious oscillations. Though not very evident here, the numerical method has difficulty accurately predicting the variation in solid quantities near the end of the reaction zone; this difficulty is slightly noticeable in the numerically predicted solid density profile. Reasons for this difficulty are unclear, but it is possibly a consequence of the burn termination technique used in this work.

Convergence data based on a comparison of the unsteady numerical prediction for the weak detonation structure with the result given by the steady analysis are plotted in Fig. 14. Here, the error is based on the definition in Eq. (4.1), where $P_1^c = 12.75$ GPa is the weak detonation gas pressure at the end of the reaction zone. As with the compaction wave test case, the steady-state solution was placed at the location which minimized the computed error. As indicated by lines I and II in the figure, the convergence rate of the numerical method for this problem depends on grid resolution. For relatively coarse grids ($400 \leq N \leq 2000$),

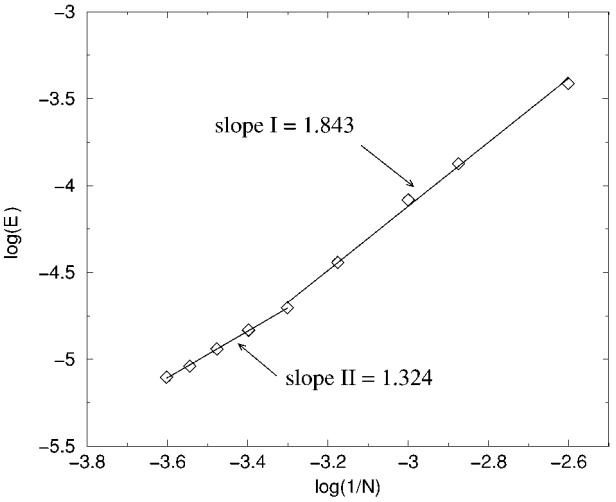

FIG. 14. Numerical convergence data for the two-phase detonation problem based on the 1 norm for the gas pressure.

the computed convergence rate is $p = 1.843$, which is substantially higher than typical rates for problems having discontinuous solutions ($\sim$1.0). In this case, the convergence rate is dominated by the integrated numerical error over the continuous reaction zone structure ($\sim$1 GPa) rather than by diffusive errors associated with the lead shock ($\sim$0.01 GPa). As the computational grid is refined ($2000 \leq N \leq 4000$), the convergence rate is observed to decrease to $p = 1.324$ as diffusion at the shock becomes increasingly important. If the grid were further refined ($N > 4000$), it is plausible that the convergence rate would approach unity as expected, but it is impractical to completely address this issue due to computational constraints. The most resolved case performed in this study ($N = 4000$) required nearly 24 h of CPU time. Fully resolved simulations would take considerably longer to compute.

5. CONCLUSIONS

A high-resolution, upwind numerical method was formulated for the accurate solution of a two-phase DDT model which is representative of a class of models used in current practice. The numerical method is a substantial improvement over conventional methods commonly used to simulate two-phase DDT. The method utilizes a new approximate solution for the two-phase Riemann problem, valid for general equations of state, which has the "shock resolution" property common to Roe-type solvers; thus, if the discontinuous initial data can be connected by a single shock in the gas and/or solid, the approximate solution is exact. Though less computationally expensive, the use of an approximate solution was necessitated by the lack of an exact solution for the general two-phase Riemann problem for complex equations of state. In addition to documenting full details of the approximate Riemann solver, this paper has given a technique for suppressing numerical instabilities near singularities associated with a local loss of hyperbolicity.

The model was shown to predict experimentally observed features associated with DDT induced by low-velocity impact of granular energetic solids, including the initial evolution

of a dispersed compaction wave, a subsequent induction period prior to the onset of vigorous combustion, and the final transition to detonation. Experimentally observed time scales, wave speeds, and stresses are correctly predicted. Further, the results conclusively show for the first time the evolution of a two-phase weak detonation structure; thus, contrary to conventional assumptions, the Chapman–Jouguet wave speed is not the unique wave speed for a self-propagating two-phase detonation. Detailed comparisons of numerical predictions with known theoretical results for the steady weak detonation structure indicated that the method can accurately capture strong shocks induced by detonation with minimal numerical diffusion and dispersion. Based on a detailed convergence study, the nominally second-order method was shown to have a global convergence rate of 1.001 for discontinuous solutions, which is comparable to modern high-resolution methods developed for the Euler equations of gas dynamics, and a rate of 1.670 for continuous solutions.

Finally, we give the following remarks. First, there exists some uncertainty about the implications of the model singularities on the approximate two-phase Riemann solution. It is possible that the approximate solution may not properly represent the true solution behavior in the neighborhood of these singularities in all cases, though it is impossible to know definitively in the absence of exact solutions. In this work, we have chosen to suppress only numerical instabilities induced by these singularities; however, comparisons of predicted detonation structures having embedded singularities with the corresponding structures given by a formal steady-state analysis of the model have shown good agreement. Second, the shock resolution property comes with additional computational expense as much effort is required to compute the square-root averages for system variables. Though not explored in this study, one could replace the square-root averages with simple arithmetic averages. As such, arithmetic averages for complex thermodynamic derivatives could be easily evaluated circumventing the need to compute the potentially cumbersome averages defined in this paper. In this case, the shock resolution property will not be maintained, but a more computationally efficient algorithm will result with potentially little sacrifice in performance.

APPENDIX A

Derivation of the Eigenvector Expansion Coefficients

The eigenvector expansion coefficients $\alpha^{(j)}$ $(j = 1, \ldots, 9)$ [Eqs. (3.11)–(3.19)] associated with the solution of the linear two-phase Riemann problem are derived in this appendix.

To this end, we choose the $\alpha^{(j)}$ such that each component of the vector equation

$$\delta(\mathbf{q}) = \sum_{j=1}^{9} \alpha^{(j)} \mathbf{r}^{(j)} \tag{A.1}$$

is satisfied to within $O[\delta(q_j)^2]$, and such that each component of the vector equation

$$\delta(\mathbf{f}) = \sum_{j=1}^{9} \alpha^{(j)} \lambda^{(j)} \mathbf{r}^{(j)} \tag{A.2}$$

is satisfied to within $O[\delta(f_j)^2]$, where the difference operator is defined by $\delta(\bullet) \equiv (\bullet)_R - (\bullet)_L$. Substituting the expressions for $\mathbf{r}^{(j)}$ $(j = 1, \ldots, 9)$ [Eqs. (2.42)–(2.50)] into Eq. (A.1),

and fully expanding the resulting system of equations give

$$\delta(\rho_1\phi_1) = \alpha^{(1)} + \alpha^{(2)} + \alpha^{(3)} + \alpha^{(7)}\frac{\rho_1\eta_1}{\rho_2\phi_2\big((v_2 - v_1)^2 - c_1^2\big)}, \tag{A.3}$$

$$\begin{aligned}\delta(\rho_1\phi_1 v_1) = {} & \alpha^{(1)}v_1 + \alpha^{(2)}(v_1 + c_1) + \alpha^{(3)}(v_1 - c_1) \\ & + \alpha^{(7)}\frac{\rho_1\eta_1 v_2}{\rho_2\phi_2\big((v_2 - v_1)^2 - c_1^2\big)},\end{aligned} \tag{A.4}$$

$$\begin{aligned}\delta\big(\rho_1\phi_1\big(e_1 + v_1^2/2\big)\big) = {} & \alpha^{(1)}\big(H_1 - c_1^2/\Gamma_1\big) + \alpha^{(2)}(H_1 + v_1c_1) + \alpha^{(3)}(H_1 - v_1c_1) \\ & + \alpha^{(7)}\frac{\rho_1\eta_1\big(H_1 + v_1v_2 - v_1^2/2\big)}{\rho_2\phi_2\big((v_2 - v_1)^2 - c_1^2\big)},\end{aligned} \tag{A.5}$$

$$\delta(\rho_2\phi_2) = \alpha^{(4)} + \alpha^{(5)} + \alpha^{(6)}, \tag{A.6}$$

$$\delta(\rho_2\phi_2 v_2) = \alpha^{(4)}v_2 + \alpha^{(5)}(v_2 + c_2) + \alpha^{(6)}(v_2 - c_2), \tag{A.7}$$

$$\begin{aligned}\delta\big(\rho_2\phi_2\big(e_2 + v_2^2/2\big)\big) = {} & \alpha^{(4)}\big(H_2 - c_2^2/\Gamma_2\big) + \alpha^{(5)}(H_2 + v_2c_2) \\ & + \alpha^{(6)}(H_2 - v_2c_2) + \alpha^{(7)}\eta_2/(\phi_2\Gamma_2),\end{aligned} \tag{A.8}$$

$$\delta\big(\rho_2\phi_2^2\big) = \alpha^{(4)}\phi_2 + \alpha^{(5)}\phi_2 + \alpha^{(6)}\phi_2 + \alpha^{(7)}, \tag{A.9}$$

$$\delta(n) = \alpha^{(5)}n/(\rho_2\phi_2) + \alpha^{(6)}n/(\rho_2\phi_2) + \alpha^{(8)}. \tag{A.10}$$

$$\delta(\rho_2\phi_2 I) = \alpha^{(5)}I + \alpha^{(6)}I + \alpha^{(9)}. \tag{A.11}$$

With the assumption that $\mathbf{q}_L$ is close to $\mathbf{q}_R$, the left-hand sides of Eqs. (A.4), (A.5), (A.7), (A.8), (A.9), and (A.11) can be approximated by the following expressions valid to $O(\delta^2)$, respectively:

$$\begin{aligned}\delta(\rho_1\phi_1 v_1) &\sim v_1\delta(\rho_1\phi_1) + \rho_1\phi_1\delta(v_1), \\ \delta\big(\rho_1\phi_1\big(e_1 + v_1^2/2\big)\big) &\sim \big(e_1 + v_1^2/2\big)\delta(\rho_1\phi_1) + \rho_1\phi_1\delta(e_1) + \rho_1\phi_1 v_1\delta(v_1), \\ \delta(\rho_2\phi_2 v_2) &\sim v_2\delta(\rho_2\phi_2) + \rho_2\phi_2\delta(v_2), \\ \delta\big(\rho_2\phi_2\big(e_2 + v_2^2/2\big)\big) &\sim \big(e_2 + v_2^2/2\big)\delta(\rho_2\phi_2) + \rho_2\phi_2\delta(e_2) + \rho_2\phi_2 v_2\delta(v_2), \\ \delta\big(\rho_2\phi_2^2\big) &\sim \phi_2\delta(\rho_2\phi_2) + \rho_2\phi_2\delta(\phi_2), \\ \delta(\rho_2\phi_2 I) &\sim \rho_2\phi_2\delta(I) + I\delta(\rho_2\phi_2).\end{aligned}$$

Substituting these expressions into Eqs. (A.3)–(A.11) and solving the resulting coupled system of equations for $\alpha^{(1)}, \alpha^{(2)}, \ldots, \alpha^{(9)}$ give

$$\alpha^{(1)} = \delta(\rho_1\phi_1) - \frac{1}{c_1^2}\delta(P_1\phi_1) - \frac{\rho_1\eta_1}{c_1^2}\delta(\phi_1), \tag{A.12}$$

$$\alpha^{(2)} = \frac{1}{2c_1^2}\delta(P_1\phi_1) + \frac{\rho_1\phi_1}{2c_1}\delta(v_1) + \left(\frac{v_2 - v_1}{v_2 - (v_1 + c_1)}\right)\frac{\rho_1\eta_1}{2c_1^2}\delta(\phi_1), \tag{A.13}$$

$$\alpha^{(3)} = \frac{1}{2c_1^2}\delta(P_1\phi_1) - \frac{\rho_1\phi_1}{2c_1}\delta(v_1) + \left(\frac{v_2 - v_1}{v_2 - (v_1 - c_1)}\right)\frac{\rho_1\eta_1}{2c_1^2}\delta(\phi_1), \tag{A.14}$$

$$\alpha^{(4)} = \delta(\rho_2\phi_2) - \frac{1}{c_2^2}\delta(P_2\phi_2), \tag{A.15}$$

$$\alpha^{(5)} = \frac{1}{2c_2^2}\delta(P_2\phi_2) + \frac{\rho_2\phi_2}{2c_2}\delta(v_2), \tag{A.16}$$

$$\alpha^{(6)} = \frac{1}{2c_2^2}\delta(P_2\phi_2) - \frac{\rho_2\phi_2}{2c_2}\delta(v_2), \tag{A.17}$$

$$\alpha^{(7)} = \rho_2\phi_2\delta(\phi_2), \tag{A.18}$$

$$\alpha^{(8)} = \delta(n) - \frac{n}{\rho_2\phi_2 c_2^2}\delta(P_2\phi_2), \tag{A.19}$$

$$\alpha^{(9)} = \rho_2\phi_2\delta(I) + I\delta(\rho_2\phi_2) - \frac{I}{c_2^2}\delta(P_2\phi_2). \tag{A.20}$$

It is easily checked by directly substituting the expressions for $\lambda^{(j)}$ [Eq. (2.41)], $\mathbf{r}^{(j)}$ [Eqs. (2.42)–(2.50)], and $\alpha^{(j)}$ [Eqs. (A.12)–(A.20)] into Eq. (A.2) that the required identities are satisfied to within $O[\delta(f_j)^2]$.

APPENDIX B

Averages for the Approximate Riemann Solution

In this appendix, Eqs. (3.20)–(3.43) are solved for the average quantities $\widetilde{\rho_1\phi_1}$, $\tilde{v}_1$, $\tilde{e}_1$, $\tilde{H}_1$, $\tilde{F}_{1_{\rho 1\phi 1}}$, $\tilde{F}_{1_{\phi 1}}$, $\tilde{F}_{1_{e1}}$, $\widetilde{\rho_2\phi_2}$, $\tilde{\phi}_2$, $\tilde{v}_2$, $\tilde{e}_2$, $\tilde{H}_2$, $\tilde{F}_{2_{\rho 2\phi 2}}$, $\tilde{F}_{2_{\phi 2}}$, $\tilde{F}_{2_{e2}}$, $\tilde{n}$, and $\tilde{I}$. To this end, it is convenient to first substitute the expressions given by Eqs. (3.22)–(3.31) into Eq. (3.20) and to fully expand the resulting expressions:

$$\Delta(\rho_1\phi_1) = \tilde{\alpha}^{(1)} + \tilde{\alpha}^{(2)} + \tilde{\alpha}^{(3)} - \frac{\tilde{\alpha}^{(7)}\tilde{F}_{1_{\phi 1}}}{\widetilde{\rho_2\phi_2}\left[(\tilde{v}_2 - \tilde{v}_1)^2 - \tilde{c}_1^2\right]}, \tag{B.1}$$

$$\begin{aligned}\Delta(\rho_1\phi_1 v_1) = {} & \tilde{\alpha}^{(1)}\tilde{v}_1 + \tilde{\alpha}^{(2)}(\tilde{v}_1 + \tilde{c}_1) + \tilde{\alpha}^{(3)}(\tilde{v}_1 - \tilde{c}_1) \\ & - \frac{\tilde{\alpha}^{(7)}\tilde{v}_2\tilde{F}_{1_{\phi 1}}}{\widetilde{\rho_2\phi_2}\left[(\tilde{v}_2 - \tilde{v}_1)^2 - \tilde{c}_1^2\right]},\end{aligned} \tag{B.2}$$

$$\begin{aligned}\Delta\left(\rho_1\phi_1\left(e_1 + v_1^2/2\right)\right) = {} & \tilde{\alpha}^{(1)}\left(\tilde{H}_1 - \tilde{c}_1^2/\tilde{\Gamma}_1\right) + \tilde{\alpha}^{(2)}(\tilde{H}_1 + \tilde{v}_1\tilde{c}_1) + \tilde{\alpha}^{(3)}(\tilde{H}_1 - \tilde{v}_1\tilde{c}_1) \\ & - \frac{\tilde{\alpha}^{(7)}\left(\tilde{H}_1 + \tilde{v}_1\tilde{v}_2 - \tilde{v}_1^2\right)\tilde{F}_{1_{\phi 1}}}{\widetilde{\rho_2\phi_2}\left[(\tilde{v}_2 - \tilde{v}_1)^2 - \tilde{c}_1^2\right]}\end{aligned} \tag{B.3}$$

$$\Delta(\rho_2\phi_2) = \tilde{\alpha}^{(4)} + \tilde{\alpha}^{(5)} + \tilde{\alpha}^{(6)}, \tag{B.4}$$

$$\Delta(\rho_2\phi_2 v_2) = \tilde{\alpha}^{(4)}\tilde{v}_2 + \tilde{\alpha}^{(5)}(\tilde{v}_2 + \tilde{c}_2) + \tilde{\alpha}^{(6)}(\tilde{v}_2 - \tilde{c}_2), \tag{B.5}$$

$$\begin{aligned}\Delta\left(\rho_2\phi_2\left(e_2 + v_2^2/2\right)\right) = {} & \tilde{\alpha}^{(4)}\left(\tilde{H}_2 - \tilde{c}_2^2/\tilde{\Gamma}_2\right) + \tilde{\alpha}^{(5)}(\tilde{H}_2 + \tilde{v}_2\tilde{c}_2) \\ & + \tilde{\alpha}^{(6)}(\tilde{H}_2 - \tilde{v}_2\tilde{c}_2) - \frac{\tilde{\alpha}^{(7)}\tilde{F}_{2_{\phi 2}}}{\widetilde{\rho_2\phi_2}\tilde{\Gamma}_2},\end{aligned} \tag{B.6}$$

$$\Delta\left(\rho_2\phi_2^2\right) = \tilde{\alpha}^{(4)}\tilde{\phi}_2 + \tilde{\alpha}^{(5)}\tilde{\phi}_2 + \tilde{\alpha}^{(6)}\tilde{\phi}_2 + \tilde{\alpha}^{(7)}, \tag{B.7}$$

$$\Delta(n) = \tilde{\alpha}^{(5)}\tilde{n}/\widetilde{\rho_2\phi_2} + \tilde{\alpha}^{(6)}\tilde{n}/\widetilde{\rho_2\phi_2} + \tilde{\alpha}^{(8)}, \tag{B.8}$$

$$\Delta(\rho_2\phi_2 I) = \tilde{\alpha}^{(5)}\tilde{I} + \tilde{\alpha}^{(6)}\tilde{I} + \tilde{\alpha}^{(9)}. \tag{B.9}$$

Likewise, we substitute the expressions given by Eqs. (3.22)–(3.31) into Eq. (3.21) and fully expand the resulting expressions:

$$\Delta(\rho_1\phi_1 v_1) = \tilde{\alpha}^{(1)}\tilde{v}_1 + \tilde{\alpha}^{(2)}(\tilde{v}_1 + \tilde{c}_1) + \tilde{\alpha}^{(3)}(\tilde{v}_1 - \tilde{c}_1) - \frac{\tilde{\alpha}^{(7)}\tilde{v}_2\tilde{F}_{1_{\phi 1}}}{\widetilde{\rho_2\phi_2}\left[(\tilde{v}_2 - \tilde{v}_1)^2 - \tilde{c}_1^2\right]}, \quad \text{(B.10)}$$

$$\Delta\left(\rho_1\phi_1 v_1^2 + P_1\phi_1\right) = \tilde{\alpha}^{(1)}\tilde{v}_1^2 + \tilde{\alpha}^{(2)}(\tilde{v}_1 + \tilde{c}_1)^2 + \tilde{\alpha}^{(3)}(\tilde{v}_1 - \tilde{c}_1)^2 - \frac{\tilde{\alpha}^{(7)}\tilde{v}_2^2\tilde{F}_{1_{\phi 1}}}{\widetilde{\rho_2\phi_2}\left[(\tilde{v}_2 - \tilde{v}_1)^2 - \tilde{c}_1^2\right]}, \quad \text{(B.11)}$$

$$\begin{aligned}\Delta\left(\rho_1\phi_1 v_1\left(e_1 + v_1^2/2 + P_1/\rho_1\right)\right) &= \tilde{\alpha}^{(1)}\tilde{v}_1\left(\tilde{H}_1 - \tilde{c}_1^2/\tilde{\Gamma}_1\right) + \tilde{\alpha}^{(2)}(\tilde{v}_1 + \tilde{c}_1)(\tilde{H}_1 + \tilde{v}_1\tilde{c}_1) \\ &\quad + \tilde{\alpha}^{(3)}(\tilde{v}_1 - \tilde{c}_1)(\tilde{H}_1 - \tilde{v}_1\tilde{c}_1) - \frac{\tilde{\alpha}^{(7)}\left(\tilde{H}_1 + \tilde{v}_1\tilde{v}_2 - \tilde{v}_1^2\right)\tilde{F}_{1_{\phi 1}}}{\widetilde{\rho_2\phi_2}\left[(\tilde{v}_2 - \tilde{v}_1)^2 - \tilde{c}_1^2\right]}, \quad \text{(B.12)}\end{aligned}$$

$$\Delta(\rho_2\phi_2 v_2) = \tilde{\alpha}^{(4)}\tilde{v}_2 + \tilde{\alpha}^{(5)}(\tilde{v}_2 + \tilde{c}_2) + \tilde{\alpha}^{(6)}(\tilde{v}_2 - \tilde{c}_2), \quad \text{(B.13)}$$

$$\Delta\left(\rho_2\phi_2 v_2^2 + P_2\phi_2\right) = \tilde{\alpha}^{(4)}\tilde{v}_2^2 + \tilde{\alpha}^{(5)}(\tilde{v}_2 + \tilde{c}_2)^2 + \tilde{\alpha}^{(6)}(\tilde{v}_2 - \tilde{c}_2)^2, \quad \text{(B.14)}$$

$$\begin{aligned}\Delta\left(\rho_2\phi_2 v_2\left(e_2 + v_2^2/2 + P_2/\rho_2\right)\right) &= \tilde{\alpha}^{(4)}\tilde{v}_2\left(\tilde{H}_2 - \tilde{c}_2^2/\tilde{\Gamma}_2\right) + \tilde{\alpha}^{(5)}(\tilde{v}_2 + \tilde{c}_2)(\tilde{H}_2 + \tilde{v}_2\tilde{c}_2) \\ &\quad + \tilde{\alpha}^{(6)}(\tilde{v}_2 - \tilde{c}_2)(\tilde{H}_2 - \tilde{v}_2\tilde{c}_2) - \frac{\tilde{\alpha}^{(7)}\tilde{F}_{2_{\phi 2}}}{\widetilde{\rho_2\phi_2}\tilde{\Gamma}_2}, \quad \text{(B.15)}\end{aligned}$$

$$\Delta\left(\rho_2\phi_2^2 v_2\right) = \tilde{\alpha}^{(4)}\tilde{v}_2\tilde{\phi}_2 + \tilde{\alpha}^{(5)}(\tilde{v}_2 + \tilde{c}_2)\tilde{\phi}_2 + \tilde{\alpha}^{(6)}(\tilde{v}_2 - \tilde{c}_2)\tilde{\phi}_2 + \tilde{\alpha}^{(7)}\tilde{v}_2, \quad \text{(B.16)}$$

$$\Delta(v_2 n) = \tilde{\alpha}^{(5)}(\tilde{v}_2 + \tilde{c}_2)\tilde{n}/\widetilde{\rho_2\phi_2} + \tilde{\alpha}^{(6)}(\tilde{v}_2 - \tilde{c}_2)\tilde{n}/\widetilde{\rho_2\phi_2} + \tilde{\alpha}^{(8)}\tilde{v}_2, \quad \text{(B.17)}$$

$$\Delta(\rho_2\phi_2 I v_2) = \tilde{\alpha}^{(5)}(\tilde{v}_2 + \tilde{c}_2)\tilde{I} + \tilde{\alpha}^{(6)}(\tilde{v}_2 - \tilde{c}_2)\tilde{I} + \tilde{\alpha}^{(9)}\tilde{v}_2. \quad \text{(B.18)}$$

Equations (B.4)–(B.9) and (B.13)–(B.18) are first solved for $\widetilde{\rho_2\phi_2}$, $\tilde{\phi}_2$, $\tilde{v}_2$, $\tilde{e}_2$, $\tilde{H}_2$, $\tilde{n}$, and $\tilde{I}$ in Section B.1. Next, Eqs. (B.1)–(B.3) and (B.10)–(B.12) are solved for $\widetilde{\rho_1\phi_1}$, $\tilde{v}_1$, $\tilde{e}_1$, and $\tilde{H}_1$ in Section B.2. Last, expressions for $\tilde{F}_{1_{\rho 1\phi 1}}$, $\tilde{F}_{1_{\phi 1}}$, $\tilde{F}_{1_{e1}}$, $\tilde{F}_{2_{\rho 2\phi 2}}$, $\tilde{F}_{2_{\phi 2}}$, and $\tilde{F}_{2_{e2}}$ are postulated in Section B.3 to complete the construction of the approximate solution.

B.1. *Averages for the Solid Quantities*

In this section, Eqs. (B.4)–(B.9) and Eqs. (B.13)–(B.18) are solved for $\widetilde{\rho_2\phi_2}$, $\tilde{\phi}_2$, $\tilde{v}_2$, $\tilde{e}_2$, $\tilde{H}_2$, $\tilde{n}$, and $\tilde{I}$. It is noted that by substituting the expressions for $\tilde{\alpha}^{(4)}$, $\tilde{\alpha}^{(5)}$, $\tilde{\alpha}^{(6)}$, and $\tilde{\alpha}^{(8)}$ [Eqs. (3.35)–(3.37) and (3.39), respectively] into Eqs. (B.4) and (B.8), that the latter two equations are identically satisfied by any averages we define. Also, it is noted that Eqs. (B.5) and (B.13) are identical expressions. Therefore, only Eqs. (B.5)–(B.7), (B.9), and (B.14)–(B.18) can be considered in determining the required average quantities for the solid phase. To this end, the following relations will prove useful:

$$\tilde{\alpha}^{(4)} + \tilde{\alpha}^{(5)} + \tilde{\alpha}^{(6)} = \Delta(\rho_2\phi_2), \quad \text{(B.19)}$$

$$\tilde{\alpha}^{(5)} + \tilde{\alpha}^{(6)} = \frac{1}{\tilde{c}_2^2}\Delta(P_2\phi_2), \quad \text{(B.20)}$$

$$\tilde{\alpha}^{(5)} - \tilde{\alpha}^{(6)} = \frac{\widetilde{\rho_2\phi_2}}{\tilde{c}_2}\Delta(v_2). \quad \text{(B.21)}$$

First, we rearrange terms in Eq. (B.5) to get

$$\Delta(\rho_2\phi_2 v_2) = \tilde{v}_2\big(\tilde{\alpha}^{(4)} + \tilde{\alpha}^{(5)} + \tilde{\alpha}^{(6)}\big) + \tilde{c}_2\big(\tilde{\alpha}^{(5)} - \tilde{\alpha}^{(6)}\big).$$

Substituting the expressions given by Eqs. (B.19) and (B.21) into the above equation, we obtain

$$\Delta(\rho_2\phi_2 v_2) = \tilde{v}_2\Delta(\rho_2\phi_2) + \widetilde{\rho_2\phi_2}\Delta(v_2).$$

This equation can be solved for $\widetilde{\rho_2\phi_2}$ to give

$$\widetilde{\rho_2\phi_2} = \frac{\Delta(\rho_2\phi_2 v_2) - \tilde{v}_2\Delta(\rho_2\phi_2)}{\Delta(v_2)}. \tag{B.22}$$

Next, we expand the left-hand side of Eq. (B.14) and rearrange terms on the right-hand side of this same equation to get

$$\Delta\big(\rho_2\phi_2 v_2^2\big) + \Delta(P_2\phi_2) = \tilde{v}_2^2\big(\tilde{\alpha}^{(4)} + \tilde{\alpha}^{(5)} + \tilde{\alpha}^{(6)}\big) + 2\tilde{v}_2\tilde{c}_2\big(\tilde{\alpha}^{(5)} - \tilde{\alpha}^{(6)}\big) + \tilde{c}_2^2\big(\tilde{\alpha}^{(5)} + \tilde{\alpha}^{(6)}\big).$$

Substituting the expressions given by Eqs. (B.19)–(B.21) into this equation and simplifying the result gives

$$\Delta\big(\rho_2\phi_2 v_2^2\big) = \tilde{v}_2^2\Delta(\rho_2\phi_2) + 2\widetilde{\rho_2\phi_2}\tilde{v}_2\Delta(v_2). \tag{B.23}$$

Substituting the expression for $\widetilde{\rho_2\phi_2}$ [Eq. (B.22)] into Eq. (B.23) and rearranging terms yield the following quadratic equation for $\tilde{v}_2$:

$$\Delta(\rho_2\phi_2)\tilde{v}_2^2 - 2\Delta(\rho_2\phi_2 v_2)\tilde{v}_2 + \Delta\big(\rho_2\phi_2 v_2^2\big) = 0.$$

This equation has two solutions given by

$$\tilde{v}_2 = \frac{\Delta(\rho_2\phi_2 v_2) \pm \sqrt{[\Delta(\rho_2\phi_2 v_2)]^2 - \Delta(\rho_2\phi_2)\Delta\big(\rho_2\phi_2 v_2^2\big)}}{\Delta(\rho_2\phi_2)}.$$

Performing the difference operations $\Delta(\bullet)\,[\equiv(\bullet)_R - (\bullet)_L]$ in these solutions and simplifying the result give the following expression for the solution corresponding to positive (+) root:

$$\tilde{v}_2 = \frac{\sqrt{\rho_{2L}\phi_{2L}}\,v_{2L} - \sqrt{\rho_{2R}\phi_{2R}}\,v_{2R}}{\sqrt{\rho_{2L}\phi_{2L}} - \sqrt{\rho_{2R}\phi_{2R}}}.$$

Likewise, the following expression is obtained for the solution corresponding to the negative (−) root:

$$\tilde{v}_2 = \frac{\sqrt{\rho_{2L}\phi_{2L}}\,v_{2L} + \sqrt{\rho_{2R}\phi_{2R}}\,v_{2R}}{\sqrt{\rho_{2L}\phi_{2L}} + \sqrt{\rho_{2R}\phi_{2R}}}. \tag{B.24}$$

Clearly, to obtain a physically meaningful average we must choose the solution corresponding to the negative root. Now, substituting this expression for $\tilde{v}_2$ into Eq. (B.22) and simplifying the result yield

$$\widetilde{\rho_2\phi_2} = \sqrt{\rho_{2L}\rho_{2R}\phi_{2L}\phi_{2R}}. \tag{B.25}$$

Next, we multiply Eq. (B.7) by $\tilde{v}_2$ and subtract the result from Eq. (B.16) to obtain

$$\begin{aligned}\Delta\left(\rho_2\phi_2^2 v_2\right) - \tilde{v}_2\left(\rho_2\phi_2^2\right) &= \tilde{\phi}_2\tilde{c}_2\left(\tilde{\alpha}^{(5)} - \tilde{\alpha}^{(6)}\right)\\ &= \widetilde{\rho_2\phi_2}\tilde{\phi}_2\Delta(v_2).\end{aligned}$$

This equation can be solved for $\tilde{\phi}_2$ to give

$$\tilde{\phi}_2 = \frac{\Delta\left(\rho_2\phi_2^2 v_2\right) - \tilde{v}_2\Delta\left(\rho_2\phi_2^2\right)}{\widetilde{\rho_2\phi_2}\Delta(v_2)}.$$

Since exact expressions for the averages $\tilde{v}_2$ and $\widetilde{\rho_2\phi_2}$ are known, this equation for $\tilde{\phi}_2$ reduces to

$$\tilde{\phi}_2 = \frac{\sqrt{\rho_{2L}\phi_{2L}}\phi_{2L} + \sqrt{\rho_{2R}\phi_{2R}}\phi_{2R}}{\sqrt{\rho_{2L}\phi_{2L}} + \sqrt{\rho_{2R}\phi_{2R}}}. \tag{B.26}$$

Similarly, we multiply Eq. (B.9) by $\tilde{v}_2$, and subtract the result from Eq. (B.18) to obtain

$$\begin{aligned}\Delta(\rho_2\phi_2 I v_2) - \tilde{v}_2\Delta(\rho_2\phi_2 I) &= \tilde{I}\tilde{c}_2\left(\alpha^{(5)} - \alpha^{(6)}\right)\\ &= \widetilde{\rho_2\phi_2}\tilde{\phi}_2\Delta(v_2).\end{aligned}$$

Solving this equation for $\tilde{I}$, substituting in the definitions for $\tilde{v}_2$ and $\widetilde{\rho_2\phi_2}$, and simplifying the result gives

$$\tilde{I} = \frac{\sqrt{\rho_{2L}\phi_{2L}}I_L + \sqrt{\rho_{2R}\phi_{2R}}I_R}{\sqrt{\rho_{2L}\phi_{2L}} + \sqrt{\rho_{2R}\phi_{2R}}}. \tag{B.27}$$

Next, we multiply Eq. (B.8) by $\tilde{v}_2$ and subtract the result from Eq. (B.17) to obtain

$$\begin{aligned}\Delta(v_2 n) - \tilde{v}_2\Delta(n) &= \frac{\tilde{c}_2\tilde{n}}{\widetilde{\rho_2\phi_2}}\left(\tilde{\alpha}^{(5)} - \tilde{\alpha}^{(6)}\right)\\ &= \tilde{n}\Delta(v_2).\end{aligned}$$

Solving this equation for $\tilde{n}$, substituting in the definition for $\tilde{v}_2$, and simplifying the result gives

$$\tilde{n} = \frac{\sqrt{\rho_{2L}\phi_{2L}}n_R + \sqrt{\rho_{2R}\phi_{2R}}n_L}{\sqrt{\rho_{2L}\phi_{2L}} + \sqrt{\rho_{2R}\phi_{2R}}}. \tag{B.28}$$

Now, we consider Eqs. (B.6) and (B.15). Expanding the left-hand side of Eq. (B.6) and rearranging terms on the right-hand side of this same equation yield

$$\begin{aligned}&\Delta(\rho_2\phi_2 e_2) + \Delta\left(\rho_2\phi_2 v_2^2/2\right)\\ &\quad= \tilde{H}_2\left(\tilde{\alpha}^{(4)} + \tilde{\alpha}^{(5)} + \tilde{\alpha}^{(6)}\right) - \frac{\tilde{\alpha}^{(4)}\tilde{c}_2^2}{\tilde{\Gamma}_2} + \tilde{v}_2\tilde{c}_2\left(\tilde{\alpha}^{(5)} - \tilde{\alpha}^{(6)}\right) - \frac{\tilde{\alpha}^{(7)}\tilde{F}_{2_{\phi 2}}}{\widetilde{\rho_2\phi_2}\tilde{\Gamma}_2}.\end{aligned} \tag{B.29}$$

Substituting the expressions given by Eqs. (B.19) and (B.21), and the expressions for $\tilde{\alpha}^{(4)}$ [Eq. (3.14)] and $\tilde{\alpha}^{(7)}$ [Eq. (3.17)] into Eq. (B.29), using the second expression in Eq. (3.42)

to replace $\tilde{H}_2$ in favor of $\widetilde{\rho_2\phi_2}$, $\tilde{v}_2$, $\widetilde{P_2\phi_2}$, and $\tilde{e}_2$, and recognizing that the second term on the left-hand side of Eq. (B.29) is simply the expression given in Eq. (B.23) divided by 2, we obtain the following expression after performing some simple algebra:

$$\Delta(\rho_2\phi_2 e_2) - \tilde{e}_2\Delta(\rho_2\phi_2) = \left(\frac{\widetilde{P_2\phi_2}}{\widetilde{\rho_2\phi_2}} - \frac{\tilde{c}_2^2}{\tilde{\Gamma}_2}\right)\Delta(\rho_2\phi_2) + \frac{1}{\tilde{\Gamma}_2}\Delta(P_2\phi_2) - \frac{\tilde{F}_{2_{\phi 2}}}{\tilde{\Gamma}_2}\Delta(\phi_2). \quad \text{(B.30)}$$

Now, upon using the second expression in Eq. (3.41) to replace $\tilde{c}_2^2$ in Eq. (B.30) in favor of $\widetilde{\rho_2\phi_2}$, $\widetilde{P_2\phi_2}$, $\tilde{F}_{2_{\rho 2\phi 2}}$, and $\tilde{F}_{2_{e2}}$, using the second expression in Eq. (3.43) to replace $\tilde{\Gamma}_2$ in Eq. (B.30) in favor of $\widetilde{\rho_2\phi_2}$ and $\tilde{F}_{2_{e2}}$, subtracting the term $\widetilde{\rho_2\phi_2}\Delta(e_2)$ from both sides of Eq. (B.30), and simplifying the result, we obtain

$$\begin{aligned}&\Delta(\rho_2\phi_2 e_2) - \tilde{e}_2\Delta(\rho_2\phi_2) - \widetilde{\rho_2\phi_2}\Delta(e_2)\\ &\quad= \frac{\widetilde{\rho_2\phi_2}}{\tilde{F}_{2_{e2}}}\Delta(P_2\phi_2) - \frac{\widetilde{\rho_2\phi_2}\tilde{F}_{2_{\rho 2\phi 2}}}{\tilde{F}_{2_{e2}}}\Delta(\rho_2\phi_2) - \frac{\widetilde{\rho_2\phi_2}\tilde{F}_{2_{\phi 2}}}{\tilde{F}_{2_{e2}}}\Delta(\phi_2) - \widetilde{\rho_2\phi_2}\Delta(e_2). \quad \text{(B.31)}\end{aligned}$$

At this point, a number of assumptions can be made in order to define $\tilde{F}_{2_{\rho 2\phi 2}}$, $\tilde{F}_{2_{\phi 2}}$, $\tilde{F}_{2_{e2}}$, and $\tilde{e}_2$. Following the analysis of Glaister [18], it is plausible to choose

$$\Delta(\rho_2\phi_2 e_2) - \tilde{e}_2(\rho_2\phi_2) - \widetilde{\rho_2\phi_2}\Delta(e_2) = 0, \quad \text{(B.32)}$$

in which case the right-hand side of Eq. (B.31) reduces to

$$\Delta(P_2\phi_2) - \tilde{F}_{2_{\rho 2\phi 2}}\Delta(\rho_2\phi_2) - \tilde{F}_{2_{\phi 2}}\Delta(\phi_2) - \tilde{F}_{2_{e2}}\Delta(e_2) = 0. \quad \text{(B.33)}$$

Equation (B.32) can then be solved for $\tilde{e}_2$:

$$\tilde{e}_2 = \frac{\Delta(\rho_2\phi_2 e_2) - \widetilde{\rho_2\phi_2}\Delta(e_2)}{\Delta(\rho_2\phi_2)}.$$

In this equation, we replace the term $\widetilde{\rho_2\phi_2}$ with the expression given by Eq. (B.25) and simplify the result to get

$$\tilde{e}_2 = \frac{\sqrt{\rho_{2L}\phi_{2L}}e_{2L} + \sqrt{\rho_{2R}\phi_{2R}}e_{2R}}{\sqrt{\rho_{2L}\phi_{2L}} + \sqrt{\rho_{2R}\phi_{2R}}}. \quad \text{(B.34)}$$

It remains to define the quantities $\tilde{F}_{2_{\rho 2\phi 2}}$, $\tilde{F}_{2_{\phi 2}}$, and $\tilde{F}_{2_{e2}}$ such that Eq. (B.33) is identically satisfied. Definitions for these quantities are postulated in a following section.

Last, we multiply Eq. (B.6) by $\tilde{v}_2$, subtract the result from Eq. (B.15), and simplify the resulting expression to get

$$\begin{aligned}&\Delta\big(\rho_2\phi_2 v_2\big(e_2 + v_2^2/2 + P_2/\rho_2\big)\big) - \tilde{v}_2\Delta\big(\rho_2\phi_2\big(e_2 + v_2^2/2\big)\big)\\ &\quad= \tilde{c}_2\tilde{H}_2\big(\tilde{\alpha}^{(5)} - \tilde{\alpha}^{(6)}\big) + \tilde{v}_2\tilde{c}_2^2\big(\tilde{\alpha}^{(5)} + \tilde{\alpha}^{(6)}\big). \quad \text{(B.35)}\end{aligned}$$

Upon substituting the expressions given by Eqs. (B.20) and (B.21) into Eq. (B.35), re-expressing the left-hand side of Eq. (B.35) in terms of the total enthalpy of the solid H_2 ($=e_2 + v_2^2/2 + P_2/\rho_2$), and simplifying the result, we obtain

$$\Delta(\rho_2\phi_2 v_2 H_2) - \tilde{v}_2\Delta(\rho_2\phi_2(H_2 - P_2/\rho_2)) = \widetilde{\rho_2\phi_2}\tilde{H}_2\Delta(v_2) + \tilde{v}_2\Delta(P_2\phi_2). \quad \text{(B.36)}$$

Now, expanding the second term on the left-hand side of this equation and canceling the appropriate terms give

$$\Delta(\rho_2\phi_2 v_2 H_2) - \tilde{v}_2\Delta(\rho_2\phi_2 H_2) = \widetilde{\rho_2\phi_2}\tilde{H}_2\Delta(v_2).$$

This equation is solved for $\tilde{H}_2$ yielding

$$\tilde{H}_2 = \frac{\Delta(\rho_2\phi_2 v_2 H_2) - \tilde{v}_2\Delta(\rho_2\phi_2 H_2)}{\widetilde{\rho_2\phi_2}\Delta(v_2)}.$$

Since $\widetilde{\rho_2\phi_2}$, $\tilde{\phi}_2$, and $\tilde{v}_2$ are all known quantities, this expression for $\tilde{H}_2$ reduces to

$$\tilde{H}_2 = \frac{\sqrt{\rho_{2L}\phi_{2L}}H_{2L} + \sqrt{\rho_{2R}\phi_{2R}}H_{2R}}{\sqrt{\rho_{2L}\phi_{2L}} + \sqrt{\rho_{2R}\phi_{2R}}}. \tag{B.37}$$

In summary, definitions for the solid phase average quantities $\widetilde{\rho_2\phi_2}$, $\tilde{\phi}_2$, $\tilde{v}_2$, $\tilde{e}_2$, $\tilde{H}_2$, $\tilde{n}$, and $\tilde{I}$ are given by Eqs. (B.25), (B.26), (B.24), (B.34), (B.37), (B.28), and (B.27), respectively.

B.2. *Averages for the Gas Quantities*

In this section, Eqs. (B.1)–(B.3) and Eqs. (B.10)–(B.12) are solved for $\widetilde{\rho_1\phi_1}$, $\tilde{v}_1$, $\tilde{e}_1$, and $\tilde{H}_1$. It is noted, by substituting the expressions for $\tilde{\alpha}^{(1)}$, $\tilde{\alpha}^{(2)}$, $\tilde{\alpha}^{(3)}$, and $\tilde{\alpha}^{(7)}$ into Eq. (B.1), that Eq. (B.1) is satisfied by any averages we define; also, Eqs. (B.2) and (B.10) are identical expressions. Therefore, only Eqs. (B.2), (B.3), (B.11), and (B.12) can be used to determine the required averages for the gas phase. In defining these average quantities, the following relations will prove useful:

$$\tilde{\alpha}^{(1)} + \tilde{\alpha}^{(2)} + \tilde{\alpha}^{(3)} = \Delta(\rho_1\phi_1) - \frac{\tilde{F}_{1_{\phi 1}}}{(\tilde{v}_2 - \tilde{v}_1)^2 - \tilde{c}_1^2}\Delta(\phi_1), \tag{B.38}$$

$$\tilde{\alpha}^{(2)} + \tilde{\alpha}^{(3)} = \frac{1}{\tilde{c}_1^2}\Delta(P_1\phi_1) - \frac{(\tilde{v}_2 - \tilde{v}_1)^2\tilde{F}_{1_{\phi 1}}}{\tilde{c}_1^2\left[(\tilde{v}_2 - \tilde{v}_1)^2 - \tilde{c}_1^2\right]}\Delta(\phi_1), \tag{B.39}$$

$$\tilde{\alpha}^{(2)} - \tilde{\alpha}^{(3)} = \frac{\widetilde{\rho_1\phi_1}}{\tilde{c}_1}\Delta(v_1) - \frac{(\tilde{v}_2 - \tilde{v}_1)\tilde{F}_{1_{\phi 1}}}{\tilde{c}_1\left[(\tilde{v}_2 - \tilde{v}_1)^2 - \tilde{c}_1^2\right]}\Delta(\phi_1). \tag{B.40}$$

First, we rearrange Eq. (B.2) to get

$$\Delta(\rho_1\phi_1 v_1) = \tilde{v}_1\left(\tilde{\alpha}^{(1)} + \tilde{\alpha}^{(2)} + \tilde{\alpha}^{(3)}\right) + \tilde{c}_1\left(\tilde{\alpha}^{(2)} - \tilde{\alpha}^{(3)}\right) - \frac{\tilde{\alpha}^{(7)}\tilde{v}_2\tilde{F}_{1_{\phi 1}}}{\widetilde{\rho_2\phi_2}\left[(\tilde{v}_2 - \tilde{v}_1)^2 - \tilde{c}_1^2\right]}.$$

By substituting the expressions given by Eqs. (B.38) and (B.40) and the expression for $\tilde{\alpha}^{(7)}$ [Eq. (3.17)] into the above equation and simplifying the resulting expression [recognizing that $\Delta(\phi_2) = -\Delta(\phi_1)$], we obtain

$$\Delta(\rho_1\phi_1 v_1) = \tilde{v}_1\Delta(\rho_1\phi_1) + \widetilde{\rho_1\phi_1}\Delta(v_1).$$

This equation is solved for $\widetilde{\rho_1\phi_1}$ to obtain

$$\widetilde{\rho_1\phi_1} = \frac{\Delta(\rho_1\phi_1 v_1) - \tilde{v}_1\Delta(\rho_1\phi_1)}{\Delta(v_1)}. \tag{B.41}$$

Also, expanding the left-hand side of Eq. (B.11) and rearranging the terms on the right-hand side of this same equation give

$$\Delta\left(\rho_1\phi_1 v_1^2\right) + \Delta(P_1\phi_1) = \tilde{v}_1^2\left(\tilde{\alpha}^{(1)} + \tilde{\alpha}^{(2)} + \tilde{\alpha}^{(3)}\right) + 2\tilde{v}_1\tilde{c}_1\left(\tilde{\alpha}^{(2)} - \tilde{\alpha}^{(3)}\right) + \tilde{c}_1^2\left(\tilde{\alpha}^{(2)} + \tilde{\alpha}^{(3)}\right) - \frac{\tilde{\alpha}^{(7)}\tilde{v}_2^2\tilde{F}_{1_{\phi 1}}}{\widetilde{\rho_2\phi_2}\left[(\tilde{v}_2 - \tilde{v}_1)^2 - \tilde{c}_1^2\right]}.$$

Now, substituting in the expressions given by Eqs. (B.38)–(B.40) and the expression for $\tilde{\alpha}^{(7)}$ [Eq. (3.17)] into the above expression, the following result is obtained upon simplifying:

$$\Delta\left(\rho_1\phi_1 v_1^2\right) = \tilde{v}_1^2\Delta(\rho_1\phi_1) + 2\widetilde{\rho_1\phi_1}\tilde{v}_1\Delta(v_1). \tag{B.42}$$

Substituting the expression for $\widetilde{\rho_1\phi_1}$ [Eq. (B.41)] into this expression and rearranging terms result in a quadratic equation for $\tilde{v}_1$:

$$\tilde{v}_1^2\Delta(\rho_1\phi_1) - 2\tilde{v}_1\Delta(\rho_1\phi_1 v_1) + \Delta\left(\rho_1\phi_1 v_1^2\right) = 0.$$

This equation has two solutions given by

$$\tilde{v}_1 = \frac{\Delta(\rho_1\phi_1 v_1) \pm \sqrt{[\Delta(\rho_1\phi_1 v_1)]^2 - \Delta(\rho_1\phi_1)\Delta\left(\rho_1\phi_1 v_1^2\right)}}{\Delta(\rho_1\phi_1)}.$$

Once again, the negative root leads to the physically relevant solution

$$\tilde{v}_1 = \frac{\sqrt{\rho_{1L}\phi_{1L}}v_{1L} + \sqrt{\rho_{1R}\phi_{1R}}v_{1R}}{\sqrt{\rho_{1L}\phi_{1L}} + \sqrt{\rho_{1R}\phi_{1R}}}. \tag{B.43}$$

With $\tilde{v}_1$ known, Eq. (B.41) reduces to

$$\widetilde{\rho_1\phi_1} = \sqrt{\rho_{1L}\rho_{1R}\phi_{1L}\phi_{1R}}. \tag{B.44}$$

Next, we consider Eqs. (B.3) and (B.12). Expanding the left-hand side of Eq. (B.3) and rearranging terms on the right-hand side of this same equation yields

$$\Delta(\rho_1\phi_1 e_1) + \Delta\left(\rho_1\phi_1 v_1^2/2\right) = \tilde{H}_1\left(\tilde{\alpha}^{(1)} + \tilde{\alpha}^{(2)} + \tilde{\alpha}^{(3)}\right) - \frac{\tilde{\alpha}^{(1)}\tilde{c}_1^2}{\tilde{\Gamma}_1} + \tilde{v}_1\tilde{c}_1\left(\tilde{\alpha}^{(2)} - \tilde{\alpha}^{(3)}\right) - \frac{\tilde{\alpha}^{(7)}\left(\tilde{H}_1 + \tilde{v}_1\tilde{v}_2 - \tilde{v}_1^2\right)\tilde{F}_{1_{\phi 1}}}{\widetilde{\rho_2\phi_2}\left[(\tilde{v}_2 - \tilde{v}_1)^2 - \tilde{c}_1^2\right]}. \tag{B.45}$$

Substituting the expressions given by Eqs. (B.38) and (B.40) and the expressions for $\tilde{\alpha}^{(1)}$ [Eq. (3.11)] and $\tilde{\alpha}^{(7)}$ [Eq. (3.17)] into Eq. (B.45), using the first expression in Eq. (3.42) to replace $\tilde{H}_1$ in favor of $\widetilde{\rho_1\phi_1}$, $\tilde{v}_1$, $\widetilde{P_1\phi_1}$, and $\tilde{e}_1$, recognizing that the second term on the left-hand side of Eq. (B.45) is simply the expression given in Eq. (B.42) divided by 2, and using the equality $\Delta(\phi_2) = -\Delta(\phi_1)$, we obtain the following expression after performing some simple algebra:

$$\Delta(\rho_1\phi_1 e_1) - \tilde{e}_1\Delta(\rho_1\phi_1) = \left(\frac{\widetilde{P_1\phi_1}}{\widetilde{\rho_1\phi_1}} - \frac{\tilde{c}_1^2}{\tilde{\Gamma}_1}\right)\Delta(\rho_1\phi_1) + \frac{1}{\tilde{\Gamma}_1}\Delta(P_1\phi_1) - \frac{\tilde{F}_{1_{\phi 1}}}{\tilde{\Gamma}_1}\Delta(\phi_1). \tag{B.46}$$

Now, using the first expression in Eq. (3.41) to replace $\tilde{c}_1^2$ in Eq. (B.46) in favor of $\widetilde{\rho_1\phi_1}$, $\widetilde{P_1\phi_1}$, $\tilde{F}_{1_{\rho 1\phi 1}}$, and $\tilde{F}_{1_{e1}}$, using the first expression in Eq. (3.43) to replace $\tilde{\Gamma}_1$ in Eq. (B.46) in favor of $\widetilde{\rho_1\phi_1}$ and $\tilde{F}_{1_{e1}}$, subtracting the term $\widetilde{\rho_1\phi_1}\Delta(e_1)$ from both sides of Eq. (B.46), and simplifying the result, we obtain

$$\begin{aligned}&\Delta(\rho_1\phi_1 e_1) - \tilde{e}_1\Delta(\rho_1\phi_1) - \widetilde{\rho_1\phi_1}\Delta(e_1)\\ &\quad= \frac{\widetilde{\rho_1\phi_1}}{\tilde{F}_{1_{e1}}}\Delta(P_1\phi_1) - \frac{\widetilde{\rho_1\phi_1}\tilde{F}_{1_{\rho 1\phi 1}}}{\tilde{F}_{1_{e1}}}\Delta(\rho_1\phi_1) - \frac{\widetilde{\rho_1\phi_1}\tilde{F}_{1_{\phi 1}}}{\tilde{F}_{1_{e1}}}\Delta(\phi_1) - \widetilde{\rho_1\phi_1}\Delta(e_1). \quad \text{(B.47)}\end{aligned}$$

Here, as was done for the solid-phase analysis, we choose

$$\Delta(\rho_1\phi_1 e_1) - \tilde{e}_1(\rho_1\phi_1) - \widetilde{\rho_1\phi_1}\Delta(e_1) = 0, \quad \text{(B.48)}$$

in which case Eq. (B.47) reduces to

$$\Delta(P_1\phi_1) - \tilde{F}_{1_{\rho 1\phi 1}}\Delta(\rho_1\phi_1) - \tilde{F}_{1_{\phi 1}}\Delta(\phi_1) - \tilde{F}_{1_{e1}}\Delta(e_1) = 0. \quad \text{(B.49)}$$

Substituting the expression for $\widetilde{\rho_1\phi_1}$ [Eq. (B.41)] into Eq. (B.48) and solving the resulting expression for $\tilde{e}_1$ yield

$$\tilde{e}_1 = \frac{\sqrt{\rho_{1L}\phi_{1L}}e_{1L} + \sqrt{\rho_{1R}\phi_{1R}}e_{1R}}{\sqrt{\rho_{1R}\phi_{1R}} + \sqrt{\rho_{1R}\phi_{1R}}}. \quad \text{(B.50)}$$

Similar to the solid-phase analysis, it is necessary to define the quantities $\tilde{F}_{1_{\rho 1\phi 1}}$, $\tilde{F}_{1_{\phi 1}}$, and $\tilde{F}_{1_{e1}}$ such that Eq. (B.49) is identically satisfied. Definitions for these quantities are postulated in the following section.

Last, we multiply Eq. (B.3) by $\tilde{v}_1$, subtract the result from Eq. (B.12), and simplify the result to get

$$\begin{aligned}&\Delta\big(\rho_1\phi_1 v_1\big(e_1 + v_1^2/2 + P_1/\rho_1\big)\big) - \tilde{v}_1\Delta\big(\rho_1\phi_1\big(e_1 + v_1^2/2\big)\big)\\ &\quad= \tilde{c}_1\tilde{H}_1\big(\tilde{\alpha}^{(2)} - \tilde{\alpha}^{(3)}\big) + \tilde{v}_1\tilde{c}_1^2\big(\tilde{\alpha}^{(2)} + \tilde{\alpha}^{(3)}\big) - \frac{\tilde{\alpha}^{(7)}(\tilde{v}_2 - \tilde{v}_1)\big(\tilde{H}_1 + \tilde{v}_1\tilde{v}_2 - \tilde{v}_1^2\big)\tilde{F}_{1_{\phi 1}}}{\widetilde{\rho_2\phi_2}\big[(\tilde{v}_2 - \tilde{v}_1)^2 - \tilde{c}_1^2\big]}.\end{aligned} \quad \text{(B.51)}$$

Upon substituting the expressions given by Eqs. (B.39) and (B.40), and the expression for $\tilde{\alpha}^{(7)}$ [Eq. (B.17)] into Eq. (B.51), reexpressing the left-hand side of Eq. (B.51) in terms of the total enthalpy of the gas H_1 ($=e_1 + v_1^2/2 + P_1/\rho_1$), and simplifying the result, we obtain

$$\Delta(\rho_1\phi_1 v_1 H_1) - \tilde{v}_1\Delta(\rho_1\phi_1(H_1 - P_1/\rho_1)) = \widetilde{\rho_1\phi_1}\tilde{H}_1\Delta(v_1) + \tilde{v}_1\Delta(P_1\phi_1). \quad \text{(B.52)}$$

Expanding the second term on the left-hand side of this equation and canceling like terms gives

$$\Delta(\rho_1\phi_1 v_1 H_1) - \tilde{v}_1\Delta(\rho_1\phi_1 H_1) = \widetilde{\rho_1\phi_1}\tilde{H}_1\Delta(v_1).$$

Since $\widetilde{\rho_1\phi_1}$ and $\tilde{v}_1$ are known quantities, this equation can be solved for $\tilde{H}_1$ to give

$$\tilde{H}_1 = \frac{\sqrt{\rho_{1L}\phi_{1L}}H_{1L} + \sqrt{\rho_{1R}\phi_{1R}}H_{1R}}{\sqrt{\rho_{1L}\phi_{1L}} + \sqrt{\rho_{1R}\phi_{1R}}}. \quad \text{(B.53)}$$

In summary, the required gas phase average quantities $\widetilde{\rho_1\phi_1}$, $\tilde{v}_1$, $\tilde{e}_1$, and $\tilde{H}_1$ are given by Eqs. (B.44), (B.43), (B.50), and (B.53), respectively.

B.3. *Averages for the Thermodynamic Derivatives*

In this section, definitions for $\tilde{F}_{1_{\rho 1\phi 1}}$, $\tilde{F}_{2_{\rho 2\phi 2}}$, $\tilde{F}_{1_{\phi 1}}$, $\tilde{F}_{2_{\phi 2}}$, $\tilde{F}_{1_{e1}}$, and $\tilde{F}_{2_{e2}}$ are are postulated such that Eqs. (B.33) and (B.49) are identically satisfied. These approximations are all that is needed to complete the approximate Riemann solution. For convenience, Eqs. (B.33) and (B.49) are given below in a slightly rearranged form:

$$\Delta(P_1\phi_1) = \tilde{F}_{1_{\rho 1\phi 1}}\Delta(\rho_1\phi_1) + \tilde{F}_{1_{\phi 1}}\Delta(\phi_1) + \tilde{F}_{1_{e1}}\Delta(e_1), \tag{B.54}$$

$$\Delta(P_2\phi_2) = \tilde{F}_{2_{\rho 2\phi 2}}\Delta(\rho_2\phi_2) + \tilde{F}_{2_{\phi 2}}\Delta(\phi_2) + \tilde{F}_{2_{e2}}\Delta(e_2). \tag{B.55}$$

Since each of these equations contains the three average derivatives, these averages cannot be uniquely defined. As such, the methodology proposed by Glaister [18] is adopted in which artificial states are introduced in order to define the averages.

The following approximations for $\tilde{F}_{1_{\rho 1\phi 1}}$, $\tilde{F}_{1_{\phi 1}}$, and $\tilde{F}_{1_{e1}}$ are proposed:

$$\begin{aligned}\tilde{F}_{1_{\rho 1\phi 1}} = \Bigg\{ &\frac{1}{4}\left[F_1(\rho_{1R}\phi_{1R}, \phi_{1R}, e_{1R}) + F_1(\rho_{1R}\phi_{1R}, \phi_{1R}, e_{1L}) + F_1(\rho_{1R}\phi_{1R}, \phi_{1L}, e_{1L})\right.\\ &\left. + F_1(\rho_{1R}\phi_{1R}, \phi_{1L}, e_{1R})\right] - \frac{1}{4}\left[F_1(\rho_{1L}\phi_{1L}, \phi_{1R}, e_{1R}) + F_1(\rho_{1L}\phi_{1L}, \phi_{1L}, e_{1R})\right.\\ &\left. + F_1(\rho_{1L}\phi_{1L}, \phi_{1R}, e_{1L}) + F_1(\rho_{1L}\phi_{1L}, \phi_{1L}, e_{1L})\right]\Bigg\} \Bigg/ \Delta(\rho_1\phi_1), \quad \text{if } \Delta(\rho_1\phi_1) \neq 0,\end{aligned} \tag{B.56}$$

$$\begin{aligned}\tilde{F}_{1_{\phi 1}} = \Bigg\{ &\frac{1}{2}\left[F_1(\rho_{1R}\phi_{1R}, \phi_{1R}, e_{1R}) + F_1(\rho_{1L}\phi_{1L}, \phi_{1R}, e_{1L})\right] + \frac{1}{2}\left[F_1(\rho_{1R}\phi_{1R}, \phi_{1L}, e_{1R})\right.\\ &\left. + F_1(\rho_{1L}\phi_{1L}, \phi_{1L}, e_{1L})\right]\Bigg\} \Bigg/ \Delta(\phi_1), \quad \text{if } \Delta(\phi_1) \neq 0,\end{aligned} \tag{B.57}$$

$$\begin{aligned}\tilde{F}_{1_{e1}} = \Bigg\{ &\frac{1}{4}\left[F_1(\rho_{1R}\phi_{1R}, \phi_{1R}, e_{1R}) + F_1(\rho_{1L}\phi_{1L}, \phi_{1L}, e_{1R}) + F_1(\rho_{1R}\phi_{1R}, \phi_{1L}, e_{1R})\right.\\ &\left. + F_1(\rho_{1L}\phi_{1L}, \phi_{1R}, e_{1R})\right] - \frac{1}{4}\left[F_1(\rho_{1R}\phi_{1R}, \phi_{1L}, e_{1L}) + F_1(\rho_{1R}\phi_{1R}, \phi_{1R}, e_{1L})\right.\\ &\left. + F_1(\rho_{1L}\phi_{1L}, \phi_{1R}, e_{1L}) + F_1(\rho_{1L}\phi_{1L}, \phi_{1L}, e_{1L})\right]\Bigg\} \Bigg/ \Delta(e_1), \quad \text{if } \Delta(e_1) \neq 0.\end{aligned} \tag{B.58}$$

Similarly, the following approximations for $\tilde{F}_{2_{\rho 2\phi 2}}$, $\tilde{F}_{2_{\phi 2}}$, and $\tilde{F}_{2_{e2}}$ are proposed:

$$\begin{aligned}\tilde{F}_{2_{\rho 2\phi 2}} = \Bigg\{ &\frac{1}{4}\left[F_2(\rho_{2R}\phi_{2R}, \phi_{2R}, e_{2R}) + F_2(\rho_{2R}\phi_{2R}, \phi_{2R}, e_{2L}) + F_2(\rho_{2R}\phi_{2R}, \phi_{2L}, e_{2L})\right.\\ &\left. + F_2(\rho_{2R}\phi_{2R}, \phi_{2L}, e_{2R})\right] - \frac{1}{4}\left[F_2(\rho_{2L}\phi_{2L}, \phi_{2R}, e_{2R}) + F_2(\rho_{2L}\phi_{2L}, \phi_{2L}, e_{2R})\right.\\ &\left. + F_2(\rho_{2L}\phi_{2L}, \phi_{2R}, e_{2L}) + F_2(\rho_{2L}\phi_{2L}, \phi_{2L}, e_{2L})\right]\Bigg\} \Bigg/ \Delta(\rho_2\phi_2), \quad \text{if } \Delta(\rho_2\phi_2) \neq 0,\end{aligned} \tag{B.59}$$

$$\tilde{F}_{2_{\phi 2}} = \left\{ \frac{1}{2}\left[F_2(\rho_{2R}\phi_{2R}, \phi_{2R}, e_{2R}) + F_2(\rho_{2L}\phi_{2L}, \phi_{2R}, e_{2L})\right] + \frac{1}{2}\left[F_2(\rho_{2R}\phi_{2R}, \phi_{2L}, e_{2R}) + F_2(\rho_{2L}\phi_{2L}, \phi_{2L}, e_{2L})\right] \right\} \Big/ \Delta(\phi_2), \quad \text{if } \Delta(\phi_2) \neq 0, \tag{B.60}$$

$$\tilde{F}_{2_{e2}} = \left\{ \frac{1}{4}\left[F_2(\rho_{2R}\phi_{2R}, \phi_{2R}, e_{2R}) + F_2(\rho_{2L}\phi_{2L}, \phi_{2L}, e_{2R}) + F_2(\rho_{2R}\phi_{2R}, \phi_{2L}, e_{2R}) + F_2(\rho_{2L}\phi_{2L}, \phi_{2R}, e_{2R})\right] - \frac{1}{4}\left[F_2(\rho_{2R}\phi_{2R}, \phi_{2L}, e_{2L}) + F_2(\rho_{2R}\phi_{2R}, \phi_{2R}, e_{2L}) + F_2(\rho_{2L}\phi_{2L}, \phi_{2R}, e_{2L}) + F_2(\rho_{2L}\phi_{2L}, \phi_{2L}, e_{2L})\right] \right\} \Big/ \Delta(e_2), \quad \text{if } \Delta(e_2) \neq 0. \tag{B.61}$$

In Eqs. (B.56)–(B.61), the functions $F_1(\rho_1\phi_1, \phi_1, e_1)$ and $F_2(\rho_2\phi_2, \phi_2, e_2)$ are obtained from the thermodynamic state relations for each phase. In the event that $\Delta(\rho_i\phi_i)$, $\Delta(\phi_i)$, or $\Delta(e_i)$ $(i = 1, 2)$ vanishes, we take the appropriate limits of Eqs. (B.56)–(B.61) (i.e., as $\Delta(\rho_i\phi_i) \to 0$, $\Delta(\phi_i) \to 0$, or $\Delta(e_i) \to 0$) to obtain the following expressions, respectively:

$$\tilde{F}_{1_{\rho 1\phi 1}} = \frac{1}{4}\left[\frac{\partial F_1}{\partial(\rho_1\phi_1)}(\rho_1\phi_1, \phi_{1R}, e_{1R}) + \frac{\partial F_1}{\partial(\rho_1\phi_1)}(\rho_1\phi_1, \phi_{1R}, e_{1L}) + \frac{\partial F_1}{\partial(\rho_1\phi_1)}(\rho_1\phi_1, \phi_{1L}, e_{1R}) + \frac{\partial F_1}{\partial(\rho_1\phi_1)}(\rho_1\phi_1, \phi_{1L}, e_{1L})\right], \quad \text{if } \Delta(\rho_1\phi_1) = 0, \tag{B.62}$$

$$\tilde{F}_{1_{\phi 1}} = \frac{1}{2}\left[\frac{\partial F_1}{\partial \rho_1}(\rho_{1R}\phi_{1R}, \phi_1, e_{1R}) + \frac{\partial F_1}{\partial \rho_1}(\rho_{1L}\phi_{1L}, \phi_1, e_{1L})\right], \quad \text{if } \Delta(\phi_1) = 0, \tag{B.63}$$

$$\tilde{F}_{1_{e1}} = \frac{1}{4}\left[\frac{\partial F_1}{\partial e_1}(\rho_{1R}\phi_{1R}, \phi_{1R}, e_1) + \frac{\partial F_1}{\partial e_1}(\rho_{1R}\phi_{1R}, \phi_{1L}, e_1) + \frac{\partial F_1}{\partial e_1}(\rho_{1L}\phi_{1L}, \phi_{1R}, e_1) + \frac{\partial F_1}{\partial e_1}(\rho_{1L}\phi_{1L}, \phi_{1L}, e_1)\right], \quad \text{if } \Delta(e_1) = 0, \tag{B.64}$$

$$\tilde{F}_{2_{\rho 2\phi 2}} = \frac{1}{4}\left[\frac{\partial F_2}{\partial(\rho_2\phi_2)}(\rho_2\phi_2, \phi_{2R}, e_{2R}) + \frac{\partial F_2}{\partial(\rho_2\phi_2)}(\rho_2\phi_2, \phi_{2R}, e_{2L}) + \frac{\partial F_2}{\partial(\rho_2\phi_2)}(\rho_2\phi_2, \phi_{2L}, e_{2R}) + \frac{\partial F_2}{\partial(\rho_2\phi_2)}(\rho_2\phi_2, \phi_{2L}, e_{2L})\right], \quad \text{if } \Delta(\rho_2\phi_2) = 0, \tag{B.65}$$

$$\tilde{F}_{2_{\phi 2}} = \frac{1}{2}\left[\frac{\partial F_2}{\partial \rho_2}(\rho_{2R}\phi_{2R}, \phi_2, e_{2R}) + \frac{\partial F_2}{\partial \rho_2}(\rho_{2L}\phi_{2L}, \phi_2, e_{2L})\right], \quad \text{if } \Delta(\phi_2) = 0, \tag{B.66}$$

$$\tilde{F}_{2_{e2}} = \frac{1}{4}\left[\frac{\partial F_2}{\partial e_2}(\rho_{2R}\phi_{2R}, \phi_{2R}, e_2) + \frac{\partial F_2}{\partial e_2}(\rho_{2R}\phi_{2R}, \phi_{2L}, e_2) + \frac{\partial F_2}{\partial e_2}(\rho_{2L}\phi_{2L}, \phi_{2R}, e_2) + \frac{\partial F_2}{\partial e_2}(\rho_{2L}\phi_{2L}, \phi_{2L}, e_2)\right], \quad \text{if } \Delta(e_2) = 0, \tag{B.67}$$

It is easily checked by direct substitution that the expressions given by Eqs. (B.56)–(B.67) identically satisfy Eqs. (B.54) and (B.55). Though these definitions for the derivatives appear

complicated, they can generally be reduced when the equations of state are specified, and the reduced forms can be directly implemented into a computer algorithm.

REFERENCES

1. B. W. Asay, S. F. Son, and J. B. Bdzil, *Int. J. Multiphase Flow* **22**, 923 (1996).
2. M. R. Baer, *J. Appl. Mech.* **55**, 36 (1988).
3. M. R. Baer and J. W. Nunziato, *Int. J. Multiphase Flow* **12**, 861 (1986).
4. M. R. Baer, R. J. Gross, J. W. Nunziato, and E. A. Igel, *Combust. Flame* **65**, 15 (1986).
5. M. R. Baer and J. W. Nunziato, Compressive combustion of granular materials induced by low-velocity impact, in *Proceedings of the 9th (International) Detonation Symposium, Portland, Oregon*, 1989, p. 744.
6. J. B. Bdzil, R. Menikoff, S. F. Son, A. K. Kapila, and D. S. Stewart, *Phys. Fluids* **11**(2), 378 (1999).
7. J. B. Bell, P. Colella, and J. A. Trangenstein, *J. Comput. Phys.* **82**, 362 (1989).
8. P. B. Butler and H. Krier, *Combust. Flame* **63**, 31 (1986).
9. A. W. Campbell, Deflagration-to-Detonation Transition in Granular HMX, Technical Report LA-UR 80-2016, Los Alamos National Laboratory (Los Alamos, NM, 1980).
10. S. R. Chakravarthy and S. Osher, *Lect. Appl. Math.* **22**, 57 (1985).
11. P. Colella, A. J. Majda, and V. Roytburd, *SIAM J. Sci. Stat. Comput.* **7**, 1059 (1986).
12. R. Courant and K. O. Friedrichs, *Supersonic Flow and Shock Waves* (Wiley, New York, 1948).
13. I. Dimitrienko, *Int. J. Eng. Sci.* **36**, 1215 (1998).
14. D. A. Drew, *Annu. Rev. Fluid Mech.* **15**, 261 (1983).
15. P. Embid and M. Baer, *Continuum Mech. Thermodyn.* **4**, 279 (1992).
16. P. Embid, J. Hunter, and A. Majda, *SIAM J. Appl. Math.* **52**(5), 1199 (1992).
17. P. Embid and A. Majda, *Combust. Flame* **89**, 17 (1992).
18. P. Glaister, *J. Comput. Phys.* **74**, 382 (1988).
19. P. Glaister, *J. Comput. Phys.* **77**, 361 (1988).
20. P. Glaister, *Comput. Math. Appl.* **24**(3), 77 (1992).
21. K. A. Gonthier and J. M. Powers, *Shock Waves* **6**, 183 (1996).
22. K. A. Gonthier, *A Numerical Investigation of the Evolution of Self-Propagating Detonation in Energetic Granular Solids*, Ph.D. dissertation (University of Notre Dame, 1996).
23. K. A. Gonthier and S. F. Son, Modeling compaction induced energy localization in granular HMX, in *Shock Compression of Condensed Matter* (American Institute of Physics, 1999), p. 393.
24. M. J. Grismer, *A Numerical Investigation of Oblique Detonations with Applications to Propulsion*, Ph.D. dissertation (University of Notre Dame, 1994).
25. A. Harten and J. M. Hyman, *J. Comput. Phys.* **50**, 235 (1983).
26. A. Harten, P. D. Lax, and B. van Leer, *SIAM Rev.* **25**(1), 33 (1983).
27. A. C. Hindmarsh, ODEPACK, a systematized collection of ODE solvers, in *Scientific Computing* (North–Holland, Amsterdam, 1983) p. 55.
28. C. Hirsch, *Numerical Computation of Internal and External Flows*, Vol. 1 (Wiley, New York, 1990).
29. E. Isaacson and B. Temple, *SIAM J. Appl. Math.* **52**(5), 1260 (1992).
30. A. K. Kapila, S. F. Son, J. B. Bdzil, R. Menikoff, and D. S. Stewart, *Phys. Fluids* **9**, 3885 (1997).
31. B. L. Keyfitz and H. C. Kranzer, *J. Differential Equations* **47**, 35 (1983).
32. R. J. LeVeque and H. C. Yee, *J. Comput. Phys.* **86**, 187 (1990).
33. R. J. LeVeque, *Numerical Methods for Conservation Laws* (Birkhauser–Verlag, Boston, 1992).
34. P. E. Luebcke, P. M. Dickson, and J. E. Field, *J. Appl. Phys.* **79**(7), 3499 (1996).
35. J. Massoni, R. Saurel, G. Baudin, and G. Demol, *Phys. Fluids* **11**(3), 710 (1999).
36. J. M. McAfee, B. W Asay, W. Campbell, and J. B. Ramsay, Deflagration to detonation transition in granular HMX, in *Proceedings of the 9th (International) Detonation Symposium*, 1989, p. 265.

37. J. M. McAfee, B. W Asay, and J. B. Bdzil, Deflagration-to-Detonation in Granular HMX: Ignition, Kinetics, and Shock Formation, Technical Report LA-UR 93-1754, Los Alamos National Laboratory (Los Alamos, NM, 1993).
38. R. Menikoff, *SIAM J. Sci. Comput.* **15**(5), 1227 (1994).
39. R. Menikoff, Numerical Anomalies Mimicking Physical Effects, Technical Report LA-UR 95-2628, Los Alamos National Laboratory (Los Alamos, NM, 1995).
40. R. Menikoff and K. S. Lackner, Anomalous Physical Effects from Artificial Numerical Length Scales, Technical Report LA-UR 95-2135, Los Alamos National Laboratory (Los Alamos, NM, 1995).
41. R. Pape and D. Gidaspow, *AICHE J.* **44**(2), 294 (1998).
42. J. M. Powers, *Theory of Detonation Structure for Two-Phase Materials*, Ph.D. dissertation (University of Illinois, Urbana-Champaign, 1988).
43. J. M. Powers, D. S. Stewart, and H. Krier, *J. Appl. Mech.* **56**, 15 (1989).
44. J. M. Powers, D. S. Stewart, and H. Krier, *Combust. Flame* **80**, 264 (1990).
45. J. M. Powers, D. S. Stewart, and H. Krier, *Combust. Flame* **80**, 280 (1990).
46. E. M. Kober, J. B. Bdzil, and S. F. Son, Modeling DDT in Granular Explosives with a Multi-Dimensional Hydrocode, Technical Report LA-UR 95-2812, Los Alamos National Laboratory (Los Alamos, NM, 1995).
47. J. D. Ramshaw and J. A. Trapp, *Nucl. Sci. Eng.* **66**, 93 (1978).
48. P. L. Roe and J. Pike, Efficient construction and utilization of approximate Riemann solutions, in *Computing Methods in Applied Sciences and Engineering VI* (North–Holland, New York, 1984) p. 499.
49. P. L. Roe, *J. Comput. Phys.* **43**, 357 (1981).
50. X. Rogue, G. Rodriguez, J. F. Haas, and R. Saurel, *Shock Waves* **8**(1), 29 (1998).
51. V. V. Rusanov, *J. Comput. Math. Phys. USSR* **1**, 267 (1961).
52. H. W. Sandusky and T. P. Liddiard, Dynamic Compaction of Porous Beds, Technical Report NSWC TR 83-246, Naval Surface Warfare Center (Indian Head, MD, 1985).
53. H. W. Sandusky and R. R. Bernecker, Compressive reaction in porous beds of energetic material, in *Proceedings of the 8th (International) Detonation Symposium*, 1985, p. 881.
54. R. Saurel, M. Larini, and J. C. Loraud, *J. Comput. Fluid Dyn.* **1**(2), 155 (1992).
55. R. Saurel, E. Daniel, and J. C. Loraud, *AIAA J.* **32**(6), 1214 (1994).
56. R. Saurel, A. Forestier, D. Veyret, and J. C. Loraud, *Int. J. Numerical Methods Fluids* **18**, 803 (1994).
57. R. Saurel, *J. Propul. Power* **12**(4), 708 (1996).
58. R. Saurel and R. Abgrall, *J. Comput. Phys.* **150**, 425 (1999).
59. S. F. Son, B. W Asay, and J. B. Bdzil, Inert Plug Formation in the DDT of Granular Energetic Materials, Technical Report LA-UR 95-2872, Los Alamos National Laboratory (Los Alamos, NM, 1995).
60. S. F. Son, B. W Asay, J. B. Bdzil, and E. M. Kober, Reaction rate modeling in the deflagration to detonation transition of granular energetic materials, in *Proceedings of the Materials Research Society Meeting, Boston, Massachusetts*, 1995.
61. D. S. Stewart, B. Asay, and K. Prasad, *Phys. Fluids* **6**(7), 2515 (1994).
62. G. Strang, *SIAM J. Num. Anal.* **5**(3), 506 (1968).
63. P. K. Sweby, *SIAM J. Num. Anal.* **21**(5), 995 (1984).
64. P. Woodward and P. Collela, *J. Comput. Phys.* **54**(1), 115 (1984).
65. E. Zauderer, *Partial Differential Equations of Applied Mathematics* (Wiley, New York, 1989).
66. Y. B. Zeldovich and Y. P. Raizer, *Elements of Gasdynamics and the Classical Theory of Shock Waves* (Academic Press, New York, 1968).